DISS. ETH No. 12623

# Investigations of spectral dynamics in rare earth ion doped crystals using high resolution laser techniques

A dissertation submitted to the

SWISS FEDERAL INSITUTE OF TECHNOLOGY ZÜRICH

For the degree of
Doctor of Natural Sciences

presented by
FELIX R. GRAF
Dipl. Natw. ETH

born June 5, 1967
citizen of Winterthur

Accepted on the recommendation of:
Prof. Urs P. Wild, Examiner
Prof. Richard R. Ernst, Co-Examiner

1998

*Meinen Eltern gewidmet*

# 1. Contents

Leer - Vide - Empty

# Acknowledgments

*Todays scientific achievements are seldom based on the work of a single person. In my case they definitely were not. During the years at the Institute of physical chemistry I found a very pleasant and helpful environment, which permitted me to learn a lot. Here as a whole I would like to thank all the people who have made this possible on the administrative side as well as on the scientific side.*

*My warmest thanks go to Prof. Urs Wild who has been a great adviser, leaving me as much freedom as I wished, often fighting with me, also about non-scientific problems. I always enjoyed debating with this humorous and young in mind professor, although we often were not of the same opinion. I guess this is what made the fights so fresh.*

*I have to express my gratitude to Prof. Richard Ernst who although very busy volunteered to act as co-examiner of my thesis. His work and the work of his group have always been very stimulating for my own research.*

*During all this time at the institute I had many collaborations or supervisors. However, one person was always there. If the laser broke, if I had a scientific question or if it regarded personal issue, on the physiological (jogging) as well as on the psychological side. Dr. Alois Renn has been a great supervisor who always took his time if it was needed.*

*Dr. Eric Maniloff was the person who introduced me to the field of frequency selective materials. Not only that he was a great advisor, he also became a good friend. I always enjoyed debating with him on and off the squash court.*

*Dr. Masaharu Mitsunaga from the NTT basic research labs in Japan spent six months at our laboratory. Although this time might seam short compared to the four years I was here, it was the most productive period during my PhD work. It was incredible how much I could learn from him for which I am very thankful. Most of the work presented here is not thinkable without his presence in the group.*

*The collaboration with Dr. Gert Zumofen started relatively late during my PhD work. Nevertheless I regard it as very fruitful. I was able to learn a great many things from Gert, and the discussions with him were always very insightful. I guess it brought him some of the problems of an experimentalist a little closer, it definitely made me understand stochastic processes in a much better way.*

*Dr. Stefan Altner had been the former student on the project I worked on. He introduced me into the fields of rare earth doped crystals and laser stabilization. Without his contributions, my work could not have been performed. Many thanks to you Stefan. Dr. Stefan Bernet showed me the mysteries of phase swept holograms. My work during the first two years was strongly influenced by Stefan. Bernd Plagemann was fighting together with me for an experiment to get done. Finally after about a year we succeeded and I guess we had a good time together. It was for the two of us a good learning experience. As a whole I would like to thank the people of the Wild group. The discussions with Hermann Bach, Elizabeth Donley, Dr. Daniel Erni, Dr. Werner Graff, Dr. Thomas Irngartinger, Dr. Taras Plakhotnik, and Udo Wallenborn (just to mention a few) about "Gott und die Welt" were enjoyable on the scientific as well as on the private side. I wish to express my gratitude to Elizabeth for proof-reading this work and many others. The responsibility for mistakes you may find however, is fully on my side. The international and multi-lingual environment I found in this lab was always very refreshing. Here I would like to particularly thank the representative of the "Italian" community, Dr. M. Croci from whom I also took over the lab and transformed into a big nice tool collection. Thanks for all the patience, Mauro. The contacts were not limited to the own lab. Other members of the institute were always ready to help if I had any question. As a "representative" ensemble let me thank Dr. Tobias Bremi, Dr. Rafael Brühschweiler, Stefan Lienin, Dr. Eric Meister and Dr. Thomas Schulte-Herbrüggen.*

*Our work shop people deserve special thanks. The amount of energy and enthusiasm that they put into their work is admirable. In particular, my thanks go to Andreas Hunkeler and Bruno Lambilotte who constructed the craziest parts and usually had much better ideas on how to do so than I did. Many thanks also to the people from the technical staff, Konrad Boss, Karl Burkhalter, Jörg Forrer, Peter Nyffeler, and Markus Traber who always were very helpful, repaired the things that I broke or were able to solve a problem I had, either on the soft- or hardware side. Thanks to Marie-Therese Werder and Heinrich Willi who took most of the administrative problems off our shoulders.*

*Last but not least a special thank you to my wife, Fatma Hayatally (along with Sally and Sam and ...) for all her patience and the support she gave me during these years. It was not always easy, but quite often I found a hot meal at home after a long frustrating day.*

*Thanks to all. I really had a great time.*

# Abstract

Solids containing rare earth (RE) ions have attracted spectroscopists' attention since the beginning of this century. In the last 30 years, their extremely narrow spectral features in combination with the use of non linear spectroscopy have served to sensitively measure ion-solid interactions and to progressively observe narrower homogeneous linewidths. The potential for using RE ion doped crystals as optical storage materials and processors has lately been a driving force in their investigations. Here, the ratio of inhomogeneous to homogeneous linewidth is regarded as an adequate measure of storage density and can become as big as $10^7$ at cryogenic temperatures. Therefore, the analysis of line broadening is of fundamental as well as applied interest.

This work is concerned with the investigation of interactions of RE ions with their environment. By means of a laser with a kilohertz resolution and non-linear spectroscopy, spectral dynamics as a function of intrinsic, external electric field, or light-pulse induced perturbations are analyzed on different time scales.

In the first part, the theoretical background for the spectroscopy of RE ion doped crystals is outlined. The energy levels are presented and it is shown that due to their electronic properties RE ions have spectrally narrow electronic transitions, sometimes in the sub-kHz regime.

The investigations of these narrow spectral features on the seconds to minutes time scale require very stable tunable laser sources. At present, such devices are not commercially available. In the second part, the performance of a home built laser system is characterized using persistent spectral holes. The results show that frequency selective materials can be used as powerful tools for the high resolution

spectral analysis of laser sources. Complementary to that, they give a measure for the long term evolution of the spectral holes for the particular hole burning substance.

In the third part, the effect of an external electric field on RE ion doped crystals is investigated. It is shown that for these systems the electric field induced frequency shifts are fully reversible. A general theory of Stark splittings of RE doped crystals is introduced and two methods are presented which allow for the determination of the magnitude and orientation of the electric dipole moment differences with sub-degree accuracy.

Finally in the last part, spectral line broadening mechanisms of RE ion doped crystals are discussed and investigated by means of two-pulse photon echoes. Through variation of the experimental parameters, a discrimination between the different contributions is partly achieved and characteristic properties for different dephasing mechanisms are presented. In combination with the measurements from the third part, quantitative predictions of the electric dipole-dipole induced broadening are carried out, which are compared to the experimental results.

# Zusammenfassung

Seit Anfang des Jahrhunderts befassen sich Spektroskopiker mit Festkörpern, die mit Lanthanidionen dotiert sind. Aufgrund zunehmend besser werdender spektraler Auflösung konnten im Laufe der letzten dreissig Jahre Ionen-Festkörperwechselwirkungen mit immer höherer Empfindlichkeit untersucht werden. Das hieraus resultierende bessere Verständnis der Wechselwirkungsdynamik hat massgeblich dazu beigetragen, dass fortlaufend schmalere homogene Linienbreiten bestimmt wurden. Die potentielle Nutzbarkeit von Lanthanidionen dotierten Kristallen für die Datenspeicherung und -prozessierung hat deren Untersuchungen während der letzten Jahre zusätzlich vorangetrieben. Hierbei wird das Verhältnis der inhomogenen zur homogenen Linienbreite als ein gutes Mass für die Kapazität eines frequenzselektiven Speichers betrachtet. Dieses Verhältnis kann bei kryogenen Temperaturen Werte bis zu $10^7$ erreichen. Insofern sind Untersuchungen der die Linienbreiten bestimmenden charakteristischen Prozesse, sowohl von grundlagenwissenschaflichem, als auch von anwendungsorientiertem Interesse.

Die hier präsentierte Arbeit befasst sich mit verschiedenen Wechselwirkungsmechanismen von Lanthanidionen dotierten Kristallen. Mit Hilfe einer schmalbandigen Laserquelle und nichtlinearen spektroskopischen Methoden wird die spektrale Dynamik als Funktion von intrinsischen, externen und Lichtpuls-induzierten Störungen auf verschiedenen Zeitskalen untersucht.

Im ersten Teil werden die spektroskopischen Grundlagen präsentiert. Hierbei wird das Schwergewicht auf den Ursprung der schmalbandigen spektralen Linien gelegt und es wird gezeigt, wie sich verschiedene Störungen auf das Energiespektrum auswirken können.

Typische Linienbreiten liegen meistens im Kilohertzbereich. Die Untersuchung derart schmaler optischer Übergänge auf Zeitskalen von Sekunden bis Stunden erfordert äusserst stabile Laser. Kommerziell sind solche Lichtquellen zur Zeit nicht erhältlich. Deshalb wurde ein kommerzielles System weiterentwickelt, welches im zweiten Teil mittels Lochbrennen charakterisiert wird. Die Resultate belegen einerseits die Brauchbarkeit von frequenzselektiven Materialien zur Spektralanalyse von Lasern. Andererseits geben sie ein Mass für die spektrale Stabilität des Lochbrennmaterials.

Im dritten Teil wird der Einfluss von elektrischen Feldern auf Lanthanidionen dotierte Kristalle untersucht. Es wird gezeigt, dass das Anlegen eines externes elektrisches Feld zu vollkommen reversiblen atomaren Frequenzverschiebungen führt. Eine allgemeine Theorie über Stark Aufspaltungen von Defektzentren in Kristallen wird vorgestellt und zwei Methoden werden präsentiert, welche genaue Messungen der statischen Dipolmomentdifferenzen und deren Orientierungen ermöglichen.

Der letzte Teil ist der Untersuchung von Linienverbreiterungsmechanismen mittels Intensitätsabschwächung von Zweipuls Photonenecho gewidmet. Durch Anpassung der experimentellen Parameter wird eine Unterscheidung der einzelnen Prozesse teilweise erreicht. Charakteristische Erkennungsmerkmale der verschiedenen Wechselwirkungsmechanismen werden präsentiert. Kombiniert mit den Resultaten aus dem dritten Teil können Voraussagen über die erwartete Linienverbreitung aufgrund elektrischer Dipol-Dipol-Kopplungen gemacht werden.

# Symbols and abbreviations

| Symbol | |
|---|---|
| $\|1\rangle$ | Electronic ground state wave function. |
| $\|2\rangle$ | Electronic excited state wave function. |
| $c$ | Speed of light in vacuum, c=2.9979 $\cdot 10^8$ ms$^{-1}$. |
| $d_s$ | Sample thickness. |
| $d$ | Spectral hole depth. See Eq. (5.6). |
| D | Debeye, 1D = $3.33 \cdot 10^{-30}$ Cm. |
| $D$ | Effective quadrupole constant. |
| $D_{jk}$ | Diagonal coupling term between $j$th and $k$th ion. |
| $e$ | Electronic charge, $e = 1.6022 \cdot 10^{-19}$ C. |
| $\|e\rangle$ | Excited state wave function. |
| $\mathbf{E_S}$ | Externally applied electro-static field amplitude. |
| $E_{S0}$ | Mean of $\|\mathbf{E_S}\|$. |
| $\mathbf{E}$ | Electro-magnetic field. |
| $\mathcal{E}$ | Electro-magnetic field envelope. |
| f | Oscillator strength. |
| f' | Oscillator strength along electro-magnetic field polarization. |
| $\mathcal{G}_{c(s)}$ | Crystal (site) symmetry group. |
| $g_i$ | Order of Group $\mathcal{G}_i$. |
| $\|g\rangle$ | Ground state wave function. |
| H | Static magnetic field. |
| $\mathscr{H}$ | Hamiltonian of a single RE ion in a crystal. |
| $\mathscr{H}_x$ | x contribution to the Hamiltonian $\mathscr{H}$. |
| $\hbar$ | $h/2\pi$, $h$ Planck constant, $h = 6.6262 \cdot 10^{-34}$ Js. |
| $\mathcal{I}$ | RE ion nuclear spin operator. |
| $\mathcal{I}_k$ | $k$th laser pulser intensity. |
| $I(t)$ | Echo intensity. |
| $I_0$ | $I_0 \sim \|\mathbf{P_0}\|^2$. |

| Symbol | |
|---|---|
| $J_{jk}$ | Off-diagonal coupling term between $j$th and $k$th ion. |
| $\mathbf{l}$ | Electron angular momentum. |
| $l$ | Reference cavity length. |
| $m_e$ | Electron mass, $m_e = 9.1096 \cdot 10^{-31}$kg. |
| $n$ | Refractive index. |
| $p$ | Probability of a lattice site to be occupied by a RE ion. |
| $\mathbf{P}(t)$ | Echo polarization. |
| $\mathbf{P}_0$ | $\mathbf{P}(t)$ for $\Phi(t) = 0$. |
| $P(t)$ | $\lvert\mathbf{P}(t)\rvert$. |
| $\langle N \rangle$ | Num. of spont. decay events of el. excitations between 0 and $2t_{12}$. |
| $\mathbf{Q}$ | See Eq. (3.10). |
| $\mathbf{r}$ | Pseudo-spin vector (Bloch vector). |
| $r_{ik}$ | Radial distance between ion $i$ and $k$. |
| $\mathbf{s}$ | Electron spin operator. |
| $\mathcal{S}$ | Host ion nuclear spin operator. |
| $S$ | Pound Drever error signal. |
| $\mathcal{T}_k$ | $k$th pulse strength. |
| $T$ | Temperature. |
| $T_\mathrm{m}$ | Host-ion spin flip time. |
| $t_{12}$ | 2PPE inter pulse time. |
| $t_\mathrm{s}$ | Scrambler pulse time. |
| $u(t)$ | Stochastic variable, see Eq. (7.5). |
| $\hat{\mathrm{V}}$ | Perturbation operator. |
| | |
| $\alpha$ | Absorption. |
| $\alpha_\mathrm{S}$ | Azimuthal angle of the static dipole moment difference $\delta\boldsymbol{\mu}$. |
| $\beta_\mathrm{S}$ | Polar angle of the static dipole moment difference $\delta\boldsymbol{\mu}$. |

| Symbol | |
|---|---|
| $\Gamma$ | Linewidth. |
| $\Gamma_{\mathrm{h}}$ | Homogeneous linewidth extrapolated to zero pulse strength. |
| $\Gamma_{\mathrm{LT}}$ | Lifetime limited linewidth, $\Gamma_{\mathrm{LT}} = 1/(2\pi T_1)$. |
| $\gamma$ | Lifetime limited coherence decay rate, $\gamma = \gamma_1/2$. |
| $\gamma_1$ | Excited state intensity decay rate, $\gamma_1 = 1/T_1$. |
| $\gamma_k$ | Gyromagnetic ratio of $k$th ion. |
| $\Delta(t)$ | Frequency offset. |
| $\Delta_{0k}$ | Static frequency offset of ion $k$. |
| $\delta\boldsymbol{\mu}_i$ | $i$th ion static dipole moment diff. between excited and ground state. |
| $\delta\mu$ | $\delta\mu = \lvert\delta\boldsymbol{\mu}_k\rvert,\ \forall k$. |
| $\boldsymbol{\epsilon}$ | Electro-magnetic field polarization. |
| $\epsilon_0$ | $\epsilon_0 = 8.854 \times 10^{-12}\mathrm{As/(Vm)}$. |
| $\epsilon(\omega)$ | Dielectric constant at frequency $\omega$. |
| $\zeta_{\mathrm{S}}$ | Stark coefficient, $\zeta_{\mathrm{S}} = \Omega_{\mathrm{S}}\lvert\mathbf{E}_{\mathrm{S}}\rvert^{-1}/(2\pi)$. |
| $\eta$ | Holographic diffraction efficiency. |
| $\bar{\eta}$ | Effective field gradient parameter. |
| $\eta(\omega)$ | Dielectric correction at frequency $\omega$. |
| $\theta_{ik}$ | Angle between vectors at ion $i$ and $k$. |
| $\theta(t)$ | Variable defined through $u(t)$, see Eq. (7.10). |
| $\theta_{\mathrm{S}}$ | Polar angle of $\mathbf{E}_{\mathrm{S}}$. |
| $\vartheta$ | Pulse angle. |
| $\kappa$ | Thermal expansion coefficient. |
| $\kappa(\Omega)$ | Angular dependence of dipole interaction. |
| $\boldsymbol{\mu}_{12}$ | Transition dipole moment. |
| $\mu$ | Trans. dipole moment along el. field polarization, $\mu = \langle\boldsymbol{\mu}_{12}\lvert\boldsymbol{\epsilon}\rangle$. |
| $\mu_{\mathrm{B}}$ | Bohr magneton, $9.274{\cdot}10^{-24}\mathrm{Am}^2$. |
| $\mu_{\mathrm{N}}$ | Nuclear magneton, $5.051{\cdot}10^{-27}\mathrm{Am}^2$. |
| $\nu$ | Laser frequency. |

| Symbol | |
|---|---|
| $\nu_b$ | Laser hole burning frequency position. |
| $\nu_p$ | Phonon frequency. |
| $\xi$ | See Eq. (7.6). |
| $\hat{\rho}$ | Density operator. |
| $\rho_{ik}$ | Matrix element $\langle i\|\hat{\rho}\|k\rangle$. |
| $\rho_0$ | Density of sites, which can be replaced by RE ions. |
| $\sigma_A$ | Allan variance. |
| $\sigma_\nu$ | Standard deviation of the inhomogeneous band. |
| $\sigma_S$ | Standard deviation of Stark modulated echo intensity. |
| $\sigma^j$ | Third Pauli matrix of $j$th ion. $\sigma^j = \frac{1}{2}(\|2\rangle\langle 2\| - \|1\rangle\langle 1\|)_j$ . |
| $\tau_k$ | $k$th optical excitation pulse length. |
| $\tau_{Sk}$ | $k$th Stark pulse length. |
| $\Phi(t_{12})$ | Accumlated phase factor in 2PPE at rephasing time. |
| $\phi$ | Electro-magnetic field phase. |
| $\phi_S$ | Azimuthal angle of $\mathbf{E}_S$. |
| $\chi$ | Rabi frequency. |
| $\|\psi\rangle$ | State function. |
| $\Omega_{Sk}$ | Stark shift of $k$th ion, $\Omega_{Sk} = \delta\boldsymbol{\mu}_k\mathbf{E}_S/\hbar$. |
| $\Omega_S$ | $\Omega_S = \delta\mu\|\mathbf{E}_S\|/\hbar$. |
| $\Omega_{S0}$ | Mean Stark shift. |
| $\Omega$ | Spatial angle. |
| $\omega$ | $\omega = 2\pi\nu$. |
| $\omega(t)$ | Optical transition frequency. |
| $\omega_0$ | Static optical transition frequency. |
| $\omega_1$ | Laser frequency. |

| Abbreviation | |
|---|---|
| 2PPE | Two-pulse photon echoes. |
| AOM | Acousto optic modulator. |
| CF | Crystal field. |
| EOM | Electro optic modulator. |
| EFS | Excitation induced frequency shifts. |
| EQP | Equilibrium phonons. |
| FI | Free ion. |
| FSM | Frequency selective materials. |
| FSR | Free spectral range. |
| FWHM | Full width half maximum. |
| HF | Hyperfine. |
| ICA | Intra cavity assembly. |
| NQP | Non-equilibrium phonons. |
| ODNMR | Optically detected nuclear magnetic resonance. |
| OFID | Optical free induction decay. |
| PMT | Photo-multiplyer tube. |
| PSHB | Persistent spectral hole burning. |
| Q | Quadrupole. |
| RE | Rare earth. |
| SHB | Spectral hole burning. |
| SI | Spin-ion. |
| SMPE | Stark modulated photon echoes. |
| SMS | Single molecule spectroscopy. |
| TDM | Temporal division multiplexing. |
| TLS | Two-level systems. |
| WDM | Wavelength division multiplexing. |

# 1. Introduction

"*Löcher sind statisch.*
*Löcher auf Reisen gibt es nicht. ... Fast nicht!*"

aus "Zur soziologischen Psychologie der Löcher"
in *Gruss nach vorn,* Kurt Tucholsky (1926).

In the last 20 years, the requirements on memory storage, signal transmission, and access rates have dramatically increased. It has become evident that on the long run purely electronic devices will neither be able to achieve the needed transmission rates nor will they succeed in storing the increasing data volumes. Although currently the traditional memories are still improving, their intrinsic limits are getting closer and closer. The idea of using purely optical storage devices seemed obvious since optical storage and optical transmission offer advantages over the standard techniques. Two major advantages are the small cross talk between the multiplexed signals and the huge transmission rates connected to the large bandwidths.

In part, the turn-over towards optical technologies is already occuring now, if one considers the increasing number of optical transmission lines used in telecommunications. In the fields of data storage and processing the search for "ideal" materials and techniques which need to match the requirements put forward by the use of the optical signal transmission is still going on and different approaches are proposed [1–4]. Up to now, all studied systems have some severe drawbacks and it is quite thinkable that none of them will be used in future applications. Still, the investigation of the currently known materials is justified since many aspects are studied which will need to be controllable in any future optical storage technology, no matter what the actual storage medium will be.

In this work the focus is put on the investigation of one type of the presently used storage substances: frequency selective materials (FSM). A pictorial way to demonstrate the principle of storage in FSM is their comparison to a book. This is illustrated in Fig. (1.1). On each page of the book it is possible to write information.[1] The total information contained in a book is proportional to the information per page times the total number of pages. Analogously, FSM allow the storage of different pages (or images) at different "colors". The number of pages or the number of "colors channels" $\Lambda_s$, ranges between $10^4 - 10^7$.

[1]Images can be encoded as a bit pattern. Through the bit pattern one can assign to each page a curtain memory capacity given by the page size divided by the minimal bit size, thus yielding a measure for the contained information per page.

These large ratios are only achievable at cryogenic temperatures.[2] The spectral width of a single color channel is more or less given by the inverse of the lifetime of the electronic state which is excited with a light source. This width is addressed as homogeneous linewidth. The "total" width or better, the inhomogeneous linewidth originates from different local environments of the different chromophores which leads to shifts of their electronic transition frequencies.[3] The ratio of inhomogeneous to homogeneous linewidth roughly defines $\Lambda_s$. The investigation of FSM comprises

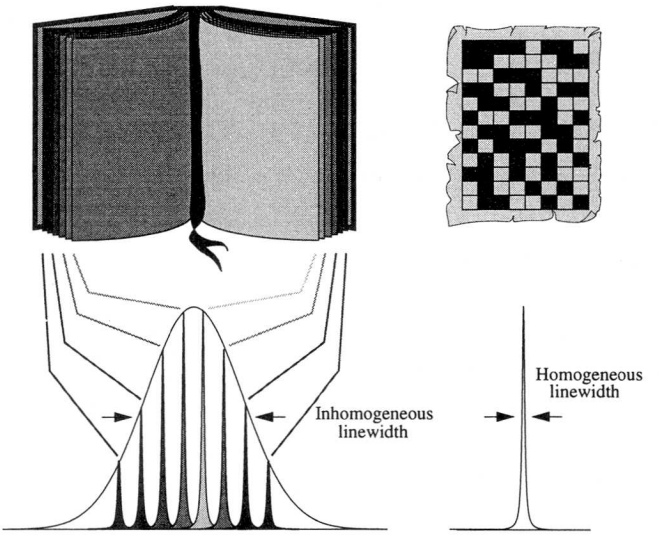


**Figure 1.1:** Picturesque analogue of a frequency selective material. Writing two images at different wavelengths of a FSM, corresponds to printing the two images onto different pages in a book (From Ref. [6]).

a better understanding of the underlying mechanisms, as well as the more technical need of a demonstration of the principle feasibilities. In both fields the literature is

[2]Current proposals for high-speed processors also require helium temperatures [5], such that it is thinkable that in the future certain ultra-high speed computations and correlations may be performed at low temperatures. However, up to now the temperature requirement is the biggest drawback for FSM.

[3]The terms homogeneous and inhomogeneous linewidth will be defined in a more rigorous form in Chapter 2.

vast and it is referred to Refs. [7–12] for overviews. The FSM mostly under investigation can be separated into two groups: (i) organic chromophore doped polymers and (ii) rare earth (RE) ion doped crystals. Both systems have a large $\Lambda_s$. However, their absolute linewidths are different by more than five orders of magnitude. In dye doped polymers typical homogeneous linewidths are in the few 100 MHz range and $\Lambda_s \sim 10^4 - 10^5$. In RE ion doped crystals the homogeneous linewidth is in the sub-kHz range and $\Lambda_s$ can become as big as $10^7$. It is thus obvious that the principle mechanisms which influence the lineshapes as well as the requirements put on the experimental equipment are quite different for the two systems. Nevertheless, the common large $\Lambda_s$ makes both systems very attractive for different branches of optical storage and processing, mainly because FSM intrinsically match some criteria given by optically transmitted signals.

During the first part of my PhD work, I participated on investigations of the usability of FSM for data storage and processing. In the latter case the focus was put on possible applications in the field of division multiplexing. When employing multiplexed signals, it is necessary to combine (split apart) the different transmitted transmission signals at the beginning (end) of the data line. Commonly two approaches are considered: either the parallel transmission of different signals at different carrier frequencies or their temporal separation. In the literature these two methods are referred to as wave length division multiplexing (WDM), and temporal division multiplexing (TDM). The large number of publications over the last ten years proposing WDM and/or TDM techniques demonstrates the ongoing interest in the search of new approaches and solutions. Major requirements on a WDM system are, fast switching between different wavelengths, little cross talk between the different frequency channels (contrast better than -30 dB), and a large number of channels with bandwidths in the GHz regime. Using a dye doped polymer, we developed a WDM device able to split a broadband signal into 100 different frequency channels of 1 GHz bandwidth and spaced by 9 GHz [13]. The applicability of FSM for TDM was demonstrated in a RE ion doped crystal, showing that by means of frequency swept stimulated photon echoes, bit stream compression can be achieved [14, 15].

As pointed out earlier, when considering FSM for large scale data storage, $\Lambda_s$ is mostly taken as the figure of merit which represents the maximal possible number of images stored at one spatial position. However, up to now an experiment obtaining such a multiplicity had never been performed. Combining special holographic techniques and exploiting the possibility of electric field multiplexing we were able to record 12'000 holographic images in a single dye doped polymer sample, thus reaching the limit given by the material ($\Lambda_s \sim 10^4$) [3]. The search for better materials and the investigations of large scale storage and data reliability using FSM in dye doped polymers are the topic of another thesis performed in our group [16].

In the work presented in this thesis, RE ion doped crystals were investigated, with the focus put on the analysis of different spectral dynamics leading to line broadening. Combining the techniques of high-resolution cw-lasers and the use of non-linear laser spectroscopy, the linewidths of optical transitions of RE ion doped crystals were investigated as a function of varying parameters on different time scales.

The thesis is structured as follows: in Chapter 2, RE ion doped crystals are introduced and the different contributions of the Hamiltonian characterizing the observed spectrum are discussed. The technique of hyperfine hole burning is presented which allows for the sensitive measurement of energy splittings. In Chapter 3, the theoretical frame work of two level atoms is sketched. By means of the optical Bloch equations it is demonstrated how dynamical interactions can affect the spectral linewidth measured using photon echoes. Chapter 4 introduces the instrumentation employed during this work. The focus is put on the frequency stabilization of the dye laser by means of the side band modulation. In Chapter 5, spectral broadening of $Eu^{3+}$ in $Y_2SiO_5$ is investigated on the minute time scale using the actively stabilized laser system. It is shown that the effect of broadening resulting from spectral diffusion is smaller than 20 kHz/h with the value limited by the laser linewidth. Another technically important aspect of RE ion doped crystals is presented; their possible use as frequency markers of extremely high accuracy. By means of hyperfine hole burning, the laser performance of the system described in Chapter 4 is verified and improved. In Chapter 6, the effect of an external electric field on RE ion doped crystals is investigated. A generalized theory of Stark mod-

ulated photon echoes is presented and it is shown that echo intensity modulations arise due to the interference of the echo emission of RE ions located at inequivalent sites. The technique is used to determine the orientation and magnitude of the induced dipole moments of RE ions with high accuracy. It is further shown that the application of an electric field can be treated as a fully reversible perturbation for all systems studied in this work. Finally, the active laser is used to measure Stark splittings in the frequency domain. The work concludes with Chapter 7. Based on the measurements presented in Chapter 6 it is shown that for $Eu^{3+}$ in $Y_2SiO_5$, excitation induced frequency shifts (EFS) are solely responsible for the observed line broadening. The effect of EFS on two-pulse photon echoes is studied experimentally as well as theoretically. The theoretical analysis is based on a semi-classical stochastic treatment. Finally, an experiment is presented, which demonstrates that EFS is dominated by diagonal interactions and that off-diagonal interactions can be neglected. A quantitative comparison of the calculated and measured broadening is performed and reasonable agreement is achieved. The Chapter terminates with the analysis of broadening effects in $Pr^{3+}$:$Y_2SiO_5$.

# 2. Rare earth ion spectroscopy in solids

The basic concepts of the energy levels in RE doped ions are introduced and the individual terms leading to energy shifts are discussed. The ion/host systems under investigation are presented. It is shown that the energy splittings often allow for a separation of the wave function, such that a RE ion can be described as a two level atom. Finally, hyperfine hole burning is introduced and it is shown that this technique allows for the determination of energy splittings with subinhomogeneous linewidth resolution.

## 2.1 Introduction

In 1794 the lanthanides were discovered by Gadolin who found a black metal mineral in Ytterby (Sweden). It was called Yttria and appeared to consist of a mixture of several lanthanides. The next 150 years lead to the discovery of all lanthanides, until the last one, Promethium, was found in 1945.

The first spectroscopic investigations of rare earth (RE) compounds, an alternative name for the lanthanides, showed a feature that has continued to attract physicists for many years: an extreme sharpness of the spectral lines. As early as 1908 it was observed by Becquerel that these lines can be as narrow as those commonly observed in the spectra of free atoms or molecules and could therefore be used as very sensitive probes of the environment [17]. With the introduction of spectroscopic techniques such as photon echoes [18,19] and hole burning [20] the resolution could be further increased. A better understanding of dynamical interactions of the RE ions and the surrounding medium has lead to the narrowest spectral lines ever observed in solids [21].

The aim of this Chapter is to introduce the different contributions which are of importance for the spectroscopy of RE ion doped crystals. The Chapter is structured as follows: In Section 2.2 the different terms of the Hamiltonian of a RE ion embedded into a crystal are analyzed and the guest ion/host system under investigation is presented. Finally, in Section 2.3 hyperfine hole burning is be introduced.

## 2.2 Interaction of the solid with a RE ion

One of the advantages of RE ions in crystals lies in the simple structure of their Hamiltonian. The narrow optical lines indicate that the interaction of the RE ion with its environment is relatively weak, which to a large extent allows one to consider a weakly perturbed free ion - a highly attractive and quite unique feature for guest/host systems. The summary given here is not meant to give a complete and rigorous overview over the determination of energy levels of lanthanides. Nevertheless, the main arguments are presented since the origin of the interaction strongly

affects the spectrum of the RE ions. A detailed discussion of time-independent interactions of a free ion coupling to a static environment is presented by Hüfner [22]. A presentation of time-dependent contributions is given by various authors for different interaction forms [23–25]. The list is by no means complete and it is referred to later Chapters for proper referencing. An overview of non-linear spectroscopic techniques used in RE ion spectroscopy can be found in Ref. [8].

For experiments involving RE ion doped crystals, the total Hamiltonian can be decomposed as

$$\mathscr{H} = \mathscr{H}_{\mathrm{A}}(t) + \mathscr{H}_{\mathrm{B}} + \hat{V}_{\mathrm{AP}}(t) \ , \tag{2.1}$$

where $\mathscr{H}_{\mathrm{A}}(t) = \mathscr{H}_0 + \mathscr{H}_1(t)$ stands for the atomic Hamiltonian. It contains a time-invariant term $\mathscr{H}_0$ and a time-dependent term $\mathscr{H}_1(t)$. The anharmonic phonon bath is represented by $\mathscr{H}_{\mathrm{B}}$ and the interaction is considered through $\hat{V}_{\mathrm{AP}}(t)$ which takes electron-phonon coupling and anharmonicity into account. Excellent investigations of the effect of $\hat{V}_{\mathrm{AP}}(t)$ on the optical transition line shape are given by Orbach and by Harris [26, 27]

In this Section, $\mathscr{H}_{\mathrm{A}}(t)$ is discussed. The presentation is as follows: Subsection 2.2.1 is devoted to the description of the various terms contained in $\mathscr{H}_0$. In Subsection 2.2.2, the contributions of $\mathscr{H}_1(t)$ relevant for RE ion doped crystals are sketched. The separation into a time independent and a dynamic term is somewhat arbitrary, a fact which is discussed in Subsection 2.2.3. Further, the energy levels relevant for the RE ions investigated in this work are presented. Finally, in Subsection 2.2.4 it is shown under which conditions the approximation of a RE ion as a two level atom can be made.

### 2.2.1 Time-independent Hamiltonian

The time-independent contribution of the atomic Hamiltonian $\mathscr{H}_{\mathrm{A}}(t)$ can be approximated by

$$\mathscr{H}_0 = \mathscr{H}_{\mathrm{FI}} + \mathscr{H}_{\mathrm{CF}} + \mathscr{H}_{\mathrm{HF}} + \mathscr{H}_{\mathrm{Q}} + \mathscr{H}_{\mathrm{Z}} + \mathscr{H}_{\mathrm{z}} \ , \tag{2.2}$$

where (i) $\mathscr{H}_{\mathrm{FI}}$ is the free ion Hamiltonian, (ii) $\mathscr{H}_{\mathrm{CF}}$ represents the crystal field Hamiltonian, (iii) $\mathscr{H}_{\mathrm{HF}}$ denotes the hyperfine coupling between the 4f electrons and the RE nucleus, (iv) $\mathscr{H}_{\mathrm{Q}}$ the nuclear electric quadrupole interaction, (v) $\mathscr{H}_{\mathrm{Z}}$ the nuclear Zeeman interaction, and (vi) $\mathscr{H}_{\mathrm{z}}$ the electronic Zeeman interaction. In the experiments described here no magnetic fields were applied. Therefore, in the following treatments the terms (v) and (vi) are omitted. The remaining four factors will now be shortly described.

**(i) Free ion.** Due to the strong shielding of the 4f electrons, which is caused by the outer orbitals 5s and 5d, the Hamiltonian for RE ions can often be described starting from the free ion Hamiltonian $\mathscr{H}_{\mathrm{FI}}$. Realizing that all electronic shells except the 4f shell are spherically symmetric (closed shells), only interactions between the 4f electrons lead to a removal of degenerecies and thus need to be taken into consideration.[1] The radial part of $\mathscr{H}_{\mathrm{FI}}$ can then be written as

$$\mathscr{H}_{\mathrm{FI}} = -\frac{\hbar^2}{2m_e}\sum_{i=1}^{N}\Delta_i - \sum_{i=1}^{N}\frac{Z^*e^2}{r_i} + \sum_{i<j}^{N}\frac{e^2}{r_{ij}} + \xi\,\mathbf{l}\cdot\mathbf{s} \tag{2.3}$$

where $N$ runs over the number of 4f electrons, $Z^*e$ is the screened nuclear charge, $\xi$ is the spin-orbit coupling function, and $\mathbf{s}$ and $\mathbf{l}$ denote the electronic spin and angular momentum operators, respectively. Again, the first two factors are spherically symmetric and can be ignored. What remains are the third and fourth terms, $\mathscr{H}_{\mathrm{C}}$ and $\mathscr{H}_{\mathrm{SO}}$, which represent the mutual Coulomb interaction of the 4f electrons and the spin-orbit coupling, respectively. In some RE systems the two contributions are of the same order of magnitude and neither Russell-Sanders ($\mathscr{H}_{\mathrm{C}} \gg \mathscr{H}_{\mathrm{SO}}$) nor $J-J$ coupling ($\mathscr{H}_{\mathrm{C}} \ll \mathscr{H}_{\mathrm{SO}}$) apply. This is usually denoted as intermediate case [22]. However, in many cases the Russell-Sanders approximation describes the systems rather well and the Hamiltonian can be diagonalized using the $|LSJ\rangle$'s as a basis set. In what follows, the Russell-Sanders approximation will be used.

[1] The spherically symmetric contributions, up to the first order lead to an equal shift for all terms of the 4f configuration levels. They will therefore be omitted.

**(ii) Crystal field.** If the crystal field strength is clearly smaller than the energy separation between different $J$-manifolds, it can treated, at least in a first approximation as a perturbation term. In this case $J$ remains a good quantum number. This limit is denoted as the weak field case and is mostly fulfilled in RE ions in crystals. Within one $|LSJ\rangle$ manifold the states are split into the different irreducible representations. The splitting depends on the crystal symmetry and the number of 4f electrons. The latter dependence can be demonstrated by symmetry considerations (Kramers theorem).

As a consequence, the RE ions are separated into two groups; Kramers ions with an odd number of electrons and non-Kramers ions with an even number of electrons. It can be proven that for Kramers ions, the degeneracy is at least two fold, and that splitting occurs into $(J+1/2)$ different levels. This form of degeneracy

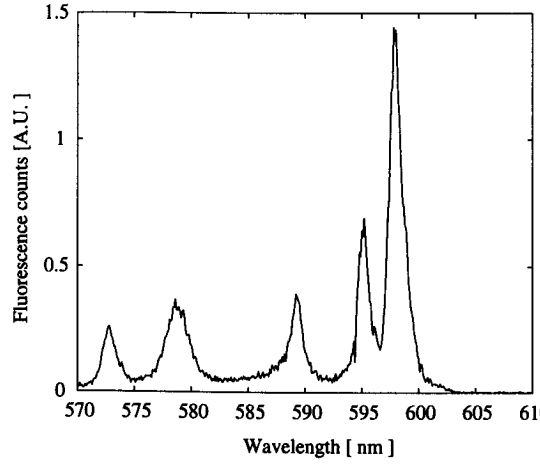


**Figure 2.1:** Excitation spectrum of $Pr^{3+}$ : $CaTiSiO_5$ . Shown is the Stark level splitting of the excited state $^1D_2$. The site symmetry is $C_1$, with a corresponding splitting into $2J + 1 = 5$ Stark levels. Here, the five transitions are clearly separated. The measurement was performed at 12 K.

is usually referred to as Kramers doublets. Kramers ions have magnetic moments on the order of the Bohr magnetron $\mu_B$ and the ions that belong to this this category are $Ce^{3+}$, $Nd^{3+}$, $Sm^{3+}$, $Dy^{3+}$, $Er^{3+}$, and $Yb^{3+}$.

For non-Kramers ions, except in sites of axial or higher crystal symmetry the $J$ degeneracy is totally removed leading to $(2J+1)$ Stark levels. Additionally, the angular momentum is quenched by the crystal field. Van Vleck demonstrated that for non-Kramers ions all time odd operators, i.e. operators that become negative upon time reversal [28], are quenched. The ions belonging to the non-Kramers group are, $Pr^{3+}$, $Pm^{3+}$, $Eu^{3+}$, $Tb^{3+}$, $Ho^{3+}$, and $Tm^{3+}$. Proofs of the Kramers theorem and the Van Vleck theorem can be found in Ref. [28].

An example of Stark level splittings for $Pr^{3+}$ is shown in Fig. (2.1). With a site symmetry of $C_1$ the degeneracy of the excited state $^1D_2$ is fully lifted and the five Stark levels are clearly resolved.

**(iii) Hyperfine.** For weak ligand fields the hyperfine coupling Hamiltonian within one $J$ state can be approximated by

$$\mathscr{H}_{\rm HF} = A_J \mathbf{I}\,\mathbf{J}\ , \tag{2.4}$$

where $A_J = 2\mu_B\gamma_N\hbar\langle r^{-3}\rangle\langle J||N||J\rangle$ is the magnetic hyperfine constant. $2\mu_B\langle r^{-3}\rangle N$ represents the field at the nucleus due to the f-electrons and $\langle r^{-3}\rangle$ is the mean inverse third power of the distance of the electron from the nucleus. The quantity $\langle J||N||J\rangle$ is the reduced matrix element and is tabulated for the ground states of all 4f ions [28]. Concentrating on non-Kramers ions in low symmetries the rhs of Eq. (2.4) vanishes since $\mathbf{J}$ is a time odd operator. In this case the second order term needs to be considered, which arises through admixture from different $|LSJ\rangle$ manifolds.

**(iv) Quadrupole and pseudo quadrupole terms.** It was shown by Teplov [29], that the second order hyperfine term is formally identical to a quadrupole Hamiltonian $\mathscr{H}_Q(x,y,z)$. It is therefore referred to as the pseudo-quadrupole Hamiltonian $\mathscr{H}_{PQ}(x',y',z')$. The $(x,y,z)$ and $(x',y',z')$ indicate the principal axes in which the quadrupole and pseudo-quadrupole Hamiltonian are diagonal. The two Hamiltonians can be summarized into a single effective quadrupole Hamiltonian $\mathscr{H}_{Q'}$ which

can be written as

$$\mathscr{H}_{Q'}(x'', y'', z'') = D\left([I_{z''}^2 - I(I+1)/3] + \frac{\bar{\eta}}{3}[I_{x''}^2 - I_{y''}^2]\right). \tag{2.5}$$

Here $D$ denotes the effective quadrupole constant and $\bar{\eta}$ the effective field gradient parameter. In general, the principal axes do not coincide in the electronic ground and excited states which leads to a mixing of the wave functions. This has an impact one the selection rules as shall be shown below.

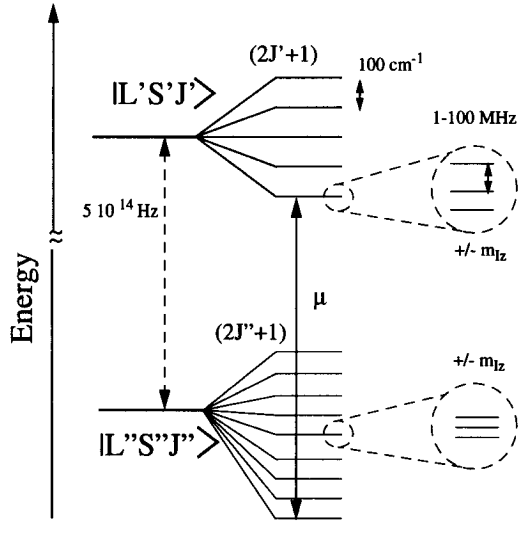


**Figure 2.2:** Level structure for a non-Kramers ion in a low symmetry crystal field. As an example, one may consider $Pr^{3+}$ ($I_{pr} = 5/2$) in $Y_2SiO_5$ (site symmetry $C_1$) for the $^1D_2 - {}^3H_4$ transition in zero magnetic field. This corresponds to one of the transitions studied in this work. The nuclear spin of the RE ion leads to a splitting of the individual Stark levels into $(2I+1)/2$ states. The splitting is usually masked by the inhomogeneous broadening of the absorption band, but can be resolved using techniques such as persistent spectral hole burning or optically detected NMR (ODNMR).

The splittings of the levels that are determined by the effective quadrupole Hamiltonian are usually referred to as hyperfine splittings, a convention that will be followed here, too. Nevertheless, the name is somewhat misleading since the hyperfine splitting is caused by a combination of a quadrupole and second order hyperfine term. The number of splittings depends on the dimension of the irreducible representation of the corresponding state and the magnitude of the nuclear spin. An example of a level splitting for a non-Kramers ion in a low symmetry crystal field is

depicted in Fig. (2.2). The given level structures approximate the order of magnitude of the different contributions.

### 2.2.2 Time-dependent Hamiltonian

Dynamical interactions have only recently become a big field of interest in the studies of RE ion doped crystals. Similarly to the previously discussed terms, they can be treated as perturbation terms since their contributions to the energy shifts are in the kHz range. Dynamical contributions manifest themselves in a change of the optical transition frequency within the experimental time scale.

For the analysis the following Hamiltonian is considered:

$$\mathscr{H}_1(t) = [\mathscr{H}_{\mathrm{SI}}(t) + \mathscr{H}_{\mathrm{TLS}}(t)] + [\mathscr{H}_{\mathrm{NQP}}(t) + \mathscr{H}_{\mathrm{EFS}}(t)]. \tag{2.6}$$

The first parenthesis covers, (i) $\mathscr{H}_{\mathrm{SI}}(t)$ which describes the interaction of the RE ion with the surrounding nuclear spins, and (ii) $\mathscr{H}_{\mathrm{TLS}}(t)$ takes into account the coupling to two level systems (TLS). These contributions can be regarded as intrinsic for a given crystal and a fixed temperature.

The second parenthesis contains (iii) the non-equilibrium phonon term $\mathscr{H}_{\mathrm{NQP}}(t)$ and (iv) $\mathscr{H}_{\mathrm{EFS}}(t)$ which describes effects arising from ion-ion interactions between different RE ions and derives from excitation induced frequency shifts (EFS). $\mathscr{H}_{\mathrm{NQP}}(t)$ and $\mathscr{H}_{\mathrm{EFS}}(t)$ are functions of the excitation light, and are thus connected to extrinsic properties.

Each of these factors has been studied extensively over the last ten years and is discussed individually throughout this work. This is started by formally writing down the different Hamiltonians. The effect on the optical transition linewidth will be analyzed in Chapters 3 and 7. Generally, the Hamiltonian $\mathscr{H}_1(t)$ can be written as

$$\mathscr{H}_1(t) = \sum_q \hat{F}^{(q)}(t)\hat{A}^{(q)} , \tag{2.7}$$

where the $\hat{A}^{(q)}$ are operators exclusively acting on a RE ion. While in a quantum mechanical relaxation theory the $\hat{F}^{(q)}(t)$ are operators of the surrounding, these quantities are taken as classical random variables in a semi-classical approach as it is chosen here.

**(i) Spin-ion interactions** have long been known to be a source of strong broadening contributions in solids and have been largely investigated using NMR or optical techniques.

The secular part of the heteronuclear Hamiltonian of the $j$th guest ion, responsible for dephasing can be written as [24]

$$\mathscr{H}_{\mathrm{SI,gh}}(t) = -\gamma_I \gamma_S \hbar \sum_k \frac{3\cos^2\theta_{kj} - 1}{r_{kj}^3} \mathcal{I}_z \mathcal{S}_{kz}(t), \tag{2.8}$$

where the index gh indicates the coupling of the $j$th guest (g) ion with nuclear spin operator $\mathcal{I}$, to the $k$th host (h) ion with nuclear spin operator $\mathcal{S}_k$. In expression (2.8) the flip flop terms are omitted because of different Larmor frequencies. Finally, the $\gamma$'s are the gyromagnetic ratios and $(\theta, r)_{jk}$ denote the angle and radial distance between the two ions, respectively. Writing Eq. (2.8), the interaction is assumed to be of dipolar form. The secular part of the homonuclear host-host coupling reads

$$\mathscr{H}_{\mathrm{SI,hh}}(t) = -\gamma_S^2 \hbar \sum_{k<j} \frac{3\cos^2\theta_{kj} - 1}{r_{kj}^3} \left[ \mathcal{S}_{kz}\mathcal{S}_{jz} - \frac{1}{4}(\mathcal{S}_k^+ \mathcal{S}_j^- + \mathcal{S}_k^- \mathcal{S}_j^+) \right], \tag{2.9}$$

where the raising and lowering operators $\mathcal{S}_k^{\pm}\mathcal{S}_j^{\mp}$ reveal the mutual spin flip processes. Due to the flipping of host ion pairs, $\mathcal{S}_{kz}(t)$ fluctuates in time, resulting in a wobbling of the the transition frequency of the $j$th guest ion. In cases where the gyromagnetic constants of the guest- and host-ions are comparable, the homonuclear guest-guest term can be neglected. Semi-classically, the interaction Hamiltonian can thus be written as

$$\mathscr{H}_{\mathrm{SI,j}}(t) = \hbar \sum_{i=1}^{N} \delta\omega_{ji}^{\mathrm{SI}}(t) \sigma_z^j \,, \tag{2.10}$$

where $\sigma_z^j = \frac{1}{2}(|2\rangle\langle 2| - |1\rangle\langle 1|)$ is the third Pauli matrix and $|2\rangle$, $|1\rangle$ denote the electronic ground and excited state wave function of the RE ion, respectively. Finally,

$N$ runs over all the surrounding host ions and $\delta\omega_{ji}^{\mathrm{SI}}(t)$ denotes the frequency shift due to the coupling of the $j$th RE ion to the $i$th host ion.

**(ii) Tunneling two-level systems.** The temperature dependence of RE ion transitions can show up in different forms, namely in the phonon densities or the interaction with matrix given tunneling two-level systems (TLS). Although the physical origin of TLS's has not yet been clarified, their postulation has permitted the elucidation of different experimental observations in the field of solid state physics. So it was possible to explain the linear temperature dependence of the heat capacity of glasses in terms of the standard TLS model [30].

Formally, the Hamiltonian describing the coupling of the $j$th RE ion to an ensemble of $N$ TLS's can be approximated by [31,32]

$$\mathscr{H}_{\mathrm{TLS,j}}(t) = \hbar \sum_{i=1}^{N} \delta\omega_{ji}^{\mathrm{TLS}}(t)\sigma_z^j \,, \tag{2.11}$$

making use of the notation introduced above. The total frequency shift depends on various factors such as the magnitude of the interacting dipoles and on the spatial TLS distribution.

**(iii) Non-equilibrium phonons.** In contrast to equilibrium phonon distributions which are strongly temperature dependent, the distributions of non-equilibrium phonons (NQP) mostly depend on the efficiency with which they are generated through external excitation and internal relaxation (paths of non-thermally activated centers in the crystal). Longitudinal acoustic phonon relaxations are governed by spontaneous splitting processes, which have to occur under energy and momentum conservation. It was shown by Orbach and Vredevoe and by Klemens that the anharmonic lifetimes of longitudinal high frequency acoustic phonons (frequencies above 1 THz) decrease as the inverse of the fifth power of frequency [33,34]. For $Eu^{2+}$ doped $CaF_2$ such a frequency dependence was measured by Baumgartner et al., and lifetimes close to 1 $\mu$s were observed for longitudinal high frequency phonons around 1.5 THz [35]. Thus, the life times of the NQP become comparable to typical dephasing times and the broadening can not be treated using fast exchange theory

as it is done in the case of equilibrium phonons [27].

**(iv) Excitation induced frequency shifts (EFS).** For a long time, guest-guest interactions had been ignored in RE ion spectroscopy since these contributions, at dilutions in the range of $10^{-4}$ were considered to be very small. However, studies over the last years have revealed that line broadening of a few kHz can emerge from ion-ion interactions. Two main forms of EFS can occur: one being purely off-resonant, where the change in the transition frequency occurs due to a change of state of the interacting neighboring ions. This is referred to as diagonal contribution. The other contribution is of resonant type, namely the off-diagonal term, which results from a shift of the energy levels due to coupling to a resonant and spatially nearby state. The discussion presented here is based on a dimer treatment which is then generalized to $N$ states.

**(iv.i) Diagonal interaction.** Single-ion wave functions $\phi_{jg}$ and $\phi_{je}$ are considered for the electronic ground and excited states of ions located at site $j$ and site $k$, respectively. The hyperfine splittings are ignored. Using the single ion basis functions the dimer interaction of the diagonal type can be written as

$$\left\langle \phi_{jx}\phi_{ky}|\hat{V}|\phi_{jx}\phi_{ky}\right\rangle \quad , \quad x,y \in \{g,e\} \, , \tag{2.12}$$

where $\hat{V}$ is the operator of the electronic interaction. The combination of the four integrals of this type leads to the shift $\delta\omega_{jk}$ in the transition frequency of an ion $j$ due to the excitation of another ion $k$ which thus reads [36]

$$\begin{aligned} \delta\omega_{jk} \;=\; & \left\langle \phi_{je}\phi_{ke}|\hat{V}|\phi_{je}\phi_{ke}\right\rangle - \left\langle \phi_{je}\phi_{kg}|\hat{V}|\phi_{je}\phi_{kg}\right\rangle \\ & -\left\langle \phi_{jg}\phi_{ke}|\hat{V}|\phi_{jg}\phi_{ke}\right\rangle + \left\langle \phi_{jg}\phi_{kg}|\hat{V}|\phi_{jg}\phi_{kg}\right\rangle \; . \end{aligned} \tag{2.13}$$

Using a two-center expansion the integrals can be approximated by electric and magnetic dipole or multipole interactions. Up to the first order, the frequency fluctuation arises due to a difference of electric and magnetic moments of the ions

in the ground and excited state, respectively.

The dimer interaction can be easily extended to the interaction of the $j$th guest ion with an ensemble of guest ions which reads

$$\mathscr{H}_{\mathrm{EFS-D_j}}(t) = \hbar \sum_k{}' \delta\omega_{jk}^{\mathrm{EFS}}(t)\sigma_z^j \ . \tag{2.14}$$

From a comparison of Eqs. (2.10), (2.11) and (2.14) it is clear that all equations have the same structure. However, their physical origins and distributions are quite different.

**(iv.ii) Off-diagonal interaction.**

In this case the dimer interaction term reads [37]

$$J_{jk} = \left\langle \phi_{je}\phi_{kg}|\hat{V}|\phi_{jg}\phi_{ke} \right\rangle \ , \tag{2.15}$$

where due to the static interaction of two almost degenerate levels, splitting occurs. The relevant Hamiltonian can be written in a $4 \times 4$ basis as [38]

$$\mathscr{H}_{\mathrm{dimer}} = \hbar \left(\bar{\omega}_1|1\rangle\langle 1| + \bar{\omega}_2|2\rangle\langle 2| + \bar{\omega}_3||3\rangle\langle 3|\right). \tag{2.16}$$

The definition of the states becomes clear from Fig. (2.3). Shown are the non-zero dipole moment matrix elements. The $|0\rangle\langle 0|$ energy is chosen at the zero energy level. States $|1\rangle$ and $|2\rangle$ are near resonance with the laser frequency $\omega_1$ while state $|3\rangle$ is near resonance with $2\omega_1$. The intermolecular coupling is assumed to be weak and static. One can then write

$$\mathscr{H}' + \mathscr{H}_{\mathrm{J}} = [\epsilon\ a_1^+ a_1 + (\epsilon + \delta\epsilon)\ a_2^+ a_2] + [J_{12}\ (a_1^+ a_2 + a_1 a_2^+)] \tag{2.17}$$

where $\mathscr{H}'$ denotes the dimer Hamiltonian for $J_{12} = 0$. $a_i^+$ and $a_i$ are the fermionic creation and annihilation operators, and $\epsilon$ and $(\epsilon + \delta\epsilon)$ represent the energy difference of the first and the second transition, respectively [38]. The Hamiltonian can then be transformed into the diagonal basis of Eq. (2.16), which requires the diagonalization of a $2 \times 2$ matrix, since $J_{12}$ is the only off-diagonal element. This

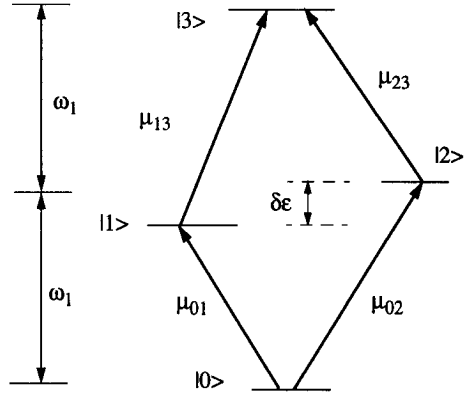


**Figure 2.3:** Four level scheme of two weakly coupled ions close in resonance to a laser field of frequency $\omega_1$. Shown are the non-vanishing transition dipole moments.

yields the eigenvalues

$$\bar{\omega}_{1,2} = \frac{1}{\hbar}\left[\epsilon + \left(\delta\epsilon/2 \pm \sqrt{J_{12}^2 + (\delta\epsilon/2)^2}\right)\right] \text{, and } \bar{\omega}_3 = \frac{1}{\hbar}(2\epsilon + \delta\epsilon). \tag{2.18}$$

The extension to the resonant interaction of all $N$ ions is involved and requires the diagonalization of a $2^N \times 2^N$ matrix. Here, the fully coupled system will be approximated by sums of independent ion-pair interactions. For each pair, the frequency shifts are calculated independently. This corresponds to a sum over $N(N-1)/2$ independently diagonalized $(4 \times 4)$ matrices. In Chapter 7, the conditions are presented for which this approximation is justified in the analysis of line broadening.

### 2.2.3 Inhomogeneous line width and energy levels

In the preceding Paragraphs the different contributions which can lead to dynamical changes of the resonance frequency or the "homogeneous" linewidth were presented. The name homogeneous linewidth in principle implies that all ions have the same lineshape and width. As single molecule experiments have revealed, this is not the

case and distributions of "homogeneous" linewidths are observed [39]. These distributions are caused by different fluctuating fields felt by each chromophore. In this sense what was earlier defined as the homogeneous linewidth depends (a) on the time scale of observation and (b) on the "individual" temporal frequency trajectory of the ions or molecules. What is usually referred to as the inhomogeneous distribution can thus be interpreted as the distribution of time trajectories of single atoms frequencies with fluctuations much smaller than the inhomogeneous linewidth for typical experimental time scales (femto seconds - few months). Various mechanisms can lead to slow or time independent frequency shifts. Most commonly one can think of different local environments leading to shifts in the resonance frequencies. These different local surroundings are caused by lattice strains inherent in all crystals, since they solidify at finite temperatures. The linewidth of the inhomogeneous broadening ranges from GHz in crystals to several nm in glasses. The observed linewidth is thus either dominated by the inhomogeneous broadening or is given by the homogeneous linewidth. For RE doped crystals, at room temperatures the inhomogeneous contributions are totally masked by phonon induced homogeneous linewidths (governed by thermalized phonons). At cryogenic temperatures however, thermal phonons are often negligible, but broadening due to spontaneous phonon emission becomes very important for all except the lowest components of the J-manifolds. The upper field components of the J-manifold are usually separated from the lowest one by energies of several 10's to100's of wavenumbers. These correspond to typical phonon energies in crystals. The transitions are homogeneously broadened with linewidths ranging from 1-100 GHz, with the magnitude depending on the electron-phonon coupling, energy spacing and phonon densities. Since the energy separation between the lowest level of a $J$-manifold and the next lower lying level belonging to another $J$-manifold is usually larger than the maximal phonon frequency, multi-phonon, spontaneous or stimulated emission is required for such relaxation processes. Typically this results in population decay times ($T_1$) of $10^{-8} - 10^{-3}$s. In the following Chapters it is shown that dynamically induced broadenings often range from Hz to a few kHz, implying that these contributions become comparable to the lifetime limit of the linewidth. Thus, these absorption lines are dominated by the inhomogeneous broadening, yielding ratios of inhomogeneous to homogeneous linewidths as big as $10^7$, which makes frequency selective materials so attractive for optical data storage.

In Fig. (2.4) the energy level diagram, denoting the different J-manifolds is shown for all lanthanide ions in $LaCl_3$ [40]. Since the free ion term is strongly dominant, these level structures are very similar for many crystalline systems.

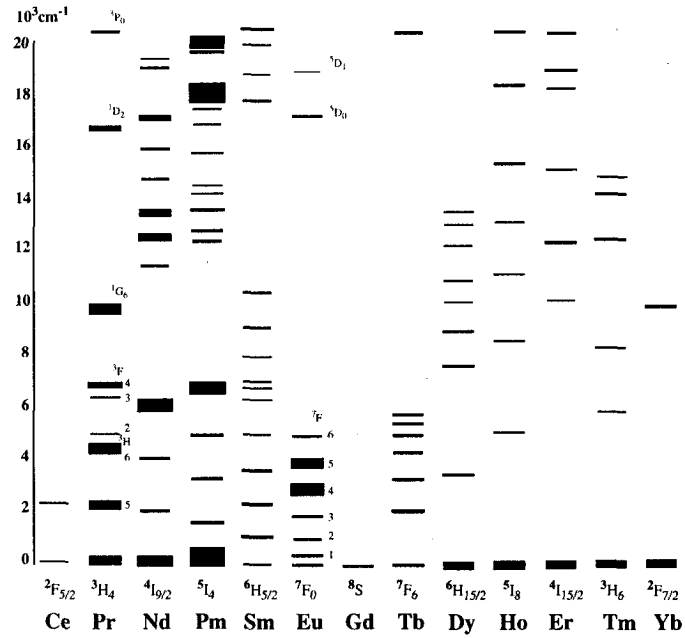


**Figure 2.4:** Energy diagram of the lanthanide ions in $LaCl_3$. Since the crystal field can be regarded as a perturbation term, the level scheme is mostly independent of the specific host crystal.

## Energy levels in $Eu^{3+} : Pr^{3+} : Y_2SiO_5$

In the following, the energy levels of $Y_2SiO_5$ crystals doped with either $Eu^{3+}$ or $Pr^{3+}$ are presented and discussed in detail since most of the studies carried out during this work were performed on these systems.

**The host:** $Y_2SiO_5$ is a widely used laser crystal, which makes it commercially available with a very high optical quality. The crystal structure, determined by

Maksimov et al. [41], is monoclinic and belongs to the $C_{2h}^6$ (C2/c; 2/m) space group. The dimensions of the monoclinic unit cell were found to be a= 10.410 Å, b=6.721 Å, c=12.490 Å and $\beta = 102.4°$. The number $Z$ of $Y_2SiO_5$ units per unit cell equals eight. This yields an approximated density of 4.35 g/cm$^3$. In Fig. (2.5) the crystal structure is reproduced using the data of Maksimov. For a substitutional cubic lattice it is possible to define an average ion-ion distance which results in an approximate distance of 2.4 Å.

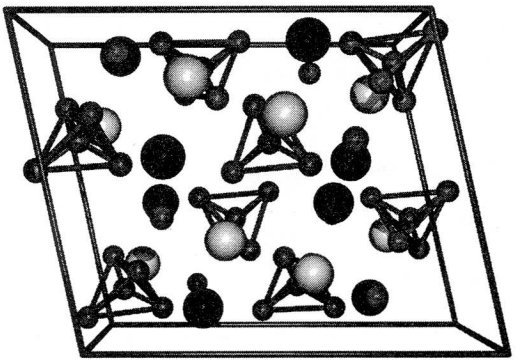

**Figure 2.5:** Crystal structure of $Y_2(SiO_4)O$. Shown is a single unit cell. The data for the positions of the atoms are taken from Maksimov et al. [41]. The silicon atoms form the centers of the tetragons with oxygens at the ends. The small spheres are the remaining 8 oxygens and the large spheres represent the 16 Yttria. The two inequivalent sites of Yttrium are colored white and black. (E.U. Wallenborn is kindly acknowledged for the generation of this Figure).

The strengths of the spin-ion coupling term is strongly determined by the magnetic moments of the host ions. In $Y_2SiO_5$ the only ions with magnetic moments are $^{89}$Y and $^{29}$Si with moments of -0.14 $\mu_N$ and -0.55 $\mu_N$, respectively. Both ions have a nuclear spin of 1/2. Since the natural abundances of $^{29}$Si and $^{89}$Y are 4.2% and 100%, respectively, and twice as many Yittria occur per unit cell, the magnetic interactions of a guest ion with Y ions is approximately 42 times stronger than that with the Si ions. The guest-host magnetic interaction is therefore expected to be

rather small in $Y_2SiO_5$ , which makes the material suited for ultra-high resolution spectroscopy.

**The guest ions** can be substituted into the two inequivalent sites of $Y^{3+}$ of site symmetry $C_1$. Ideal are substitutions by triply ionized ions since full charge compensation is obtained.

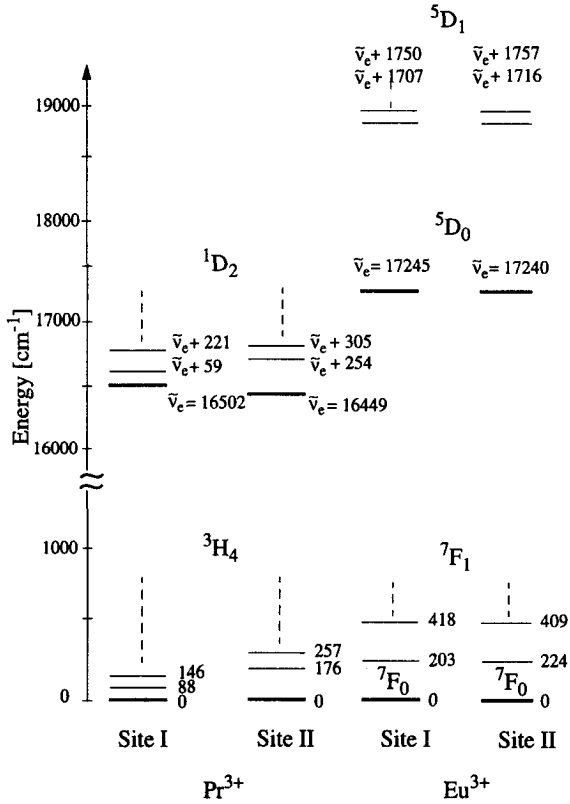


**Figure 2.6:** Level structures of $Pr^{3+}$: $Eu^{3+}$ in $Y_2SiO_5$ . Data are taken from Refs [42, 43]; all energies are given in units of wavenumbers. $\tilde{\nu}_e$ denotes the transition frequency to the state pumped by the laser. Shown are the investigated ground and excited states, along with the two closest lying Stark levels. Not shown are the hyperfine splittings of the levels which range between 3 MHz - 275 MHz. All values are given for the vacuum.

In this study, the $^1D_2 - {}^3H_4$ transition of $Pr^{3+}$ has been investigated. The transition frequencies are observed at 605.813 nm and 607.770 nm, respectively. In $Eu^{3+}$ the $^7F_0 - {}^5D_0$ transition, located at 579.879 nm and 580.049 nm have been studied. These optical transitions are shown in Fig. (2.6) along with the two closest lying Stark levels. $Eu^{3+}$ and $Pr^{3+}$ are very good candidates for the detection of small changes in the environment due to their extremely long lifetimes. On the other hand, the additional dephasing contributions are expected to be small, due to the small magnetic moments of the host ions. For $Eu^{3+}$ and $Pr^{3+}$ in $Y_2SiO_5$ the magnetic moments are not known. In the case of the free ion, for $^{141}Pr$, the only stable $Pr^{3+}$ isotope, the nuclear magnetic moment was measured as 4.2754(5) $\mu_N$ [44]. $Eu^{3+}$ has two isotopes, $^{151}Eu$ and $^{153}Eu$ of almost equal abundance (44.8% : 52.2%). The nuclear magnetic moments of the free ion $Eu^{3+}$ are 3.465(1) $\mu_N$ for $^{151}Eu$ and 1.531(2) $\mu_N$ for $^{153}Eu$. [45]. The $^7F_0 - {}^5D_0$ transition of $Eu^{3+}$ is forbidden in the free ion but becomes weakly allowed in solids through admixtures from other J levels, meaning that here the Russell-Sanders approximation of separate $|LSJ\rangle$ manifolds breaks down. The admixtures result in hyperfine induced contributions to the effective nuclear moment and to the effective quadrupole interaction. It was shown by Elliott that in the case of $Eu^{3+}$ the sign of the electronic contribution to the magnetic moment is opposite to that of the bare moment, leading to a quenching of the nuclear magnetic moments rather than an enhancement [46].

### 2.2.4 Separation of the wave function

The hierarchical splitting of the different energy contributions is given by the different magnitudes of the energy shifts induced by the crystal field, quadrupole coupling, hyperfine, and dynamical interactions. This has some important consequences for the wave function. The total wave function $|i\rangle$ in the $i$th state, being a ground ($g$) or excited ($e$) state can be approximated by a product function of the type

$$|g\rangle \simeq |1\rangle \cdot |\psi_g^{\mathrm{hf}}\rangle, \quad |e\rangle \simeq |2\rangle \cdot |\psi_e^{\mathrm{hf}}\rangle, \tag{2.19}$$

where $|1\rangle$ and $|2\rangle$ correspond to the electronic contributions and $\psi_i^{\mathrm{hf}}$ acts on the hyperfine splitting subspace. This approach is similar to the separation of molecular

modes into rotational and vibronic parts.

If the oscillations of the electric field $\mathbf{E}$ are supposed to be centered around $\omega_1$, a frequency close to the transition frequency $\omega$, one can write

$$\mathbf{E}(t,\mathbf{x}) \simeq (\boldsymbol{\epsilon}\, \mathcal{E}(t) \mathrm{e}^{-i(\omega_1 t - \mathbf{kx})} + \mathrm{c.c.})/2 \,. \tag{2.20}$$

Here, $\boldsymbol{\epsilon}$ is a unit polarization vector and $\mathcal{E}(t) = |\mathcal{E}(t)| \exp(-i\phi(t))$ is a slowly varying complex amplitude. $\mathbf{k}$ denotes the wave-vector and $\mathbf{x}$ the spatial three-dimensional coordinate. The separation performed in Eq. (2.20) corresponds to what is generally known as slowly varying envelope approximation. For simplicity, $\phi(t)$ and $\mathbf{x}$ are set to zero here. The Fourier transform of $|\mathcal{E}(t)|$ is assumed to have a narrower spectral bandwidth than the closest spectral distance between the hyperfine levels in the excited state. Further relatively low laser intensities are considered such that Rabi side bands can be neglected [47].[2] Making use of Eq. (2.20), the transition amplitude between a ground state $|g\rangle$ and an electronic excited state $|e\rangle$ thus reads

$$\begin{aligned} \langle g|\hat{\boldsymbol{\mu}} \cdot \mathbf{E}|e\rangle &\simeq \langle 1|\hat{\boldsymbol{\mu}} \cdot \mathbf{E}|2\rangle \langle \psi_{\mathrm{g}}^{\mathrm{hf}}|\psi_{\mathrm{e}}^{\mathrm{hf}}\rangle \\ &= \boldsymbol{\mu}_{12} \cdot \mathbf{E}\, \langle \psi_{\mathrm{g}}^{\mathrm{hf}}|\psi_{\mathrm{e}}^{\mathrm{hf}}\rangle = \hbar\chi \cos(\omega_1 t) \langle \psi_{\mathrm{g}}^{\mathrm{hf}}|\psi_{\mathrm{e}}^{\mathrm{hf}}\rangle \,, \end{aligned} \tag{2.21}$$

where $\hat{\boldsymbol{\mu}}$ denotes the electronic dipole moment operator and $\boldsymbol{\mu}_{12} \equiv \langle 1|\hat{\boldsymbol{\mu}}|2\rangle$. The Rabi frequency $\chi$ is given by

$$\chi(t) = \mu|\mathcal{E}(t)|/\hbar \,, \tag{2.22}$$

where $\mu \equiv \boldsymbol{\mu}_{12} \cdot \boldsymbol{\epsilon}$ is the component of the transition dipole moment along the electric field polarization. In the literature the electric field is often taken as twice the value given by Eq. (2.20). This leads to an additional factor of two in the definition of the Rabi frequency (compare for example Mandel and Wolf [47]). In cases where the approximations carried out in Eq. (2.19) and Eq. (2.21) are fulfilled it can be concluded that (i) the electronic transition properties of a RE ion can be described by a two level atom model and (ii) the transition amplitude (or effective oscillator

[2] If the total spectral bandwidth is larger than the separation of the different hyperfine levels, coherent Raman- or quantum beats will be observed [48].

strength) is determined by the overlap of the ground and the exited state hyperfine wave functions. Point (i) will be extensively exploited in the following Chapter. Here, point (ii) is discussed in a little more detail.

In order to determine the transition probabilities one must recall that the combination of quadrupole and hyperfine contributions leads to the effective hyperfine splittings. In what follows, the case of a nuclear spin $I = 5/2$ is analyzed, since this corresponds to the nuclear spin of the here investigated $Pr^{3+}$ and $Eu^{3+}$ ions. In the case of no asymmetry of the pseudo quadrupole tensor, i.e. if the effective field gradient parameter $\bar{\eta}$ in Eq. (2.5) becomes zero, the $\psi^{\rm hf}_{{\rm i},\pm m}$, (i=g, e, $\pm m = 5/2, 1/2, -3/2$) are eigenfunctions of $\mathscr{H}_{Q'}$. Generally, the eigenstates are mixed and can be written as

$$|\pm\zeta_{{\rm i},k}\rangle = \sum_m a_m |\psi^{\rm hf}_{{\rm i},\pm m}\rangle, \quad \text{with} \quad (k = 1,2,3). \tag{2.23}$$

The coefficients $a_m$ can be obtained through diagonalization of the matrix with elements

$$\langle\psi^{\rm hf}_{{\rm g},\pm m}|\mathscr{H}_{Q'}|\psi^{\rm hf}_{{\rm e},\pm m'}\rangle = \begin{cases} D\,(m_z^2 - I(I+1)/3) & : \; m'_z = m_z \\ \frac{D\bar{\eta}}{6} f_I(\pm m_z) f_I(1 \pm m_z) & : \; m_z = m'_z \pm 2 \\ 0 & : \; \text{otherwise}\,, \end{cases} \tag{2.24}$$

using $f_I^2(m_z) = (I - m_z)(I + m_z + 1)$ [49]. In general, the pseudo quadrupole axes in a diagonal basis are not congruent for the ground and excited state. Thus, an Eulerian transformation of the excited state basis set is required. The eigenstates $\xi_{{\rm e},l}$ $(l = 1,2,3)$ can then be expressed as

$$\begin{aligned} |\xi_{{\rm e},l}\rangle &= \sum_{m,m'} a_m D^{(j)}(\alpha,\beta,\gamma)_{m'\pm m} |\psi^{\rm hf}_{{\rm e},m'}\rangle, \text{ with} \\ m &= (5/2, 1/2, -3/2) \text{ and } m' = (\pm 5/2, \pm 1/2, \mp 3/2). \end{aligned} \tag{2.25}$$

The Eulerian angles for $j = 5/2$ are given in Ref. [50]. If the quadrupole parameters and the orientation of the quadrupole tensors are known, the transition probabili-

ties can be calculated using hyperfine hole burning spectra. Such an attempt was performed by various authors [51–53] and is commented on in Chapter 5.

## 2.3 Spectral hole burning

Spectroscopic investigations of RE ions consist of the traditional optically linear methods such as the measurement of absorption bands or fluorescence measurements. These methods allow for the determination of selection rules, oscillator strengths and splittings of $J$ manifolds. Non-linear optical techniques as photon echoes, quantum beats or pump-probe experiments allow for the measurement with a resolution higher than the inhomogeneous linewidth. This of course requires the homogeneous linewidths to be narrower than the inhomogeneous line, a condition clearly fulfilled in FSM at low temperatures. Alternative techniques with comparable resolution are spectral hole burning or fluorescence spectroscopy of single molecules [39]. In single molecule spectroscopy (SMS), the concentration is reduced to the point where within the spatially and spectrally probed area, only one molecule emits. This enables one to measure the fluorescence light, while scanning the laser light. SMS is currently a strongly evolving field since it permits the studies of interactions in the solid by means of a single quantum system [54].

Spectral hole burning (SHB), in contrast, yields information about the ensemble. Here a concentration change at a certain frequency location is observed. SHB can roughly be separated into two categories: transient and persistent spectral hole burning (PSHB). In the case of transient SHB the concentration change will last on the time scale of the excited or some intermediate state lifetime. Transient holes were first reported by Bloembergen et al., who introduced the term hole burning to describe the saturation behavior observed in a NMR experiment [55]. The long spin-lattice relaxation times allowed for a relatively easy measurement of the absorption change in the NMR line. Due to the much faster relaxation rate of optical transitions, it took 26 years to the first observation of a transient hole in an inhomogeneously distributed optical transition [56]. The investigations concentrated on a transient absorption change in ruby with a lifetime in the ms regime. The

first observation of PSHB in an optical transition was reported for molecular system shortly after [57,58]. In PSHB, the chromophore undergoes a a photo-reaction which leads to a shift of its absorption spectrum. This results in the observation of a "persistent hole" in the inhomogeneous spectral distribution of the educt state. Different mechanisms can lead to PSHB. In molecular systems, one usually differentiates between photo-chemical and photo-physical hole burning processes [7]. Photo-chemical hole burning means that an intramolecular configurational change leads to a shift of the absorption frequency. In photo-physical hole burning, an intermolecular reconfiguration takes place. Concentration changes can be detected with a broad variety of techniques, which have to be carefully chosen depending on the lifetime of the change, the spectral separation of educt and product, and other parameters such as the Debye-Waller factor. Since its discovery PSHB has been carried out on numerous systems and has helped to reveal different interaction mechanisms and dynamics. Additionally, it has been used very successfully as a potentially new storage technique [3]. In this work the focus is put on the PSHB mechanism observable in $Eu^{3+}$ and $Pr^{3+}$, namely hyperfine hole burning.

### Hyperfine hole burning

As shown in Fig. (2.2), typical hyperfine splittings are on average a few 1-100 MHz. These energy spacings correspond to Boltzmann temperatures of maximally a few mK. At a temperature of 1.7 K all hyperfine levels are therefore equally populated. With inhomogeneous bands of a few GHz and illuminating at a constant laser frequency $\nu_b$, all hyperfine transitions are therefore simultaneously excited, since the inhomogeneous band consists of many ions experiencing different strains which leads to shifts of the resonance frequencies. This situation is schematically sketched in Fig. (2.7). Shown are a ground and an excited state which are split into three states, as it is the case for $Eu^{3+}$ and $Pr^{3+}$ in zero magnetic field. All of the possible nine transitions will be induced with the corresponding transition amplitudes, as discussed above. This will lead to transient gratings, with a spectral separation given by the excited state hyperfine splittings.

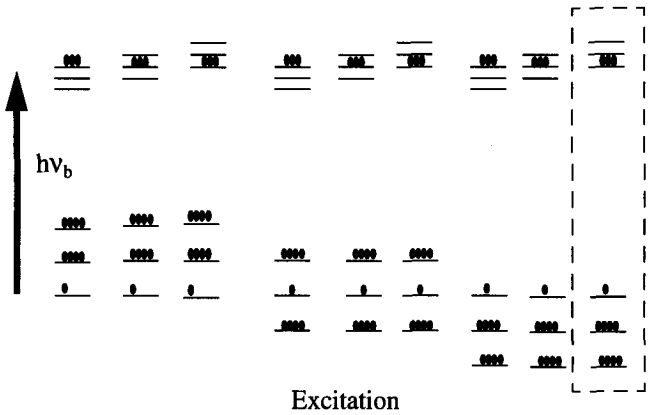


**Figure 2.7:** Hyperfine hole burning in an inhomogeneously broadened medium shown for a case of a triply split excited and ground state. Examples are $Eu^{3+}$ and $Pr^{3+}$ with a nuclear spin of $I = 5/2$ each. Due to the inhomogeneities, all of the nine possible transitions will be in resonance with the laser frequency.

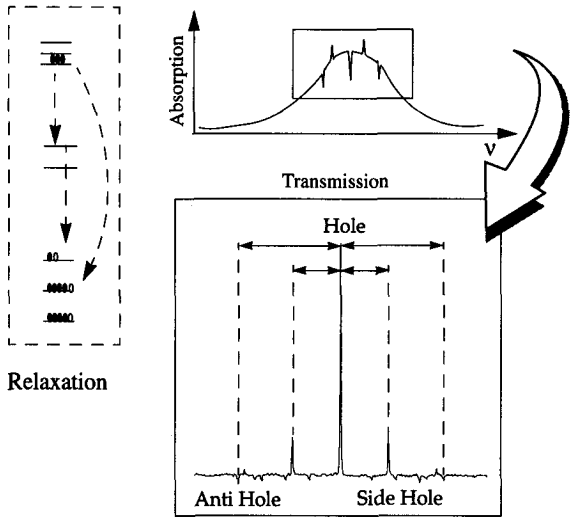


**Figure 2.8:** Hyperfine PSHB spectrum. Different relaxation paths are sketched for a single excitation path of Fig. (2.7). Relaxation can take place directly to any of the ground states, with the magnitude given by the selection rules. Redistributions within the excited states or relaxation via other intermediate levels are in principle possible. For details see text.

In the case of PSHB one needs to consider that relaxation into the ground state can occur through different paths. Each of the excited states can directly relax into any of the three ground states. Additionally, relaxation via other intermediate levels (radiative or non-radiative decays) or redistributions in the excited states can occur. This is shown in Fig. (2.8). It is clear that through excitation and relaxation a redistribution in the hyperfine levels will take place, which will manifest itself in the main spectral hole. Additionally however, in the most general case 6 side-holes and 42 anti-holes will be formed. Similarly to the main hole, the side-holes will have a decreased absorption. For the anti-holes the absorption will be increased. The Table in Fig. (2.9) presents all possible transitions which lead to a complicated hole spectrum.

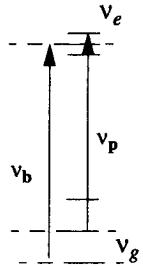


| Hole | # holes | $\nu_b$ = | $\nu_p$ = | Condition |
|---|---|---|---|---|
| Main Hole | 1 | $\nu_{ej}$-$\nu_{gi}$ | $\nu_{ej}$-$\nu_{gi}$ | i,j=1,2,3 |
| Side Hole | 6 | $\nu_{ej}$-$\nu_{gi}$ | $\nu_{ek}$-$\nu_{gi}$ | i,j,k=1,2,3 |
| Anti Hole | 6 | $\nu_{ej}$-$\nu_{gi}$ | $\nu_{ej}$-$\nu_{gk}$ | $k \neq i$ |
| Anti Hole | 36 | $\nu_{ej}$-$\nu_{gi}$ | $\nu_{ek}$-$\nu_{gl}$ | i,j,k,l=1,2,3 $k \neq j$, $l \neq j$ |

**Figure 2.9:** Hyperfine hole burning spectrum. Shown are all possible pump probe transitions for a triply split excited and ground state. This yields a total of 49 spectral holes. The $\nu_{g(e)i}$ denote the frequencies of the ith ground (excited) state.

Summarizing, it can be concluded that transient as well as persistent hyperfine hole burning are well suited for the determination of hyperfine splittings in RE ion doped crystals. In the following Chapters, different applications of hyperfine hole burning in RE ion doped crystals will be presented.

# 3. Theory of two level atoms

Optical Bloch equations for two level are theoretically described and used to calculate two-pulse photon echo intensities. It is shown how the echo intensity is affected by dynamical changes of the transition frequency. The Chapter concludes with some general remarks on the treatment of two level systems.

## 3.1 Introduction

In Section 2.2 it was shown that for a wide range of experiments, RE ions can be treated as if they consist of only two levels, namely a ground and an optically excited state. Here, the basic concepts for the understanding of the interactions of a two level atom ion with its environment are laid down [23, 59]. The Chapter is structured as follows: it begins with the description of the density matrix and the concept of reduced density matrices with an emphasis on the approximations which are made when writing optical Bloch equations [60]. Following this, the theoretical analysis of two level atoms based on optical Bloch equations is presented [61]. For a simplified case, the intensity dependence of two pulse photon echoes is evaluated. In conclusion, differences and similarities between the RE ion two level atom and a spin 1/2 system investigated in NMR are discussed.

## 3.2 Density Matrix

A closed quantum mechanical system can be characterized by pure state vectors $|\phi'(t)\rangle$'s, whose dynamics are given in terms of the time dependent Schrödinger equation

$$\frac{\mathrm{d}}{\mathrm{d}t}|\phi'(t)\rangle = \frac{1}{i\hbar}\mathscr{H}_{\mathrm{c}}|\phi'(t)\rangle, \tag{3.1}$$

where $\mathscr{H}_{\mathrm{c}}$ is the Hamiltonian for the closed system. An equivalent representation offers the density matrix formalism, where

$$\frac{\mathrm{d}}{\mathrm{d}t}\hat{\rho}_{\mathrm{c}}(t) = \frac{1}{i\hbar}[\mathscr{H}_{\mathrm{c}}, \hat{\rho}_{\mathrm{c}}(t)]\,, \tag{3.2}$$

$\hat{\rho}_{\mathrm{c}}(t) = |\phi'(t)\rangle\langle\phi'(t)|$ corresponds to the density matrix (or projector) of the pure state $\phi'(t)$ of the closed system. Expression 3.2 is usually referred to as the Liouville-von Neumann equation. In general, however, coupling to the environment is present and a unitary description of a closed system is not a valid anymore. So that, pure state vectors $\psi(t)$'s can be found for the total Hamiltonian $\mathscr{H}_{\mathrm{tot}} = \mathscr{H}_{\mathrm{c}} + \mathscr{H}_{\mathrm{s}}$ where $\mathscr{H}_{\mathrm{s}}$

includes the interaction with the environment. Generally, when probing ensembles, one is dealing with non-pure states. In this case the density matrix description is advantageous. The total ensemble density matrix operator $\langle\hat{\rho}_t\rangle$ can then be written as

$$\langle\hat{\rho}_t\rangle = \sum_i \bar{p}_i |\psi_i\rangle\langle\psi_i| \ , \tag{3.3}$$

where $\sum_i \bar{p}_i = 1$, $(0 \leq \bar{p}_i \leq 1)$ and the $\bar{p}_i$'s are probabilities. Such states are denoted as mixed states, unless $(\bar{p}_i = 1, \ \bar{p}_j = 0, \ \forall j \neq i)$. Normally, it is very difficult to handle the time evolution of $\langle\hat{\rho}_t\rangle$ since the density matrix operator is not unitary due to the irreversible coupling to the surrounding. In this case Eq. (3.2) does not apply any longer. However, for an operator $\hat{A}_t$ that acts exclusively on the subspace of $\langle\hat{\rho}_c\rangle$, i.e. $\hat{A}_t = \hat{A} \otimes \hat{1}$, the expectation value for the total density matrix $\langle\hat{\rho}_t\rangle = \langle\hat{\rho}_c\rangle \otimes \langle\hat{\rho}_s\rangle$ can still be determined and becomes

$$\langle\hat{A}_t\rangle = tr(\langle\hat{\rho}_t\rangle\hat{A}_t) = tr(\hat{\rho}_c\hat{A}) \ tr(\hat{\rho}_s) \ . \tag{3.4}$$

It is thus convenient to define a reduced density matrix $\langle\hat{\rho}\rangle \equiv \langle\hat{\rho}_c\rangle \ tr\langle\hat{\rho}_s\rangle$. It should be noted that the reduced density matrix is not unitary. Taking the trace over unobserved systems (such as a "heat bath") provides a fundamental quantum mechanical source of irreversibility. Therefore, Eq. (3.2) needs to be replaced than by a Master equation. To derive Master equations such as the Pauli or Bloch equation it is often assumed that (i) the environment acts as a bath always in thermal equilibrium (Born approximation), and (ii) that the temporal history of the process can be purely described by the last occurring event (Markov approximation) [62–65]. An excellent overview over Master equations is given by Blum [60].

## 3.3 Optical Bloch equations

Two level atoms have been studied for many years [61]. Here, the discussion is restricted to a short outline of basic concepts, focusing on the observation of two-pulse photon echoes (2PPE) which will be discussed in terms of the optical Bloch

equations. The two level atom is described by state $|1\rangle$ which corresponds to the ground state and second state $|2\rangle$, corresponding to the electronically excited state.

It was shown by Feynman et al. [66], that any two level system driven by a resonant field can be formally treated as an isolated spin 1/2 system in a magnetic field, describable through Bloch equations. The equations governing the motion are therefore referred to as optical Bloch equations, in reference to the NMR analogue [67].

For the Hamiltonian given by Eq. (2.1), the optical Bloch equations can be determined. The interaction with the bath can be treated in different forms [23]. Quite generally the Master equation can be written as

$$\frac{\mathrm{d}}{\mathrm{d}t}\hat{\rho}(t) = \frac{1}{i\hbar}[\mathscr{H}_{\mathrm{A}}(t) + \mathscr{H}_{\mathrm{I}}(t) + \hat{V}_{\mathrm{AP}}(t) + \hat{V}_{\mathrm{AE}}(t), \hat{\rho}(t)] - \hat{\hat{\Gamma}}\,[\hat{\rho}(t) - \hat{\rho}_{\mathrm{eq}}] \ . \qquad (3.5)$$

Here, $\hat{\rho}(t)$ is a reduced density matrix with the trace taken over the bath states. $\hat{\hat{\Gamma}}$ is the Liouville relaxation superoperator and accounts for the dissipative interactions which drive the density operator towards its equilibrium $\hat{\rho}_{\mathrm{eq}}$. It is a function of of different parameters such as the heuristically introduced spontaneous emission. Finally, $\hat{V}_{\mathrm{AE}}(t) = -\hat{\boldsymbol{\mu}}\mathbf{E}(t)$ denotes the interaction of the atom with the electro-magnetic field.

In what follows, an analysis of the behavior upon pulsed excitation is presented. The population is considered as constant, i.e. $\mathrm{d}(\rho_{11} + \rho_{22})/\mathrm{d}t = 0$, such that contributions like hole burning can be neglected. For the preparation the ions are excited by a first laser pulse at time $t = 0$. For simplicity, contemporaneous excitation of all frequency components is assumed, implying delta-like excitation pulse. The laser pulse is assumed to be coherent during the pulse time, implying that the laser coherence time is longer than the pulse width. The electro-magnetic field is taken from Eq. (2.20). Thus, it is considered as a classical observable. At $t < 0$ all ions are assumed to be in the ground state which is fulfilled since only electronic transitions at cryogenic temperatures are considered. Propagation effects are neglected. This corresponds to a description of a spatially and optically thin sample. Using $\tilde{\rho}_{12} \equiv \rho_{12}\exp(-i\omega_1 t)$ and neglecting non-resonant terms (rotating

wave approximation) [68], the optical Bloch equations can be written as

$$\begin{aligned}\frac{\mathrm{d}\rho_{11}(t)}{\mathrm{d}t} &= \gamma_1\rho_{22} - i\chi\left(\tilde{\rho}_{12} - \tilde{\rho}_{21}\right)\\ \frac{\mathrm{d}\tilde{\rho}_{12}(t)}{\mathrm{d}t} &= \left(-\gamma + i\Delta(t)\right)\tilde{\rho}_{12} + \frac{i\chi}{2}\left(\rho_{22} - \rho_{11}\right)\\ \frac{\mathrm{d}\rho_{22}(t)}{\mathrm{d}t} &= -\gamma_1\rho_{22} + i\chi\left(\tilde{\rho}_{12} - \tilde{\rho}_{21}\right)\ .\end{aligned} \tag{3.6}$$

The $\rho_{ij}$ denote the matrix elements of $\hat{\rho}$ and $\rho_{11}(0) = 1, \rho_{ij}(0) = 0$, otherwise. The Rabi frequency $\chi(t)$ has been defined in Eq. (2.22). $\gamma_1$ is the decay rate of the excited state population and is given by $\gamma_1 = 1/T_1$, with $T_1$ being the lifetime of the excited state. It is composed out of a radiative (spontaneous emission) and non-radiative term. $\Delta(t) = (\omega(t) - \omega_1 + \Delta_0)$ corresponds to the detuning, where $\Delta_0$ is a time independent shift of the transition frequency due to inhomogeneities in the local static fields with a distribution given by the inhomogeneous linewidth. $\omega(t)$ is composed out of the time-invariant term $\omega_0$ and $\delta\omega(t) = \sum_{\mathrm{x}}\delta\omega^{\mathrm{x}}(t)$ arising from dynamical processes. Here, the sum runs over the various interaction forms contained in $\mathscr{H}_{\mathrm{A}}(t)$ and $\hat{V}_{\mathrm{AP}}(t)$. Finally, $\tilde{\rho}_{12} = \tilde{\rho}_{21}^*$, and $\gamma$ is the lifetime limited transversal relaxation rate, limited by $\gamma = 1/(2T_1)$ [69].

For the calculation of expectation values an ensemble density matrix must be taken, since typically the experiments are carried out with $10^9 - 10^{12}$ ions. Averaging includes summation over spectral, temporal as well as spatial configurations. In order to determine the polarization the expectation of the atomic dipole moment operator $\hat{\boldsymbol{\mu}}$ needs to be calculated which can be written as [47]

$$\hat{\boldsymbol{\mu}} = \left[\boldsymbol{\mu}_{22}|2\rangle\langle 2| + \boldsymbol{\mu}_{11}|1\rangle\langle 1| + \boldsymbol{\mu}_{12}|1\rangle\langle 2| + \boldsymbol{\mu}_{21}|2\rangle\langle 1|\right]\ , \tag{3.7}$$

where $\boldsymbol{\mu}_{ij} = \langle i|\hat{\boldsymbol{\mu}}|j\rangle$ and $\boldsymbol{\mu}_{21} = \boldsymbol{\mu}_{12}^*$. Further, $\boldsymbol{\mu}_{11}$ and $\boldsymbol{\mu}_{22}$ must vanish since the dipole moment has odd parity. Thus, the ensemble polarization $\mathbf{P}(t)$ reads

$$\mathbf{P}(t) = \langle\hat{\boldsymbol{\mu}}\rangle = tr(\langle\hat{\rho}(t)\rangle\hat{\boldsymbol{\mu}}) = 2\Re(\langle\rho_{12}(t)\rangle)\Re(\boldsymbol{\mu}_{12}) + 2\Im(\langle\rho_{12}(t)\rangle)\Im(\boldsymbol{\mu}_{12})\ , \tag{3.8}$$

where $\Re$ and $\Im$ denote the real and imaginary part, respectively. Whether $\boldsymbol{\mu}_{12}$ is a complex or a real vector depends on the selection rules of the specific transition [47].

**Bloch vector representation** An equivalent representation of the optical Bloch equations (Eq. (3.6)) can be given by introducing a pseudo-spin vector $\mathbf{r}$ with its components $(r_1, r_2, r_3)$, defined as

$$\boldsymbol{r} = [2\Re(\tilde{\rho}_{12}), 2\Im(\tilde{\rho}_{12}), (\rho_{22} - \rho_{11})]. \tag{3.9}$$

For convenience, the transformation into a rotating frame has been performed directly. The introduction of the damping terms is in principle straight forward and leads to a temporal decrease of the Bloch vector components towards zero. For simplicity they are omitted for the moment. In this case, the optical Bloch equations can be written as [66]

$$\begin{aligned} \frac{\mathrm{d}\mathbf{r}}{\mathrm{d}t} &= \mathbf{Q} \times \mathbf{r}, \\ \text{with } \mathbf{Q} &= [\chi \cos\phi(t), \chi \sin\phi(t), \Delta(t)] \,, \end{aligned} \tag{3.10}$$

where $\phi(t)$ is the phase factor of the electric field envelope (see Eq. (2.20)). $|\mathbf{Q}| = [\chi^2 + \Delta^2]^{1/2}$ is sometimes addressed as the generalized Rabi frequency [61]. Thus, the pseudo-spin vector $\mathbf{r}$ precesses around the vector $\mathbf{Q}$ at a rate determined by the generalized Rabi-frequency.

### 3.3.1 Two-pulse photon echoes

By means of Eq. (3.10) the formation of a 2PPE can be easily visualized. This is illustrated in Fig. (3.1). Again, the case is considered where at time $t < 0$ all ions are in the ground state, i.e. $\mathbf{r} = [0, 0, -1]$. Here, a Rabi frequency $\chi(t)$ much bigger than the inhomogeneous linewidth $\sigma_\nu$ is further assumed.[1] At $t = 0$, an electric field pulse is switched on. The strengths of the pulse is measured through its area $\vartheta(t)$

[1] For typical parameters used in a RE experiments - (i) a Rabi frequency up to 10 MHz, (ii) an inhomogeneous linewidth $\sigma_\nu \sim 10$ GHz, and (iii) a pulse length of approximately $1\mu$s, - $\chi \ll \sigma_\nu$. This implies that $\chi \gg \Delta$, corresponding to a $\mathbf{Q}$ vector in the $(r_1, r_2)$ plane after a $\pi/2$ pulse, is only fulfilled for a small fraction of ions. For the visualization of the principle effect however, this assumption is good enough. It will not be used in the calculation of the 2PPE intensity, performed below.

which is given by

$$\vartheta(t) = \int_{-\infty}^{t} \chi(t')\mathrm{d}t' \,, \tag{3.11}$$

Here the case is considered where the pulse area of the first excitation pulse equals ($\vartheta_1 = \pi/2$). Thus, $\mathbf{r} = [0, 1, 0]$, right after, with the alignment along $r_2$ given by the choice of $\phi$. This is shown in Fig. (3.1)(a).

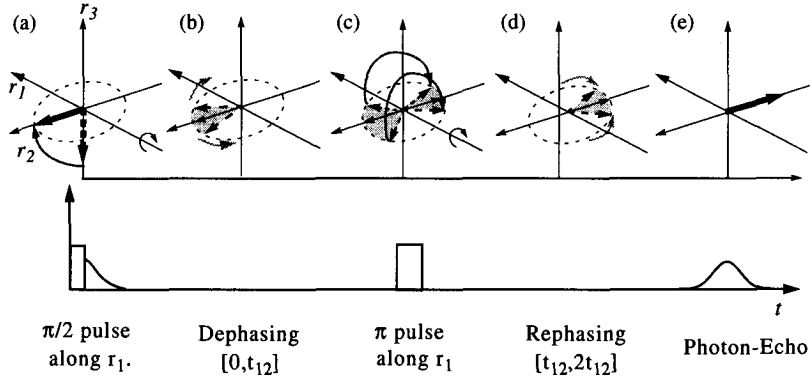


**Figure 3.1:** Formation of two pulse photon echoes (2PPE). At $t = 0$, a pulse with an area of $\vartheta_1 = \pi/2$ is applied along $r_1$ leading to a pure $r_2$ coherence term. During the dephasing period the different isochromates evolve at frequencies $\Delta_j(t)$, which leads to a vanishing macroscopic polarization. Application of a $\pi$ pulse leads to flipping of all Bloch vectors around $r_1$. Partial recovery of the macroscopic polarization can be observed at time $2t_{12}$, where the magnitude depends on the frequency history of the different $\Delta_j$'s. Below the excitation pulses and the response of the medium are sketched. The dephasing can be observed in the optical free induction decay (OFID). The drawn shapes for the OFID and the 2PPE are typical for $\sigma_\nu \ll \chi$. Further details are described in the text.

Between the first and the second excitation pulse the Bloch vectors of "isochromatic" ions freely precesses around $\mathbf{Q} = [0, 0, \Delta_j(t)]$, where $\Delta_j(t)$ denotes the frequency of the isochromate $\mathbf{r}^j$ in the rotating frame. In principle there is no difference between the use of an isochromate and a single ion density matrix since the states have exactly the same projector (compare Eq. (3.3)). Due to the inhomogeneous frequency distribution and different dynamical interactions effecting the evolution of $\mathbf{r}_j(t)$, dephasing occurs ( Fig. (3.1)(b)). This leads to a vanishing of the macroscopic

polarization which is schematically illustrated in the lower part of Fig. (3.1). At time $t_{12}$, a second pulse is applied along $r_1$, with an area of ($\vartheta_2 = \pi$). This corresponds to a transformation $\mathbf{r}(t_{12}) = [r_1, r_2, r_3]_- \rightarrow [r_1, -r_2, r_3]_+$, where the minus (plus) sign denotes the time before (after) the second excitation pulse. This is illustrated in Fig. (3.1)(c). The $r_2$ components of all Bloch vectors will experience a phase shift of $\pi$ whereas $r_1$ will be kept fixed. For $\tilde{\rho}_{12}$ this corresponds to a transformation to the complex conjugate. As during the dephasing period, the rephasing is governed by free precession of the different isochromates (Fig. (3.1)(d)). In the special case where the $\Delta_j$'s do not vary on the experimental time scale, all isochromates will perfectly rephase at time ($t = 2t_{12}$) and thus lead to a macroscopic polarization along -$r_2$ (Fig. (3.1)(e)). This can be experimentally observed and is known as two-pulse photon echo (2PPE) [18,19]. For delta-like excitation pulses, the echo pulse shape is mirror symmetric around $2t_{12}$ and equal to the shape of the OFID for $t > 2t_{12}$.

Up to now the discussion was restricted to the $\sigma_\nu \ll \chi(t)$ regime. As pointed out earlier, for typical experimental parameters in a RE ion doped crystals experiments, the inhomogeneous width is always much bigger than the Rabi frequency. This has some important consequences on the shape and length of the OFID and the 2PPE [70]. Below, the case of a collinear 2PPE using delta-like $\pi/2$, $\pi$ excitation pulses in the limit $\sigma_\nu \gg \chi(t)$ is discussed. The treatment is not generally applicable but is rather meant to introduce the different terms which are analyzed in later Chapters. Investigations of the effect of finite excitation pulse widths or arbitrary pulse areas can be found in Refs. [71–73]. Based on the consideration made above, the coherence term of the $j$th isochromate after the first excitation pulse can be written as $\tilde{\rho}^j_{12}(0) = \rho_{j0}$, where $\rho_{j0}$ depends on the detuning or offset $\Delta_j(t)$ and the Rabi frequency $\chi$ . In the case of $\sigma_\nu \ll \chi$, $\rho_{j0}$ again reduces to $i$. The free precession during the dephasing can be easily solved by integration of Eq. (3.6). This yields

$$\tilde{\rho}^j_{12}(t_{12})_- = \rho_{j0} \exp\left[-\gamma t_{12} + i \int_0^{t_{12}} \Delta_j(t')\mathrm{d}t'\right], \tag{3.12}$$

following the notation introduced before. As pointed out earlier, application of a $\pi$-pulse corresponds to taking the complex conjugate of Eq. (3.12). The value right after the second pulse serves as the starting condition for the rephasing period. Thus, rephasing can be computed in exactly the same manner as the dephasing by

substituting $(0 \rightarrow t_{12})$. At $(t = 2t_{12})$ this yields

$$\rho_{12}^{j}(2t_{12}) = \rho_{j0}^{*} \exp\left[(i\omega_1 - \gamma)2t_{12} + i\int_{t_{12}}^{2t_{12}} \omega_j(t')\mathrm{d}t' - i\int_{0}^{t_{12}} \omega_j(t')\mathrm{d}t'\right], \quad (3.13)$$

where the transformation back into the laboratory frame has been additionally performed. The contribution of the static inhomogeneity $\Delta_{0j}$ vanishes at $t = 2t_{12}$, since it is constant on the time scale of the experiment. However, at times different from $2t_{12}$, $\rho_{12}^{j}$ is strongly affected by $\Delta_{0j}$. This has to be taken into account, if 2PPE structures are calculated.

Using Eq. (3.8) and Eq. (3.13) The macroscopic polarization for a pulse separation $t_{12}$ becomes

$$\begin{aligned}\mathbf{P}(2t_{12}) = \exp(-2\gamma t_{12})\,[&\Re(\boldsymbol{\mu}_{12})\Re(\exp(i\omega_1 2t_{12})R(t_{12})) \\ &+\Im(\boldsymbol{\mu}_{12})\Im(\exp(i\omega_1 2t_{12})R(t_{12}))]\end{aligned} \quad (3.14)$$

$$\text{with} \quad R(t_{12}) = \langle \rho_0^{*} \exp\left(i\Phi(t_{12})\right)\rangle, \quad (3.15)$$

$$\text{and} \quad \Phi(t_{12}) = \left(\int_{t_{12}}^{2t_{12}} \omega(t')dt' - \int_{0}^{t_{12}} \omega(t')dt'\right).$$

The average in Eq. (3.15) has to be taken over the temporal realizations of $\omega(t)$, over the spectral density of the ion transition, and over the spatial realizations of the environmental configurations of the RE ions. In writing Eq. (3.14) it was implicitly assumed that $\langle \exp(-2\gamma t_{12})\rangle = \exp(-2\gamma t_{12})$, i.e. that all decays can be described by a single decay rate. Experimentally observed fluorescence decays show a perfectly exponential behavior, therefore justifying the assumption of a single $T_1$.

Averaging over the exponential term arises due to different dynamical interactions. Assuming that these dynamical changes are invariant upon a change in the frequency position by a few Rabi frequencies, the average over $\rho_0^{*}$ and $\Phi$ can be carried out independently and Eq. (3.15) can be rewritten as

$$R(t_{12}) = \langle \rho_0^{*} \rangle \langle \exp(i\Phi(t_{12}))\rangle. \quad (3.16)$$

In Chapter 7, the validity of this separation will be tested for the here discussed systems. Since the inhomogeneous band is very broad compared to the excitation bandwidth, the frequency distribution can always be regarded as symmetric and extended to infinity for all locations of excitation within the band. The frequency average over $\rho_0^*$ then becomes

$$\langle \rho_0^* \rangle_\Delta = \int_{-\infty}^{\infty} \rho_0^*(\Delta) g(\Delta) \mathrm{d}\Delta = -i \int_0^{\infty} 2\Im(\rho_0(\Delta)) g(\Delta) \mathrm{d}\Delta \ , \tag{3.17}$$

where $g(\Delta)$ denotes the normalized frequency distribution of the inhomogeneous line. i.e. $\int_{-\infty}^{\infty} g(\Delta)\mathrm{d}\Delta = 1$. The second equality holds since $\rho_0^*(-\Delta) = -\rho_0(\Delta)$ and $g(\Delta)$ is an even function of $\Delta$. It is worth noticing that the very large inhomogeneous linewidth leads to a vanishing real component of $\langle \rho_0^* \rangle_\Delta$.

The photon echo intensity $I(t)$ is given by the square of the polarization at time $2t_{12}$ [23] and can be calculated using Eq. (3.14) and Eq. (3.15). It is sometimes argued that only the real part of $\langle \exp(i\Phi(t_{12})) \rangle$ needs to be considered, since the frequency fluctuations are random and thus are equally probable for positive and negative fluctuations which leads to a vanishing imaginary part [74]. Generally, a complex function $R(t_{12})$ can be written in polar coordinates which reads

$$R(t_{12}) = |R(t_{12})| \exp(i\varphi') \ . \tag{3.18}$$

This enables one to write the echo intensity as

$$\begin{aligned} I(2t_{12}) = \mathbf{P}(2t_{12})^2 = \exp(-2\gamma t_{12}) |R(t_{12})|^2 \cdot \\ \cdot \left[ \Im(\boldsymbol{\mu}_{12})^2 \langle \sin^2(\omega_1 2t_{12} + \varphi') \rangle + \Re(\boldsymbol{\mu}_{12})^2 \langle \cos^2(\omega_1 2t_{12} + \varphi') \rangle \right] \end{aligned} \tag{3.19}$$

Since $\omega_1$ is an optical frequency with oscillations much faster than any detector's response time, only time averages need to be considered, which finally yields

$$I(2t_{12}) \sim |\mathbf{P}(2t_{12})|^2 \ \sim \exp(-2\gamma t_{12}) |R(t_{12})|^2 \ . \tag{3.20}$$

In the literature, the $\langle \exp(i\Phi(t_{12})) \rangle$ term is often written as the complex conjugate of the expression given in Eq. (3.15). This corresponds to a negation of the frequency $\omega$ at time $(t = t_{12})$ rather than a negation of the phase before $(t = t_{12})$. Since according

to Eq. (3.20) the echo intensity is proportional to the square of the absolute of $R(t_{12})$, one may use either forms in order to calculate the echo intensity. Thus, throughout this work both notations will be used.

Eq. (3.14), Eq. (3.15), and Eq. (3.20) show that the task of calculating 2PPE intensities largely reduces to solve $R(t_{12})$ for different types of perturbations. In Chapter 6 and Chapter 7 solutions of the specific problems of deterministic perturbations, of excitation induced lattice vibrations and excitation induced frequency shifts are discussed.

As a last step one can determine the effectively measured linewidth $\Gamma$ of the transition which reads

$$\frac{1}{\pi T_2} \equiv \Gamma = \frac{1}{2\pi T_1} + \Gamma_{\mathrm{R}} \,. \tag{3.21}$$

$\Gamma_{\mathrm{R}}$ is sometimes referred to as the inhomogeneous contribution to the homogeneous linewidth. It includes the the factors arising due to the fluctuations of $\omega(t)$ which have to be calculated using Eq. (3.15). Theses individual broadening mechanisms do not necessarily lead to an exponential attenuation of the echo intensity, so that expression (3.21) is only a schematic representation of the broadening.

**Steady state linewidths** Assuming all decays to be exponential, Eq. (3.6) can be solved for the ensemble under steady state conditions, i.e. for the case where all time derivatives become zero. The width of the spectral holes, in the case of where the laser linewidth is much narrower than the transition linewidth, then becomes

$$\Delta\nu|_{\mathrm{FWHM}} = \frac{1}{\pi T_2}\left(1 + \sqrt{1 + \chi^2 T_1 T_2}\right), \tag{3.22}$$

a result known in saturation spectroscopy for many years [75]. In deriving Eq. (3.22) it is assumed that the excitation intensity does not change upon propagation through the sample. In an optically thick samples, this assumption is not valid and it can be shown that in the limit of an exponential intensity decay throughout the sample [76]

$$\Delta\nu|_{\mathrm{FWHM}} = \frac{\sqrt{2}}{\pi T_2}\left(1 + \sqrt{1 + \chi^2 T_1 T_2}\right)^{1/2} \,. \tag{3.23}$$

In the small area case, both Eq. (3.22) and Eq. (3.23) are linear in the intensity. Therefore considerable mistakes can be made if parameters such as the Rabi frequency are determined using Eq. (3.22) in the optically thick sample regime.

**Propagation** Up to now it was ignored that the formation of atomic dipole fields in turn modify the exciting laser fields acting on each atom. For optically and spatially thin sample, this change is usually negligible. In such cases the echo intensity is given by Eq. (3.20). However, an exact solution becomes important when trying to calculate pulse propagation through optically thick media. In a polarizable medium the equation of the propagation of the electromagnetic propagation field $\mathbf{E}$ can be written as

$$\left(\frac{\partial^2}{\partial z^2} - \frac{\mathrm{n}^2(\omega)}{c^2}\frac{\partial^2}{\partial t^2}\right)\mathbf{E}(z,t) = \frac{1}{\epsilon_0\, c^2}\frac{\partial^2 \mathbf{P}(z,t)}{\partial t^2}, \tag{3.24}$$

where $\epsilon_0 = 8.854 \times 10^{-12}\mathrm{As/(Vm)}$, $c$ denotes the speed of light, and $\mathrm{n}(\omega)$ is the refractive index at the optical frequency $\omega$. This phenomenon is referred to as self-induced transparency (SIT). A self-consistent solution of this problem was given by McCall and Hahn [77, 78]. However, only for special pulse structures can an analytical solution of Eq. (3.24) and Eq. (3.6) be found. In all other cases the equations need to be solved numerically. SIT has been observed in different gaseous media [78, 79]. Recently, SIT has also been observed for the first time in a RE ion doped crystal [80].

## 3.4 Comments on two level systems

The optical Bloch equations are formally similar to the Bloch equations, used to describe isolated spin 1/2 dynamics in NMR [63,81]. However, NMR transitions occur between states which are energetically relatively near by ( $\Delta\nu(\mathrm{proton}) \leq 10^9$ Hz) whereas in the case of optical transitions, the level spacing is approximately $5 \cdot 10^{14}$ Hz. This has some important consequences. Here, some differences between NMR (liquid or solid) and optical two level systems, with a particular focus on RE ion doped crystals, are presented. It is clear that large deviations already occur when

comparing solid state to liquid NMR. The focus is thus put on the implications connected to the different transition frequencies. The list is not meant to be complete, but is rather limited to some differences the author is aware of.

- **Two level system.** Generally, an optical transition cannot be described by two levels. One therefore needs to adapt the experimental conditions such that the use of a two level system is fairly accurate. In the case of NMR, a two level description is intrinsically fulfilled for an isolated spin 1/2 nucleus.
- **Directional emission.** In optical experiments, the wavelength is small if compared to the sample size. This leads to a directional selectivity in the echo emission [19], which results in propagation effects such as multiple echoes or SIT. In NMR typical transition wavelengths are longer than 30 cm, thus larger than the typical sample size, leading to directionally uniform emission.
- **Thermal equilibrium distribution and relaxation.** Due to the large frequency differences in optical transitions, the occupation probability of the excited state is zero in thermal equilibrium. This is quite different for NMR transitions, where the temperature corresponding to the energy splitting is below 1 Kelvin (22 GHz corresponds approximately to 1 K). Therefore, even at low temperatures the states are equally populated. Application of a strong permanent magnetic field leads to a population difference between states with different Larmor frequencies. Connected to the energy spacings is the fact that the relaxation processes are quite different. In optical spectroscopy, the processes leading to the thermal equilibrium distribution are determined by multi-phonon relaxation as well as spontaneous and stimulated emission. In NMR, Typical spontaneous emission limited lifetimes are in the order of $10^{25}$ s and stimulated emissions range around $10^{10}$ s [63] so that they become negligible. In liquids it is the motional degrees of freedom which allow for a coupling to the lattice. This is known as spin-lattice coupling and can lead to a dephasing of the coherence of a spin system without changing the population of the states (adiabatic contribution), as well as induce transitions, thus altering the population difference which leads to a decrease of the lifetimes (non-adiabatic contribution). For solid state NMR, the situation is similar in the sense that again, it is not the coupling to the radiation field which leads to relaxation to the thermal equilibrium. The exact mechanism which determines the relaxation time is beyond the scope of this summary. It is worth noticing that in the NMR

case, the high temperature condition is usually fulfilled whereas for optical two level systems at cryogenic temperatures the low temperature limit always applies. For a detailed analysis of relaxation in NMR it is referred to Ref. [63].

- **Inhomogeneous frequency distribution.** In frequency selective materials at cryogenic temperatures, the ratio of inhomogeneous to homogeneous linewidth is usually on the order of $10^4 - 10^7$. In liquid NMR the situation is similar if a strongly inhomogeneous permanent magnetic field is applied [72]. However, this is not an intrinsic feature of the material and can be improved so that todays measured linewidths are mostly determined by the homogeneous linewidth. In the case of NMR in solids, the lines are strongly homogeneously broadened, due to dipolar coupling and chemical shift anisotropies. However, using techniques such as magic angle spinning, these contributions can be largely reduced. This implies that in NMR, typical excitation pulses are much shorter than the inverse of the total linewidth of the transition. To accomplish this in a RE ion doped crystal transition with a typical oscillator strengths of $f = 5 \cdot 10^{-8}$, pulses of 100 ps with pulse intensities of about 100 MW/cm$^2$ would be needed. This value is far above anything applicable. Therefore in RE experiments the inhomogeneous width $\sigma_\nu$ is always much bigger than the Rabi frequency $\chi$. This has an impact on the shape and length of the echo as pointed out earlier.
- **Spectral resolution.** In NMR, for slow passage as well as Fourier transform techniques, the spectral resolution is given by the homogeneity of the static field and the accuracy of the rf-generator. In optical experiments, echo measurements allow for the determination of linewidths in the sub-kHz regime. Using a slow passage method, this resolution is much more difficult to be achieved, since it requires the stabilization of the laser source up to these frequencies. Hole burning spectra in the sub 10 kHz have been obtained during this work (compare Chapter 5) and currently improvements of laser sources are in progress. However the task of sub-kHz laser linewidths, corresponding to Q-factors of about $10^{13}$ is a big technical challenge.

# 4. Experimental and instrumentation

The experimental framework is introduced. The focus is put on the laser, in particular the active stabilization of a dye laser. The main advantages of side band modulation techniques for active frequency stabilization are described and the different terms contributing to the error signal are presented. Finally the design of the locking cavity, the cryostat and the automation are depicted.

## 4.1 The light sources

In order to be able to spectroscopically investigate $Pr^{3+}$ and $Eu^{3+}$ doped crystals at the level of the homogeneous linewidth, several characteristics for the light source are required, which can be summed up as follows:

- a scan range characterized by the investigated spectral feature. If experiments are carried out within one inhomogeneous band, a few GHz are usually enough. If different $J$-levels need to be resolved, several hundreds of $cm^{-1}$ must be scanned. In this case however, a narrow laser linewidth is not required.
- a laser emission in the visible red (the transitions studied here absorb in the wavelength range from 580-630 nm).
- a spectral purity given by the homogeneous linewidth, ranging from 100 Hz up to a several MHz.

Up to now, the only systems which were able to achieve such a performance were dye lasers. Today and in the near future this will change towards laser diodes or optically pumped oscillators (OPO) which appear to be very promising [82]. This will have the advantages of much lower costs and easier operation.

During this work two different dye lasers were used. Both systems are constructed following the scheme illustrated in Fig. (4.1). An argon ion laser (Spectra physics 2400), operated in either single- or multi-line mode with a maximal output power of 20 W (multi-line) is used to pump the ring dye laser. The dye laser consists of different elements which allow for a decrease of the broad band laser oscillation to a linewidth of approximately 1-2 MHz. The laser emission is given by $c/2l$, where $l$ denotes the effective length of the dye laser cavity. With $l = 0.8$ m this results in a mode spacing of approximately 180 MHz. Bidirectional lasing is suppressed using a Faraday rotator (optical diode). From the wide range of possible modes single mode performance needs to be achieved. This is done using a birefringent filter (BRF), and thick and thin ethalons. The combination of a thick and thin ethalon is usually called an intra cavity assembly (ICA). The transmission characteristics of the different elements are sketched in Fig. (4.2). A rough frequency selection is

obtained using the BRF which has a passive transmission range on the order of 380 GHz. The thin ethalon with a free spectral range (FSR) of 200 GHz further limits the number of modes. The thick ethalon, with a FSR of 10 GHz finally reduces the number of cavity modes to about 30. Mode competition leads to single-mode

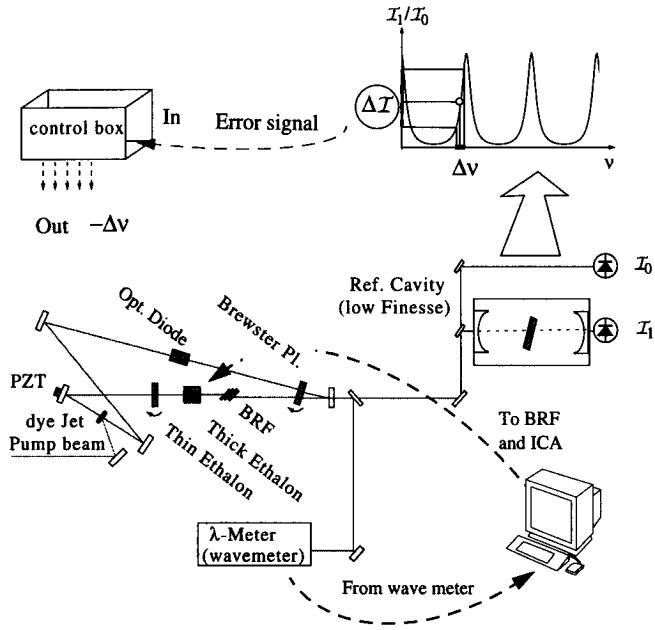


**Figure 4.1:** Illustration of a commercially available laser source. The dye laser is pumped by an argon ion laser. The elements in the cavity- the birefringent filter (BRF), thick and thin ethalon- reduce the number of modes as shown in detail in Fig. (4.2). The output is monitored on a wave meter for an absolute frequency determination. Frequency stability is obtained using fringe locking, by measuring the intensity $\mathcal{I}_1$ through a low finesse invar cavity. To avoid that intensity fluctuations lead to frequency excursions the signal is normalized by a reference signal $\mathcal{I}_0$. The error signal is given on the piezo transducer in the cavity. In the 899 version the frequency position can be automatically varied over the full range of the dye. The signal from the wave meter is given to the computer from where the ICA and the Brewster window are automatically controlled.

lasing. Laser operation under such conditions is usually called "free-running". Fluctuations in the cavity can cause instabilities of the mode position, yielding short term (milliseconds) stabilities of the order 1 MHz and frequency excursions in the 10 MHz range on the second time scale. To suppress these long term fluctuations

fringe locking is performed. This is done by monitoring the transmitted intensity through a low finesse invar cavity which is temperature stabilized. Frequency fluctuations will therefore lead to a change in the transmission intensity. The error signal, proportional to the intensity change, is applied to the piezo transducer (PZT) in the laser cavity. To avoid that intensity instabilities are transformed into frequency fluctuations the signal is normalized by a reference signal recorded on a second photo diode. In this way a laser performance in the range of 1 MHz rms in the seconds time range is obtained. Tuning of the laser frequency can then be performed using the Brewster window with a maximally accessible frequency range of 30 GHz. The two laser systems used during this work are shortly described below.

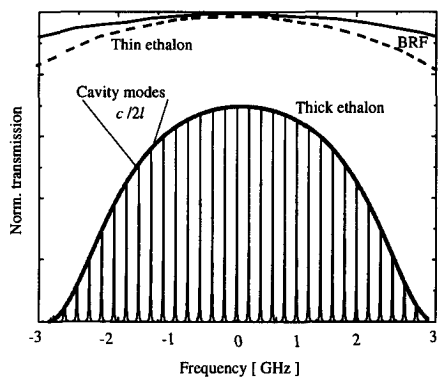


**Figure 4.2:** Due to the length of the cavity, modes with a FSR of 180 MHz are formed. The number of modes is first reduced using a birefringent filter acting as a bandpass with a bandwidth of 380 GHz. The linewidth is further reduced by a low finesse thin ethalon (FSR of 200 GHz) and a low finesse thick ethalon with a FSR of 10 GHz, respectively. Mode competition leads to single-mode laser performance. A dye laser operating in such a way is called free-running.

**899-Autoscan.** The commercially available 899-autoscan dye laser corresponds to the system sketched in Fig. (4.1) The BRF, PZT, ICA, and Brewster plate are computer controlled. Additionally a wave meter yields the absolute laser frequency with an absolute precision of 200 MHz and a reproducibility of 50MHz. The possibility of long scan ranges becomes crucial for storage application in data storage experiments, especially when using dye doped polymers.

**Coherent-699.** The 699-21 laser corresponds to the 899 system without the computer part. Scanning can be performed over 30 GHz using the Brewster window.

For large movements, the laser needs to be controlled manually. Since the inhomogeneous linewidth of RE ion doped crystals is usually below 30 GHz, the available scan range is broad enough. On the other hand the narrow homogeneous linewidth of the transitions makes a narrower laser linewidth desirable. This requires better locking. Therefore the commercially available system was modified. This will be the topic of the next Section.

## 4.2 Laser stabilization

In the previous Section fringe locking was presented as a method to further suppress frequency fluctuations. The laser performance can in principle be further improved, using either a high finesse cavity or enhanced temperature control. Still, if laser performance in the sub-MHz regime is desired, fringe locking is not well suited. Most crucial is that fact that if the finesse is very high, the locking range becomes small. Additionally, laser medium fluctuations will produce changes in the laser spot size and thus influence the mode matched cavity transmission. Another problem can arise due to the fact that normalization of the intensity is needed, since otherwise intensity fluctuations are transformed to frequency excursions. This however requires properly matched photo diodes. To avoid all these problems Drever et al. [83] proposed a different way to perform locking to the cavity, namely using a side-band modulation. A similar technique - the "Pound stabilizer"- had been known in the microwave field for many years [84]. The method is therefore commonly referred to as Pound Drever locking or frequency modulation. In Section 4.2.1 Pound Drever locking is reviewed. A crucial problem of any locking device is the performance of the absolute frequency marker, i.e. the reference cavity. In Section 4.2.2 a home built reference cavity design is presented.

### 4.2.1 Pound Drever stabilization

Ideally, a locking signal has a a zero transition at the locking point, a steep error curve, and a large locking range. As will be shown below, these criteria can all be matched using rf-side-band modulation of the optical signal. This type of locking is often referred to as Pound Drever locking and has been theoretically described in great detail [83,85]. In what follows, the main ideas are summarized. Simultaneously to Drever et al., Bjorklund et al. introduced side band modulation in spectroscopy and referred to it as FM spectroscopy [86].

As depicted in Fig. (4.3), frequency modulation techniques can be separated into three stages, which will now be shortly reviewed for the experimental configuration chosen in this work.

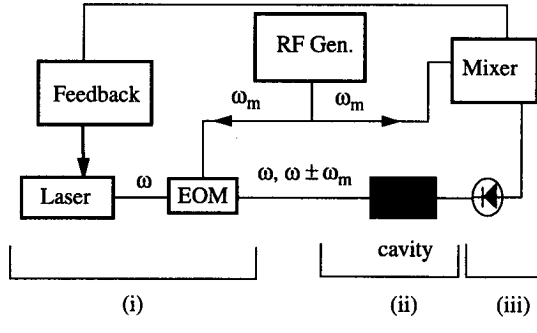


**Figure 4.3:** Pound Drever locking scheme. The three marked regions are described in the text for the case of a reference cavity used in reflection geometry, as done in the present work.

(i) In the first stage, the laser beam of frequency $\omega$ is passed through an electro optic phase modulator, run at a modulation frequency $\omega_m$, and an amplitude $\delta$.[1] The laser field $E$, emerging from the electro optic modulator (EOM) can then be

[1] Alternatively the laser cavity can be directly modulated which also leads to side bands [87].

written as

$$E = E_0 \exp\left[i(\omega t + \delta \sin(\omega_m t))\right] \ . \tag{4.1}$$

For simplicity vectorial notation is omitted here. In the case of small modulation amplitudes, i.e. $\delta \ll 1$ Eq. (4.1) reduces to

$$E = E_0 \left[J_0 \exp(i\omega t) + J_1(\delta) \exp[i(\omega + \omega_m)t] + J_{-1}(\delta) \exp[i(\omega - \omega_m)t]\right] \ , \tag{4.2}$$

where $J_i$ denotes the Bessel function of $i$th order.

(ii) In a second step the cavity is probed. In the work presented here, a setup with the cavity in reflection geometry was chosen, the reason being that previous workers reported problems with mode profile asymmetries when using the transmission modes [83]. The formal description is based on the one presented by Houssin et al. [85]. The width of the cavity fringe was chosen to be much narrower than the spectral separation between the side bands and the center frequency. In this case, the total reflected laser amplitude becomes

$$E_r = E_0 \sum_{k=-1,0,1} J_k(\delta) R(\omega_k) \exp(-i\omega_k t), \tag{4.3}$$

where

$$R(\omega_k) = E_0 \left[r_1 - r_2 t_1^2 \frac{\exp(-i(\omega_k)\tau)}{1 - r_1 r_2 \exp(-i(\omega_k)\tau)}\right] \ , \quad \text{and} \quad \omega_k = \omega + k\omega_m. \tag{4.4}$$

Here, $\tau$ denotes the round trip time in the cavity, and $r_i(t_i)$ are the $i$th mirror reflection (transmission) coefficients. In the case of more or less matching center and cavity frequencies, the center frequency's direct reflectance, corresponding to the first term between the brackets in Eq. (4.4), is phase locked to the (almost) totally reflected side bands. As Drever et al. pointed out, another contribution arises through the "leakage back field" of the cavity, corresponding to the second term in the parenthesis of Eq. (4.4). Very fast phase fluctuations, i.e. fluctuations faster than the cavity field storage time $\tau_c$, ($2\tau_c$ = number of reflections $\times\tau$) are not followed by the leakage field and a field with a phase averaged over $\tau_c$ will be

superimposed to the direct reflection. Thus, even though the "response" time of the cavity is slow, the technique allows for the elimination of fast phase (frequency) fluctuations. In the case of slow variations, the leakage field follows the direct reflection.

(iii) Finally, in the last step the signal is demodulated using a matched rf-frequency with an adjustable delay. The signal intensity $\mathcal{I}$ is recorded by a photo diode, $\mathcal{I} \propto E_r E_r^*$. The recorded intensity is mixed with $\sin(\omega_m t)$ yielding a continuous component, which corresponds to the error signal $S$, that can be written as [85]

$$S \propto \mathcal{I} t_1^2 \left[ \frac{\sin(\omega\tau)}{D} - \frac{\sin(\omega+\omega_m)\tau}{D^+} - \frac{\sin(\omega-\omega_m)\tau}{D^-} \right] \tag{4.5}$$

with

$$D = 1 + r_1^2 r_2^2 - 2 r_1 r_2 \cos(\omega\tau), D^\pm = 1 + r_1^2 r_2^2 - 2 r_1 r_2 \cos((\omega \pm \omega_m)\tau) \ .$$

Here, only the difference frequency term is considered. In principle, when mixing is performed a sum and difference frequency are generated. However, the sum frequency is larger than the bandwidth of the electronics and can therefore be neglected. An error signal as it described by Eq. (4.5) is shown in the inset of Fig. (4.4). The slope at the center is given by the cavity width and defines the magnitude of the feedback signal. Further, a large locking range is achieved, since the polarity of the signal does not change in a range given by the spectral distance to the side bands. The setup used to perform frequency stabilized experiments is presented in Fig. (4.4). In front of the dye laser an optical diode is placed in order to avoid back reflections. 10% of the laser beam are split off and modulated by an electro-optic phase modulator ( Fastpulse Technology 1039-UNC), which generates side bands at $\pm 8$ MHz. The phase modulated horizontally polarized beam is passed through a polarizing beam splitter leading to an amplitude modulation. Linear to circular polarization conversion is performed using a $\lambda/4$ plate. The laser beam is imaged into the laser cavity under mode matching conditions. The back reflected signal is converted to vertical polarization and detected on a fast PIN diode (New Focus 1601,

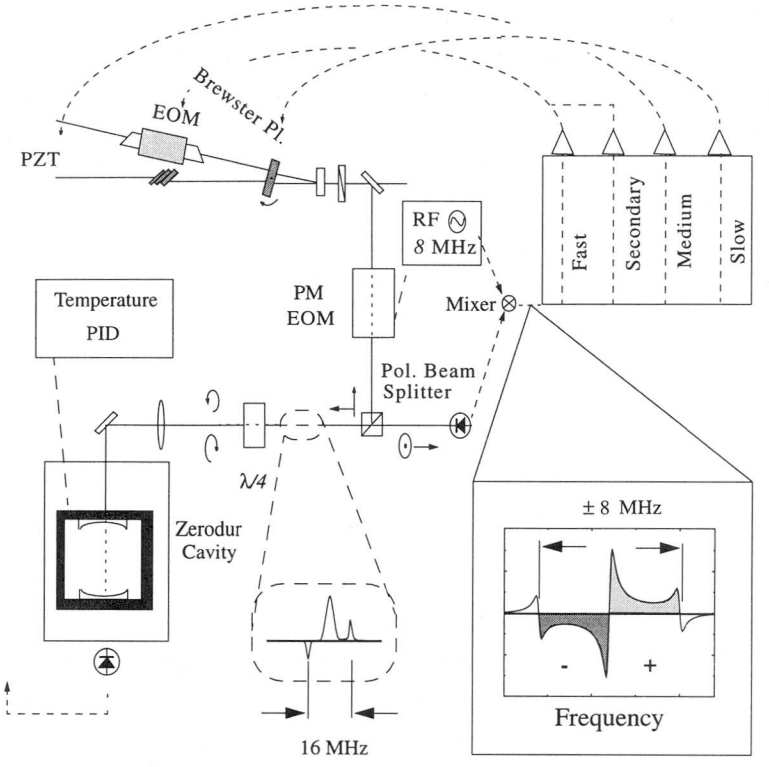


**Figure 4.4:** Overview of the setup of the actively stabilized dye laser using Pound Drever stabilization. After an optical isolator at the output of the laser, 10% of the beam is passed through an electro-optic modulator and phase modulated with 8 MHz. The horizontally polarized beam is passed through a $\lambda/4$ plate, yielding circular polarization. The temperature stabilized cavity, sitting in vacuum is described in detail in Section 4.2.2. The polarization of the back reflection is converted to vertical polarization and is applied to a fast photo diode. The resulting side-band modulation is shown in the inset. Heterodyning with a matched 8 MHz reference results in a sum and a difference signal for which the difference signal is shown (compare Eq. (4.5)). The sum signal with a carrier frequency of 16 MHz is out of the range of all amplifiers and can therefore be neglected. Note explicitly the broad locking range (no change of the sign of the error signal) which is purely determined by the applied rf-frequency. For the error feed-back the different amplification stages are separated. Fast amplification (< 4 MHz ) and secondary amplification (<90 kHz) are applied to the intra-cavity electro-optic modulator. The medium amplifier (bandpass 20 Hz - 50 kHz) controls the piezo-mirror and slow drifts (DC-200 Hz) are corrected with the Brewster plate.

band width 1GHz). The signal is then amplified by a fixed gain 30 dB amplifier (Mini-Circuits MAR-8). The electronic PI (P: Proportional, I: Integral) controller was constructed at the Australian National University. It consists of six different elements which are now shortly described. (i) A 8 MHz oscillator. To provide enough reference signal a fixed gain power amplifier (29 dB, 1 W out) is used. Its output power is given on a resonant transformer terminator to increase the 20 $V_{pp}$ 8 MHz signal up to 80 $V_{pp}$. Part of the rf-signal is split off and used for demodulation with an adjustable delay. (ii) A mixer which demodulates the reflection signal and controls the offset. (iii) A fast amplifier (<4 MHz, P) and (iv) a secondary amplifier (<90 kHz, P) connected to the bipolar intra-cavity EOM. (v) A medium bandpass amplifier connected to the piezo-mirror (20 Hz-50 kHz, PI) and (vi) a slow amplifier (DC-200 Hz) controlling the Brewster plate. Further details can be found in the user manual [88].

### 4.2.2 The reference cavity

In order to achieve a good laser performance, in addition to a good locking scheme a stable reference is needed to which the laser can be locked. The quest for oscillators of increasing accuracy and stability has been one of the most continuing developments in physics over hundreds of years, leading from early clocks to todays cold atom and trapped ion clocks. Ultra-stable resonators are essential tools in different branches of physics serving for measurements of pulsar timing, tests of relativistic theories [89], the detection of gravitational waves [90], or the use for ultra high resolution spectroscopy of ions in traps [91] or solids [92]. It is thus not surprising that much effort has gone into the development of better resonators.

The requirements on the acoustic stability and thermal expansion properties of a reference cavity are quite severe if used for laser stabilization. To better visualize this one can estimate the maximally allowed length change of a cavity which has an absolute frequency precision of 1 kHz. Considering a cavity of length 463 mm (parameter used in this work) and keeping in mind that $d\nu/\nu = dl/l$, one finds that a variation in length of $\sim 10^{-12}$ m leads to a 1 kHz frequency change. Here, for simplicity a constant refractive index was assumed. This implies that the requirements

on the stability, intrinsically coupled to those of the material and the surrounding are very strict.

In earlier locking experiments, a commercially available reference cavity was used (Newport SR 130 super cavity) [53]. The strong cavity drift of approximately 1 MHz/min made ultra-high resolution experiments difficult, mainly due to the long term performance. The drift was partly caused by temperature fluctuations. Most strongly, frequency creeping was observed due to the hysteresis of the cavity PZT onto which the mirrors were mounted. In order to overcome those problems, a new cavity was designed with the following requirements in mind: (i) a narrow linewidth, (ii) a FSR not smaller than 16 MHz, corresponding to double the width of the applied side band modulation but not broader than 500 MHz. The second restriction is given by the spectroscopic requirement to have a large number of cavity modes per inhomogeneous band. As a last point, (iii) the wish to obtain long term stability.

The cavity sketched in Fig. (4.5) is a good solution for the listed requirements. The construction was inspired by a similar design reported by Salomon et al. [93].

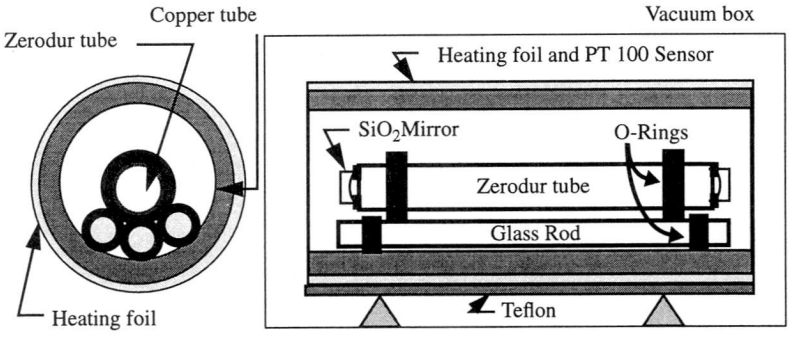


**Figure 4.5:** Design of the reference cavity. The quartz mirrors were glued to the ends of the zerodur cavity. The cavity was embedded in a copper tube to guarantee good thermal contact. A temperature stabilized thermal foil surrounded the cooper tube. The whole system was placed in a vacuum tube.

The cavity length $l$ was chosen as $l = 463$ mm and used in a confocal configuration. For a confocal setup, FSR=$c/4l = 160$ MHz, a value far below the typical inhomogeneous linewidth of a RE ion doped crystal. The mirror reflectivity was approximately 99.7% which resulted in an approximate finesse F of 1000. The finesse is given by F= $\pi\sqrt{R}/(1-R)$, where $R$ denotes the mirror reflectivity.

In order to achieve the required performance, the following measures were taken in the design of the cavity:

- A zerodur cavity with a low thermal coefficient was used. A comparison of thermal parameters of typical resonator materials is presented in Table 4.1.
- The quartz mirrors were glued sidewise to the cavity (no epoxy between the cavity and the mirror). Optical contact would be ideal with mirror coatings onto the same material as the one used for the cavity.
- No PZT was employed. Locking to the fixed frequency of the the cavity was performed by scanning the laser. Once locked, the frequency could be changed using acousto-optic modulators. Thus, piezo creeping was avoided.
- Temperature stabilization was performed in the 15 mK regime. From the thermal expansion coefficient of zerodur a long term stability of 250 kHz was expected. Long term temperature fluctuations were damped by surrounding the zerodur tube with a massive copper rod. Attached to the copper tube was a heating foil, covering the entire copper surface. The foil was in turn temperature stabilized using a Lakeshore 330 PID-temperature controller. This design was expected to be rather insensitive to temperature changes since no direct thermal contact between the copper tube and the zerodur cavity was established.
- The cavity was placed in the vacuum. This yielded better thermal isolation from the environment.
- To acoustically isolate the cavity, the zerodur tube was placed on O-rings which were in contact with three glass rods which in turn where decoupled from the copper tube, using a second set of O-rings. This additionally guaranteed that the distortion or friction of the copper given by thermal expansion would not destroy the thermal coefficient of the cavity. The entire cavity was placed on a metal board which was acoustically isolated from the optical table using a

rubber layer. The rubber layer was chosen such that the vibrations, deriving from fluctuations of the the Argon ion laser cooling water were strongly damped. The board was placed on the optical table without fixed contacts in order to minimize the transport of vibrations.

| Material | Therm. exp. coeff. $\kappa[K^{-1}]$ | Spec. heat $c_p[J/(gK)]$ | Therm. cond. $\lambda[W/(mK)]$ |
|---|---|---|---|
| Sapphire | $5{\cdot}10^{-12}$ $K^{-1}$ | 0.8 | |
| Zerodur | $5{\cdot}10^{-8}$ $K^{-1}$ | 0.8 | |
| Copper | $5{\cdot}10^{-6}$ $K^{-1}$ | 0.4 | 390 |
| Invar | $2{\cdot}10^{-6}$ $K^{-1}$ | | |
| Quartz | $5{\cdot}10^{-7}$ $K^{-1}$ | | |
| Epoxy | $6{\cdot}10^{-5}$ $K^{-1}$ | | |

**Table 4.1:** Thermal expansion coefficient, specific heat, and thermal conductivity, for different materials commonly used in cavity design. The value given for Sapphire was measured at 1.9 K and corresponds to the lowest thermal expansion coefficient obtained up to date [87].

The linewidth of a single transmission fringe is equal to the ratio FSR/F, thus an approximate cavity linewidth of 160 kHz is expected. In Fig. (4.6), a frequency scan over the experimentally observed error signal is presented.

The signal was measured using the commercially locked laser with a linewidth of approximately 1-2 MHz, indicating that the cavity linewidth is better than 1 MHz since a resolution given purely by the laser linewidth is observed. However, a precise determination of F requires a laser with a much narrower spectral linewidth than the one given by the cavity, since the total transmission is given by a convolution of the cavity width with the laser linewidth.

In the insets a locking error signal and the corresponding histogram are shown. If the finesse of the cavity is known, the laser linewidth can in principle be estimated from the combination of the error signal histogram and the ideal peak to peak transmission. This method is indirect and the knowledge of different parameters

which can vary over time is needed. In the next Chapter it is shown that PSHB offers a much more direct and elegant way to estimate the stability of a laser. This method will be used to verify the performance of the laser/cavity system.

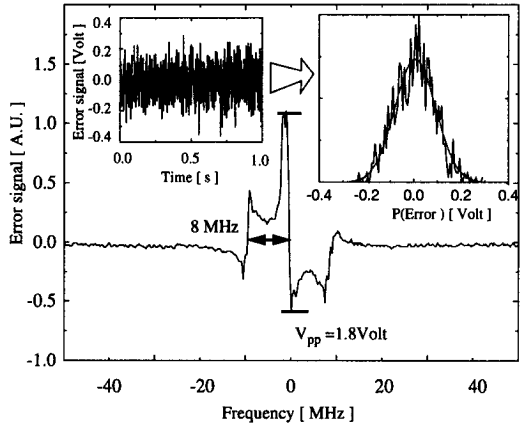


**Figure 4.6:** Error signal of the reference cavity. Shown are a frequency scan over a single transmission fringe. In the insets an error signal is shown for a locked laser, along with a histogram of the spectral error distribution. Knowing the ideal peak-peak transmission (for the 1 MHz laser line/cavity transmission, 1.8 V peak-peak transmission is observed) and the finesse of the cavity (approximately 1000), the error histogram yields the spectral purity of the laser. From this rough values the laser linewidth is estimated to approximately 20 kHz. In the next Chapter it is shown that the obtained laser linewidths were narrower by a factor two to four.

## 4.3 The cryostat

All experiments described in this work were carried out in the cryostat shown in Fig. (4.7) and denoted as "Sputnik" from here on. It can be used in gas as well as fluid mode, allowing a variation of the temperature. Here, it was operated in the immersion mode at temperatures below the $\lambda$-point (2.17 K). Thus, bubble formation which makes holographic detection impossible was avoided. The temperature range around 1.7 K was reached by contemporally pumping on the reservoir and the sample chamber. Operated in this way, experiments with durations of up to 15 hours could be performed.

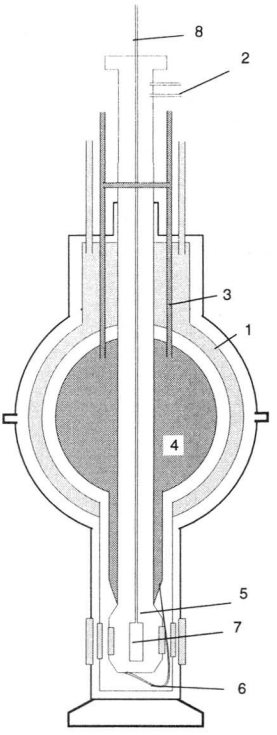


**Figure 4.7:** Design of the immersion cryostat "Sputnik". (Figure adapted from Ref. [94]).
Typical filling parameters corresponded to 5l liquid nitrogen and 3l liquid helium. At 1.7 K this yields experimental times up to 15 hours.

(1) Isolation vacuum pumped down to $10^{-4}$ Torr.
(2) Connection to the pump. Also hooked up to the reservoir (not shown).
(3) Nitrogen tank.
(4) Helium reservoir.
(5) Sample chamber.
(6) Needle valve connecting the reservoir with the sample chamber.
(7) Sample.
(8) Sample holder.

## 4.4 Automation

The software partly developed during this work is comparable to a commercially available package like *Lab-windows*. The concept consisted in the development of a high level language which allows the user to quickly adapt the system, without the need of the knowledge of low level code or specific device programming. The architecture is built on strictly separated devices, device communication and an easy to use user interface. The structure and interfaces of such a system are shown in Fig. (4.8) and described below.

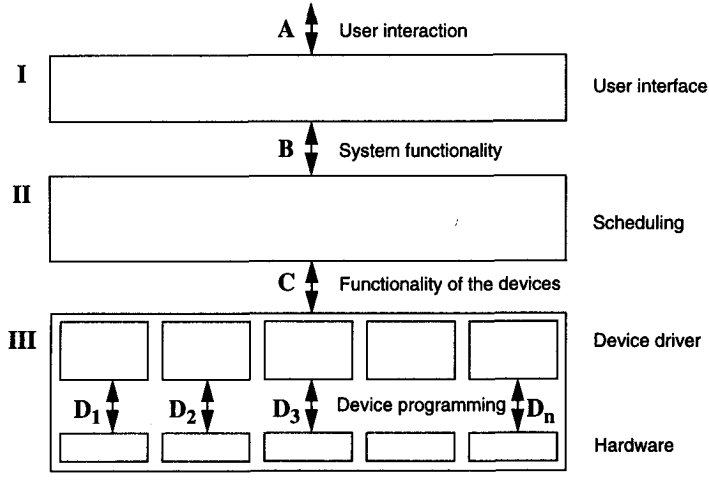


**Figure 4.8:** Structure of the experimental automation program. Adapted from Ref. [95].

### Structure

I *User interface.* Can in principle be either graphical or shell oriented. Here a shell oriented environment was chosen.

II *Scheduling.* Connection and communication between the different devices. Ideally, some high level interface which does not require any detailed knowledge about the device, and just contains sets of parameters, possible actions and the devices' status.

III *Device drivers.* Hardware specific programming (for example GPIB) of the device functionality.

### Interfaces

A *User interaction.* Can in principle be freely chosen.

B *System functionality.* Can be regarded as a requirement list of the performance of the system. The implementation itself is hidden. Example:*"describe device mode".*

C *Device functionality.* This depends on the the implementation of layer II. Programming of the device needs to be integrable into the high level language used there. Here, a C-syntax was used with some restrictions on the form given by layer II.

D *Programming of individual devices.* In a Unix environment most commonly done in C, since a large number of libraries can be used. Programming within this interface depends strongly on the specific device, defined by the product producer.

The experimental procedure is serial and communication between different devices is performed through input and output lines and globally accessible variables. Due to the separation into different levels and strictly separated devices, introduction of new devices is easily performed. The backbone of this program was written by Werner Graff and adapted or extended to personal needs. All experiments described in this work were carried out with this package.

Leer - Vide - Empty

# 5. High resolution cw-spectroscopy

Measurements of persistent spectral hole burning (PSHB) are presented, demonstrating the potential of hole burning for the verification of the short and long term performance of the laser system. Characteristic parameters such as the Allan variance or the effective thermal expansion coefficient of the reference cavity are determined for different configurations. It is shown that with the laser/cavity system presented in Chapter 4, a laser linewidth of better than 5 kHz on the time scale of minutes can now be obtained. The increased frequency resolution is exploited to measure the hyperfine splittings of $Pr^{3+}$ in $Y_2SiO_5$ and the results are compared to other techniques. Finally, some light is shed on the previously addressed issue of assymetric side- and anti-holes in $Pr^{3+}$ in $Y_2SiO_5$.

## 5.1 Introduction

Frequency stabilization of laser sources is an interesting and very current problem in fundamental sciences. The application of very stable laser sources is proposed to be in different areas. Ultra-high resolution spectroscopy is in this sense only one of the potential fields in which stable laser sources can be employed. A major problem consists of the determination of the absolute laser performance, i.e. the verification of its linewidth and its temporal stability. As shown in the last Chapter, the laser linewidth can in principle be measured using the error signal of the Pound Drever locking. However, this requires the knowledge of different experimental parameters and therefore only indirectly reflects the effective laser linewidth. A technique often used makes use of the observation of a beat signal between two laser sources. This requires two separate and stable lasers and additionally does not permit an absolute frequency determination since simultaneous drifts of the lasers will not affect the beating signal. Spectroscopic transitions can also be used to monitor the laser performance. If laser linewidths in the range of MHz need to be controlled, saturation cells can be used. However, the transition linewidths are at best a few MHz, so that laser fluctuations in the kHz or even Hz regime can not be monitored. Finally, atoms can be cooled in a magneto-optical trap and transition linewidths in the sub-Hz range can be achieved [96]. However, the technique is rather complex.

The simplicity and high spectral resolution of persistent spectral hole burning (PSHB) make it a very powerful alternative. It is clear that a spectral hole burning material which shows high spectral resolution can be used for the characterization of the laser, since the hole burning pattern directly reflects the laser profile. Once a spectral hole is formed it acts as a stable frequency marker. Of course, there are several requirements on the hole burning system which need to be met such that it can be used as a "pseudo-absolute" frequency marker. The three main points are:

(i) a narrow linewidth,

(ii) long persistence of the spectral hole, and

(iii) little or no spectral diffusion (hole broadening).

Each of these points can be discussed separately. Point (iii) will be studied in great

detail in Chapter 7. The persistence of the hole and the small spectral diffusion are somewhat related to each other, since a very long persistence implies that little configurational changes occur which generally lead to broadening and a decreasing signal-to-noise ratio (SNR). The contrary is not true. Even if a system shows no spectral dynamics, the hole lifetime can be rather short, since it may be determined by the barrier of the back reaction. For the experiments presented here, $Eu^{3+}$ in $Y_2SiO_5$ in the optical site II was chosen [92]. This system appeared ideal, since at temperatures below 2 K, almost lifetime limited spectral holes have been observed [21]. Results of the long term behavior are presented in Section 5.2.

It is clear that the tasks for high resolution cw-spectroscopy and for good laser performance go hand in hand. Once the spectral purity is achieved, such a laser offers a broad variety of interesting applications. Possible advantages of a ultra high resolution cw-lasers in RE ion doped crystal spectroscopy are, the high spectral power, the increased spectral resolution, important in frequency domain measurements, and for time-frequency domain hybrid memories [97] and, the increased coherence time (important in time resolved studies). In Section 5.3 results are presented where the improved laser resolution allowed for the determination of hyperfine splittings with a resolution usually obtainable only using double resonance techniques.

## 5.2 Use of PSHB for laser stabilization

The experiments presented in this Section were carried out in a 0.1 at.% $Eu^{3+}$:$Y_2SiO_5$ sample. High resolution spectroscopy of $Eu^{3+}$ in $Y_2SiO_5$ was first performed by Yano et al. [92], observing linewidths of several 100 Hz at temperatures of 6 K. Since then, the investigation of this system has been driven by potential applications as storage devices or as a material which could be used as a high resolution frequency marker. Applying a small magnetic field (100 G) and performing the experiment at 1.5 K, Equall et al. were able to measure homogeneous linewidths below 100 Hz [21]. Up to now this corresponds to the longest dephasing time ever observed in solids. It thus seems clear that the requirement for narrow spectral holes is nicely fulfilled. The cited works had been

carried out using photon echo techniques, thus investigating the time scale of $\mu$s up to ms. It was therefore not clear how good the material may serve for long term investigations. Yano et al. [92] commented that no spectral diffusion was apparent on the minute time scale. However, their investigations were performed with a 1 MHz laser, corresponding to seven orders of difference if compared to the lifetime limited linewidth. Here, with kHz resolution the hole stability and dynamics on time scales from a few milliseconds up to hours are investigated.

### 5.2.1 Experimental setup

The setup used for the experiments described in this Chapter is shown in Fig. (5.1). The equipment is arranged for standard holographic measurements. The argon ion laser (Spectra Physics 2040, 7W multi line) pumped 699 dye laser was actively locked to the home built cavity. Details about the locking and the cavity can be found in the preceding Chapter. Once locking was achieved the laser position was fixed. Scanning of the laser frequency was performed using a set of tandem 200 MHz acousto-optic modulators (AOM, Matsushita EFLM 200), both positioned in the focal plane of lenses of focal lengths of approximately 100 mm. This guaranteed that no positional shift was present upon changing the frequency. Another lens was used after the AOMs to re-collimate the beam. The two AOMs were driven by a single rf-frequency generator (Adret Schlumberger 740 A), whose output was enhanced by a 33 dB fixed gain amplifier (Kalmus 700 LC). The frequency precision of the rf-source is specified to 10 Hz. The rf-power could be adjusted to a maximum of 1 Watt. The frequency was split using an power splitter (Mini Circuits 15542), thus yielding a maximal power of 0.5 W on both AOMs from one and the same source. The full scan range was given by twice a single AOMs scan bandwidth, which for a 200 MHz AOM (center frequency) corresponds to approximately 80 - 120 MHz. The exact value depends on the intensity profile needed. Up to 80 MHz the diffraction intensity changes by less that 10 %. By adapting the driving power of the rf-generator, the power of the write and read beams could be adjusted. With the beam splitter the reference and object beams were generated which could be blocked using shutters in the corresponding arms. The linearly aligned laser polarization was adjusted for

for maximal absorption and the sample was placed in the Sputnik cryostat and kept at 1.7 K. The signals were detected by photo multiplier tubes (Hamamatsu

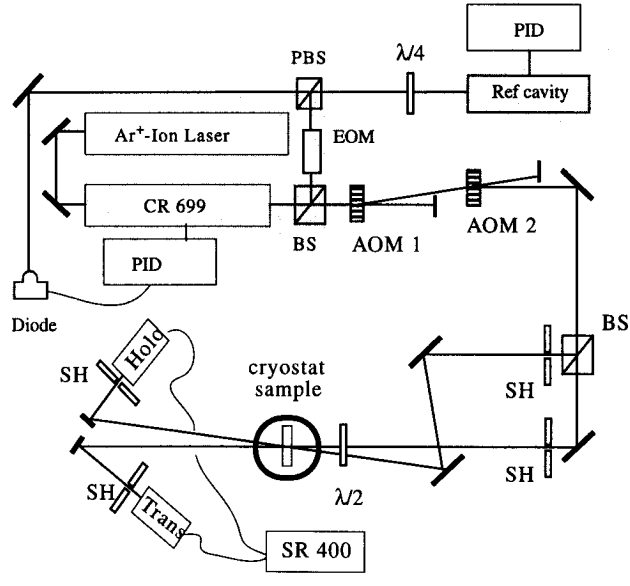


**Figure 5.1:** Experimental setup for a holographic measurement using the actively stabilized laser source. Details about the shaded regime can be found in Fig. (4.4). Scanning and amplitude control was performed using acousto optic modulators (AOM 1 and 2). The frequency precision is given by the rf-source which is specified to 10 Hz. The beam was passed through a beam splitter (BS). Using a $\lambda/2$ plate the polarization could be adjusted to the transition dipole moment of the probed ion species. The beams were controlled using shutters (SH). The signal was detected using photo multiplier tubes (Hamamatsu 928), using them either in single photon counting mode in combination with a SR 400 or by monitoring the amplified signal with an oscilloscope (Lecroy LC 7200). The experiment was fully computer controlled through GPIB interfaces using the software presented in the preceding Chapter.

928) and recorded using a Stanford SR 400 (gateable 200 MHz two channel binary counter with included pre-amplifier and discriminator) with variable gate times. Alternatively the amplified signal could be given onto a digital oscilloscope (LC 7200). The entire experiment was computer controlled through IEEE interfaces using the software described earlier.

### 5.2.2 Hole stability

#### Long term stability

The hole stability defines the maximal time for which PSHB can be continuously used as a frequency marker or tester. To determine this time window, the hole decay was monitored. Holographic detection was used. Due to the better SNR the laser power could be reduced by 5 orders of magnitude upon readout, thus permitting the treatment of the probing as interaction free. This was verified experimentally. Up to first order the diffraction efficiency $\eta$ at the center of a non-saturated spectral hologram can be written as [98,99]

$$\eta = \left(\frac{\alpha_1(\omega)}{2\cos\theta}\right)^2 \exp\left(-\frac{\alpha_0(\omega)d_s}{\cos\theta}\right) . \tag{5.1}$$

Here, the $\alpha_i$ denote the $i$th order of the absorption grating, whilst $d_s$ is the sample thickness and $2\theta$ the angle between the two burn beams. Since spectral hole gratings are always concentration gratings they also contain dispersive contributions. However, if the phase is kept constant, the center of a spectral hole will be purely characterized by the absorption modulation [100]. For shallow holes, the exponential term becomes almost constant and can be neglected. Therefore, the absorption hole decay is proportional to the square root of the diffraction efficiency. The effect of hologram decay is shown in Fig. (5.2).

Since not the broadening but rather the peak decay were of interest here, commercial locking was used. The observed decay is strongly non-exponential. Varying barriers for the the different hyperfine back reaction rates may be one of the reasons for such a behavior. In $Pr^{3+}$ in $Y_2SiO_5$ Holliday et al. [51] also observed non-exponential hole decays, which were invariant upon resonant pumping of the hyperfine levels. They concluded that varying hyperfine level lifetimes could not be the reason for the non-exponentiality and speculated whether ion-ion coupling may be the cause. However, no further evidence for this assumption was given. Here, a detailed investigation of the functional dependence of the decay form is omitted, since the focus lies on the absolute maximal decay time rather than its origin. From Fig. (5.2) it can be observed that the effective decay time of the absorption hole is

longer than ten hours, considering that the decay exhibits a stretched exponential behavior. It can therefore be concluded that concerning property (ii), i.e. the long term stability, $Eu^{3+}$ in $Y_2SiO_5$ is an excellent candidate for the investigation of long term frequency trajectory studies.

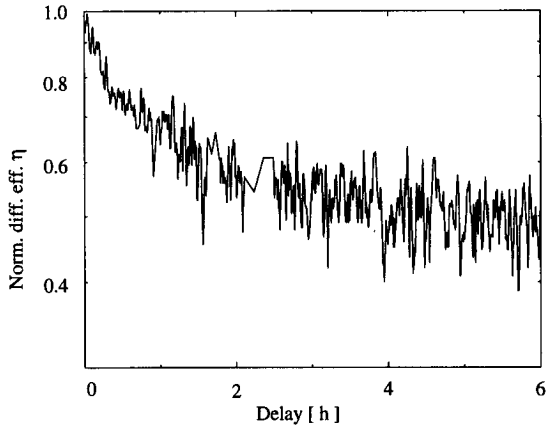


**Figure 5.2:** Decay of a persistent hologram burned in the 580.049 nm transition of $Eu^{3+}$ in $Y_2SiO_5$. Shown is the decay of the intensity on a log scale at the burn position. The spectral hologram was burned using a 1 MHz linewidth. For the readout the power was attenuated by 5 orders of magnitude to avoid further bleaching. The decay exhibits a strongly stretched exponential behavior. From the profile, an effective decay time of the absorption hole can be estimated yielding a value of longer than 10 hours. The intensity fluctuations are due to laser power fluctuations.

### Short term stability

Using the actively stabilized laser, a holographic and a transmission experiment were simultaneously performed. A big advantage of this method consists of the fact that from a comparison of the holographic to the absorption linewidth it can be concluded whether saturation broadening is present, since the hologram linewidth is always larger than the corresponding absorption hole. As a function of the total burn energy, the transmission and the hologram linewidth both increase linearly and extrapolation to zero intensity yields the same value [99]. In the low power limit the absorption hole is given by a convolution of the laser linewidths used for

burning and for readout. This is in contrast to spectral holes where the laser is narrower than the homogeneous linewidth, in which case a holewidth of twice the homogeneous linewidth is observed [101]. In Fig. (5.3) a spectral absorption hole and the corresponding holographic signal are shown. The transmission hole was burned

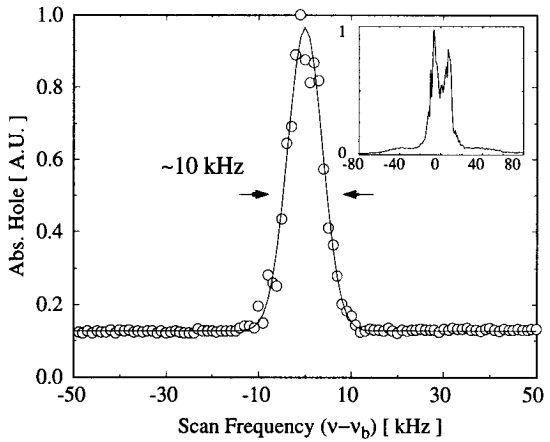


**Figure 5.3:** Absorption and holographically detected hole. The hologram, depicted in the inset shows clear saturation, even at such low intensities and short exposure times. Nevertheless, a linewidth of 10 kHz could be reproducibly measured in the absorption hole, guaranteeing that the laser linewidth is better than half of the hole width, i.e. 5kHz.

using an exposure time of 100 ms and a burn power of approximately 30 $\mu W/cm^2$. For the readout the laser was attenuated by a factor of 20. The spectral hole was read out several times for several minutes always yielding similar results. As can be seen from the dip at the center of the holographic signal shown in the inset, the spectral hole is already saturated [102]. Still, an absorption hole with a width of approximately 10 kHz could be burned, proving that an actual laser linewidth of maximally 5 kHz was achieved. Similar experiments had been carried out by Mitsunaga et al. [103]. Monitoring the spectrum of a transient hole they observed a linewidth of 5.3 kHz on the milliseconds time scale. Sellars et al. observed a 3.5 kHz spectral hole in $Eu^{3+}:Y_2O_3$ on the same time scale [104]. The 10 kHz persistent spectral holes observed here correspond to the narrowest holes yet measured on time scales longer than a few ms.

### 5.2.3 Determination of the Allan variance

The narrow line width of the transition, combined with the long term stability of the spectral holes allows for the verification of the long term performance of the laser system, using the time trajectory of a spectral hole.

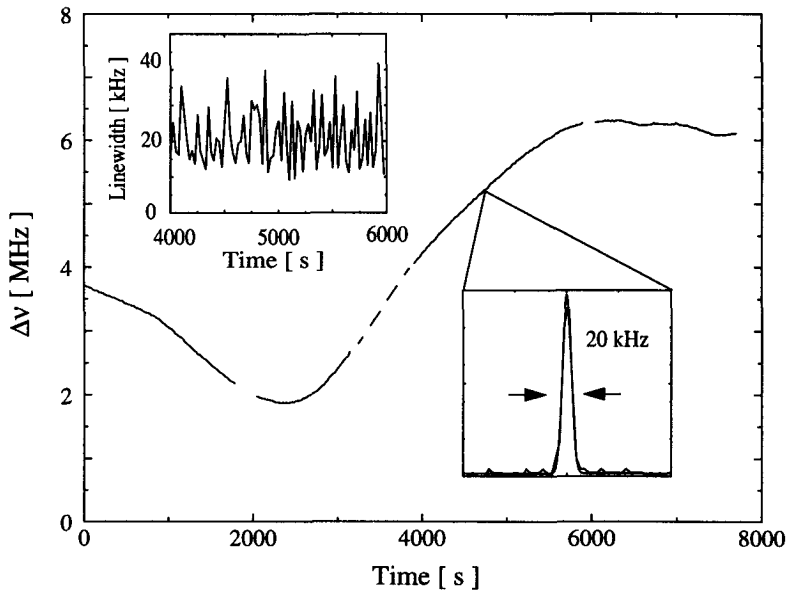


**Figure 5.4:** Trajectory of the laser frequency versus a spectral hologram. The trace shows the laser drift in this time frame. Spacings occur at positions where the laser lock was lost. This required the burning of a new hole. A typical spectral hologram is depicted in the lower inset, along with a fit to the line yielding a width of approximately 20 kHz. The upper inset shows the linewidth evolution for the time period of 2000 s - 4000 s. Fluctuations are in the range of 10 kHz given by the stability of the laser. With the obtained resolution no broadening of the spectral becomes apparent, yielding an estimate for the maximal spectral diffusion in $Eu^{3+}$ in $Y_2SiO_5$. For further details it is referred to the text.

In Fig. (5.4) such a trajectory of a holographic signal is shown. The sampling interval was chosen as 22 s, and a total time range of 8000 s was monitored. The trace is interrupted at temporal positions where the laser lock was lost. In this

case, a fresh hole was burned at a new frequency position. In the lower inset a typical spectral hologram is shown. A Gaussian was fitted to it, yielding a linewidth at FWHM of 20 kHz. This sets the maximal resolution to the experiment.[1] In the upper inset the evolution of the linewidth of the spectral hologram is shown for the the time window from 2000 -4000 s. With the given accuracy of the laser, no broadening can be observed. It can thus be concluded that these experiments demonstrate that the broadening induced by spectral diffusion in $Eu^{3+}$ in $Y_2SiO_5$ at a temperature of 1.7 K is less than 20 kHz/hour, with the value limited by the resolution of the laser. Moreover, the experiments reveal the presence of a long term drift of the laser/cavity system of approximately 4 MHz.

It is clear that time trajectories of spectral holograms offer an elegant way to measure the Allan variance of a system. The Allan variance $\sigma_A$ is defined as [105]

$$\sigma_A^2(\tau) = \frac{1}{(m-1)\nu^2} \sum_{k=1}^{m-1} \frac{(\langle \nu_{k+1} \rangle_\tau - \langle \nu_k \rangle_\tau)^2}{2} , \tag{5.2}$$

where $m$ denotes the number of successive measurements of $\langle \nu_k \rangle$ and $\langle \nu_{k+1} \rangle$, each averaged over successive time intervals of duration $\tau$, and $\nu$ stands for the optical frequency. Fig. (5.5) shows a comparison of three different locking procedures: (i) locked to the commercially available invar cavity of the 699-21 laser, (ii) locked to the homebuilt zerodur cavity without active temperature control and (iii) locked to the zerodur cavity with a temperature stability of 15 mK. Of main interest are the two extreme regimes: the short and the long term stability. It can be seen that at short times $\sigma_A \nu$ is approximately 20 kHz. This value is about a factor of two smaller than without temperature stabilization. As expected, the commercially locked laser has a short term fluctuation in the range of 1 MHz. The long term behavior indicates that the homemade cavity manifests about an order of magnitude less drift than the commercial system.

[1] This resolution changed from day to day and always had to be verified. Partly as commented above, the relatively broader line here is due to the fact that the width of the measured holographic spectral hole is always broader than the corresponding width observed in absorption.

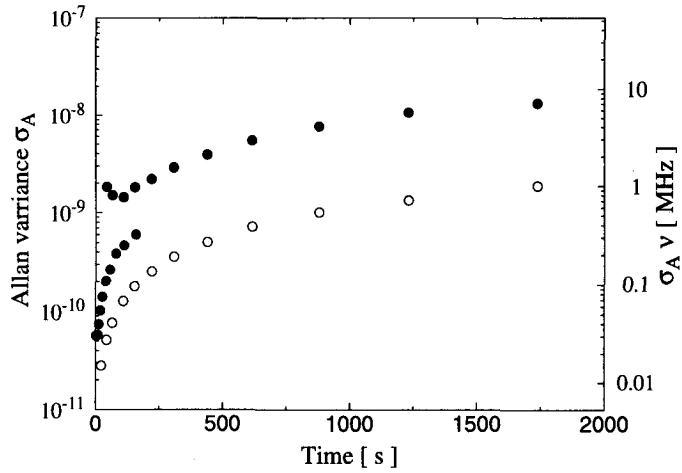


**Figure 5.5:** Allan variance for three different configurations: (from top to bottom). (i) commercial locking, (ii) Home built locking without temperature control and (iii) homebuilt locking with temperature control of the cavity. The axis are given in units of Allan variance $\sigma_A$ (left) and $\sigma_A \nu$ where $\nu$ is the optical transition frequency. Further details can be found in the text.

### *Thermal expansion coefficient*

In Chapter 4 the expansion coefficient $\kappa$ of zerodur was tabulated as $\kappa = 5 \cdot 10^{-8}$ K$^{-1}$. Keeping in mind that

$$\frac{\Delta\nu}{\nu} = \frac{\Delta n}{n} + \frac{\Delta l}{l} = \frac{\Delta n}{n} + \kappa \Delta T \tag{5.3}$$

a maximal frequency excursion of 370 kHz/15 mK would be expected to be thermally induced, a value about an order of magnitude smaller than the experimentally observed 4 MHz long term drift, again assuming a constant refractive index $n$. To clarify the origin of the drift and to verify its temperature dependence, the effective thermal expansion coefficient $\kappa'$ was measured, varying the temperature of the cavity while simultaneously monitoring the position of a spectral hole. The result is shown in Fig. (5.6). The relative drift between the laser frequency and the spectral

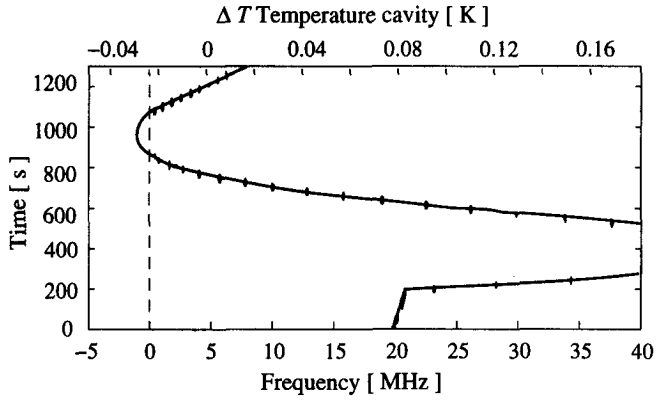


**Figure 5.6:** Temperature drift of a spectral hologram as a function of the cavity temperature. On the upper x-axis the temperature change of the reference cavity is shown in comparison to the frequency shift of the locked laser system (lower x-axis). The dashed line denotes the limit of the observable scan range.

position of the hologram is marked on the lower axis. The upper axis represents the measured temperature of the reference cavity. A comparison of the two scales directly allows for the determination of an effective expansion coefficient $\kappa'$, resulting in $\kappa' = 4.5 \cdot 10^{-7}\mathrm{K}^{-1}$. This value is about an order bigger than the thermal expansion coefficient of zerodur. Based on these measurements it can be concluded that for the laser/cavity configuration presented here, the main contributions to the long term laser fluctuations resulted from temperature effects. Further studies have shown that the glue with a glass point at 35°C, lead to a dramatic increase of $\kappa$.

## 5.3 High resolution PSHB spectroscopy

The use of hole burning to verify the laser performance is complementary to the application of highly stabilized laser systems in hole burning studies. In this Section an example is presented where spectroscopically interesting information could be extracted by means of the increased frequency resolution of the laser system presented and tested above. Fig. (5.7) (a) and (b) show a transmission hole and a hologram

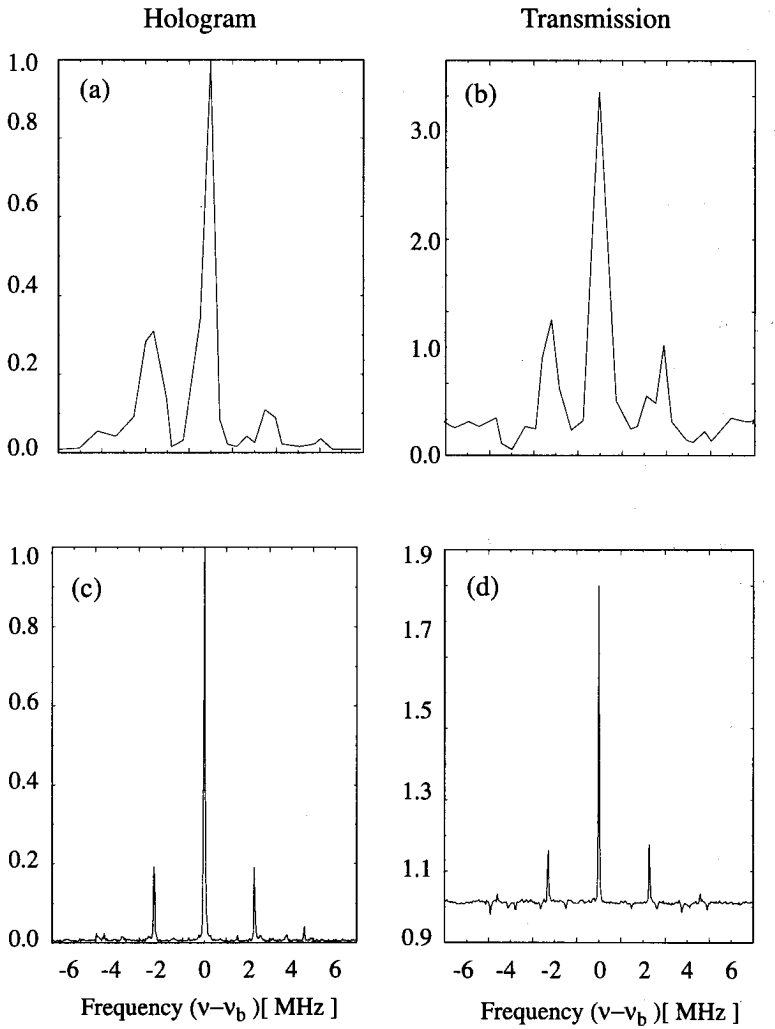


**Figure 5.7:** Comparison of a hole spectrum of the optical site II of $Pr^{3+}$:$Y_2SiO_5$ using fringe locking or Pound Drever locking. Traces (a) and (b) are reproduced from Ref [51] and scaled to the same scan range as the spectra recorded using the side band modulation ((c) and (d)). Traces (a) and (c) correspond to the holograms where as (b) and (d) are the respective transmission signals.

using a commercially locked dye laser of $Pr^{3+}$ in $Y_2SiO_5$ in site II (data taken from Ref. [51]). In (c) and (d), the corresponding spectra, measured using Pound Drever locking are shown. The exposure time was 100 ms and the spectra were read out several times. The frequency resolution enables one to determine the ground and excited state hyperfine splittings with a resolution of approximately 10 kHz. A fit to the data yields ground state splittings of $\Delta\nu_1 = 4.92$ MHz and $\Delta\nu_2 = 3.78$ MHz. In the excited state, the splittings are $\Delta\nu_3 = \Delta\nu_4 = 2.29$ MHz. Compared to earlier measurements with a frequency stabilized laser, the accuracy of these measurements is increased by one order of magnitude [53]. The given values for the hyperfine splittings are in excellent agreement with the results obtained from ODNMR [42, 51]. In this sense the current system offers a powerful alternative to double resonance techniques.

Apart from the relative frequency shifts between the different hyperfine levels, the hole burning spectrum contains information on the transition probabilities and therefore on the mixing of the wave functions as was shown in Chapter 2. To understand the hole formation process, one can subdivide it into three categories:

(1) Burning with intensity $\mathcal{I}_1$ at frequency $\nu_b$ leading to an excitation of levels exactly at resonance with $\nu_b$ with a transition amplitude $\langle g, i|e, j\rangle_1$.

(2) Relaxation from the excited state to the ground state with amplitude $\langle e, j|g, k\rangle_2$.

(3) Excitation with intensity $\mathcal{I}_3$ during readout at frequency $\nu$ with an amplitude $\langle g, k|e, f\rangle_3$.

Again, $|e\rangle$ and $|g\rangle$ denote the excited and the ground state, respectively and $(f, j, i, k)$ symbolize one of the corresponding hyperfine levels. Using Eq. (2.21), the total transition amplitude $a(i, f)$ from an initial hyperfine level $i$ to a final state $f$ thus reads

$$\begin{aligned} a(i,f) &= \langle g,i|e,j\rangle_1\langle e,j|g,k\rangle_2\langle g,k|e,f\rangle_3, \qquad (5.4)\\ \text{with } \langle e,j|g,k\rangle_2 &= \sum_{m,s}\langle e,j|s,m\rangle\langle s,m|g,k\rangle. \end{aligned}$$

As shown in Section 2.3, relaxation has to be considered over all possible paths

which is taken into account through $s$. In principle, the total spectrum can be simulated from the peak structure. However, if rigorously performed, the number of free parameters is very large, leading to big uncertainties in the result. For $Pr^{3+}$:$Y_2AlO_3$, Blasberg et al. determined the orientation of the quadrupole tensors which allowed for a reduction of the number of fitting parameters and thus permitted the calculation of the transition probabilities [52]. Holliday et al. [51] and Altner [53] attempted to determine the transition probabilities for $Y_2SiO_5$ without the knowledge of the orientation of the quadrupole tensor. To decrease the number of fit parameters they assumed that the terms $\langle \ldots \rangle_1$ and $\langle \ldots \rangle_2$ could simply be set to unity since they speculated that phonon induced redistribution would lead to equal transition probabilities during the burn and relaxation time. However, as the authors commented, the justification of this assumption was purely based on the reasonable fit of the simulated spectra to the experimental data.

The increased resolution of the here presented hole burning spectra allows for a verification of these simplifications. For this, attention is drawn to the two marked peaks in Fig. (5.8), labeled with (1) and (2). From the fit of the different hyperfine transitions, one can directly assign the individual peaks to a distinct excitation path. For peak (2), the transition amplitude is given by $\langle g,3|e,3\rangle_1\langle e,3|g,1\rangle_2\langle g,1|e,1\rangle_3$ and is expected to appear at $(\Delta\nu_1 + \Delta\nu_2 - \Delta\nu_3 - \Delta\nu_4) = 4.12$ MHz. Due to the fact that the excited state splittings are equal, peak (1) has two contributions, namely $\langle g,3|e,2\rangle_1\langle e,2|g,1\rangle_2\langle g,1|e,1\rangle_3$ and $\langle g,3|e,3\rangle_1\langle e,3|g,1\rangle_2\langle g,1|e,2\rangle_3$ at $(\Delta\nu_1 + \Delta\nu_2 - \Delta\nu_3) = 6.41$ MHz. Setting $\langle \ldots \rangle_1$ and $\langle \ldots \rangle_2$ to unity, one finds that peak (1) should be of equal or higher amplitude than peak (2) since the transition probabilities are additive. The experimental result shows an inverted behavior. It must therefore be concluded that for this system, the previously made assumptions do not hold.

From the relative intensities of the symmetric side-holes, further information about the hole formation process can be extracted. The side- and anti-holes, located symmetrically from to the central hole have equal absorption changes. This suggests that

$$\langle g,i|e,k\rangle_1\langle e,k|g,l\rangle_2\langle g,l|e,f\rangle_3 = \langle g,l|e,f\rangle_1\langle e,f|g,l\rangle_2\langle g,l|e,i\rangle_3 \,, \qquad (5.5)$$

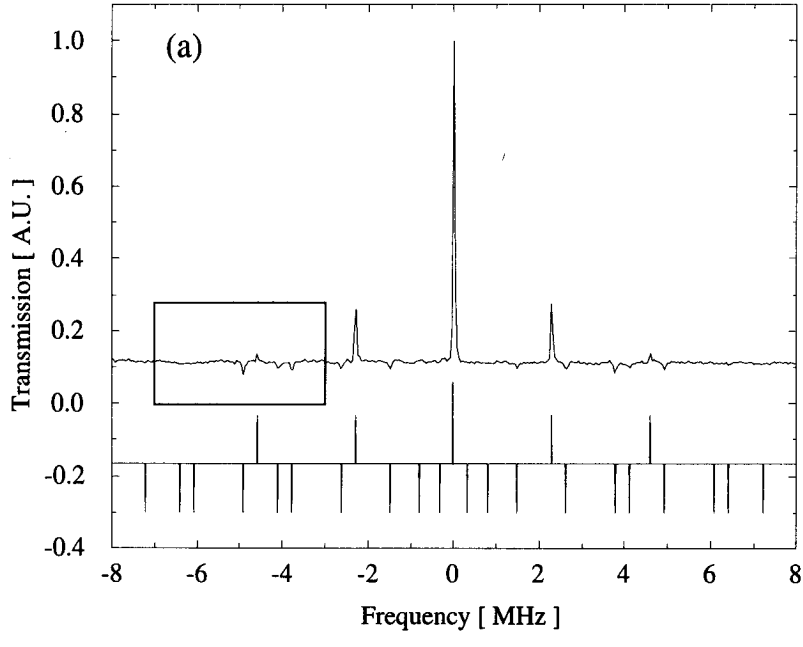


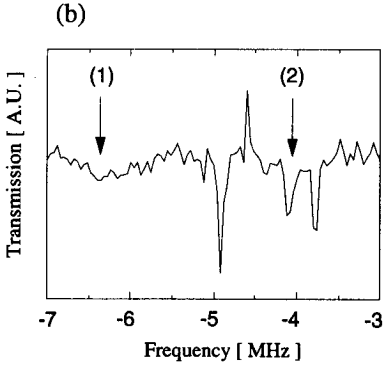


**Figure 5.8:** (a) Experimentally measured PSHB spectrum. Shown are the positions of all the expected side- and anti-holes along with the experimental transmission signal. Due to the equal splitting of the excited state hyperfine levels the hole spectrum is reduced from 42 anti-holes and 6 side-holes to 30 anti-holes and 4 side-holes. The zoomed in region (b) shows the hole structure in the region around 3-7 MHz. Under the assumption that selection rules are only assumed for $\langle \ldots \rangle_3$ a anti-hole is expected at 6.41 MHz (1) with an amplitude bigger than the hole shown at 4.12 MHz (2). The experiment shows an inverted behavior which indicates that the simplification does not hold. Details are given in the text.

which implies that indeed the relaxation process $\langle \ldots \rangle_2$ is strongly non-selective and that hole burning spectra can be simulated by setting this term to one. This is consistent with the observation of a short excitation lifetime (200 $\mu$s) compared to the inverse of the spontaneous emission rate of the order 1 s.

Earlier experiments showed asymmetric side-hole patterns which was taken as an indication for a purely readout selective process. However, these experiments had been carried out with comparably long pulses and high laser intensities. Thus, saturation may have been responsible for the observed asymmetries. That saturation can lead to asymmetric hole patterns can be easily visualized, by comparing the relative hole depths of side- and anti-holes symmetrically located around the zero-zero transition. The saturation behavior of the normalized hole depth $d$ can be written as

$$d(x, \mathcal{I}) = d_0[1 - \exp(-c\alpha(x)\mathcal{I}\Delta t)], \tag{5.6}$$

where $\mathcal{I}$ and $\Delta t$ stand for the intensity and exposure time during the burning process and $c$ and $d_0$ are constant factors. Finally, $\alpha(x)$ represents the absorption which is proportional to the transition probability $p(x)$ at the frequency of transition $x$. In the low intensity limit, Eq. (5.6) reduces to $d(x, \mathcal{I}) = c\alpha(x)\mathcal{I}\Delta t$. Using Eq. (5.6), and setting $\langle \ldots \rangle_2$ to unity, it can be seen that in order to obtain the observed hole depth, $d(x, \mathcal{I})$ needs to be multiplied with the transition probability $p(y)$ at the readout position $y$. Thus the amplitude ratio of the symmetrically located side- or anti-holes becomes

$$R = \frac{d(\langle g, i|e, k\rangle, \mathcal{I})\; p(\langle g, l|e, f\rangle)}{d(\langle g, l|e, f\rangle, \mathcal{I})\; p(\langle g, i|e, k\rangle)} \tag{5.7}$$

From Eq. (5.6) and Eq. (5.7) it is obvious that in the low burn intensity limit $R = 1$ is fulfilled. However, the onset of saturation depends on $p(x)$ and $p(y)$, which will generally lead to $R \neq 1$, i.e. the observation of asymmetries in the side- or anti-holes. It will further effect the relative peak heights between holes at different spectral positions. Indeed, when comparing earlier measurements to the present ones, (for an example see Fig. (5.7) (a) and Fig. (5.7) (c)), it can be observed that the relative heights of the holes tend to be quite different. This can lead to miss-

interpretations of the effective transition probabilities. In conclusion it can be stated that the mixing of the different hyperfine levels can in principle be determined from the hole burning spectra. However, different factors need to be considered before a direct assignment can be made.

## 5.4 Conclusions

In this Chapter it has been shown that PSHB can be used to monitor the laser performance. The Allan variances has been determined from the hole burning data and has been compared for different locking schemes. Using a temperature stabilized cavity the laser linewidth could be reduced to less than 5 kHz and the long term performance could be improved by an order of magnitude. By varying and monitoring the temperature of the reference cavity and simultaneously verifying the holes' spectral position, the thermal expansion coefficient of the cavity could be measured. Summarizing, it can be concluded that PSHB in $Eu^{3+}$:$Y_2SiO_5$ served as an ideal technique for monitoring, characterizing, and improving the laser/cavity system.

Complementary to the more technical application of PSHB, the improved laser system has been used to extract further spectroscopic information on the hole burning systems. Persistent spectral holes of $Eu^{3+}$:$Y_2SiO_5$ in site II have been monitored on the hour time scale and the spectral diffusion contribution was found to be smaller than 20 kHz/h, with the value still limited by the laser resolution. From the PSHB spectrum of $Pr^{3+}$ in $Y_2SiO_5$, all hyperfine splittings could be resolved with a resolution of 10 kHz. Finally, it has been shown that previously made assumptions on the hyperfine hole burning dynamics are not consistent with the experimental spectra shown here, and possible reasons for this were presented.

# 6. Stark effect in rare earth ion doped crystals

The effect of an externally applied electric field is studied for rare earth ion doped crystals. A general theory is presented which allows for the determination of the number of static dipole moment differences for a given crystal symmetry. Two experimental methods are described which allow for the measurement of the magnitude of the induced dipole moments. It is demonstrated that the orientations of the dipole moments and of the crystal axes can be determined with subdegree accuracy. The effect of an electric field pulse as a perturber of the photon echo is analyzed, and it is shown that for the systems under investigation, the application of an electric field can be treated as a fully deterministic and therefore reversible perturbation.

## 6.1 Introduction

The effect of external fields has been extensively studied in all fields of spectroscopy. Of interest were mainly the determination of electronic properties such as polarizability and dipole moments. Over the years extensive investigations have been carried out on molecular and ionic systems, in the gas phase as well as in solids. Such studies have also concentrated on the investigations of RE ion doped solids. However, to observe the influence of externally applied fields on an inhomogeneous linewidth level, very large fields needed to be applied, yielding a poor resolution. The use of subinhomogeneous linewidth resolution methods such as hole burning or non-linear spectroscopy have therefore been very successfully applied in the investigation of external field effects in RE ion doped crystals.

The analysis of magnetic and electronic dipole interactions in RE ion doped crystals has lately achieved an increased interest, and lead to a better understanding of stochastic interactions in solids [25, 106, 107]. Much work has been put into the determination of magnetic moments. Techniques such as Raman heterodyning [48, 50, 52, 108, 109], ODNMR [20, 110], Zeeman splittings of spectral holes [111] or magnetic resonance [29], have yielded very precise measurements of the magnitudes of magnetic moments. The cited work does by no means give a complete overview over the entire field and it is referred to Ref. [8] for more details.

Apart from the magnetic moments, the electric properties have always been of big interest for spectroscopists. In molecular systems in solids, the influence of an electric field has been studied very carefully [112–114], even on the single molecule level [115, 116]. Compared to that, little work concentrated on the Stark effect in RE ion doped crystals [117, 118]. With the introduction of Stark modulated photon echoes (SMPE) [119, 120], the resolution could be drastically increased which allowed for the measurement of very small electric dipole moment differences. However, a complete theory of splitting and broadening of spectral holes and the resulting modulation of the photon echoes was not given up to now.

This gap is closed here. A generalized theory of SMPE in RE ion doped crystals is presented, showing that usually the photon echo intensity exhibits a complex oscillatory behavior with two or more frequency components. This derives from the interference of the static dipole moment differences of ions located at inequivalent sites. Experimental results of SMPE in a $Pr^{3+}$ and $Eu^{3+}$ co-doped $YAlO_3$ and a $Pr^{3+}$ doped $Y_2SiO_5$ crystal are shown and it is demonstrated that the orientations of the dipole moment differences and of the crystal axes can be determined with subdegree accuracy.

The success of SMPE was largely based on the increased spectral resolution which allowed for the observation of shifts in the kHz range. However, under certain circumstances, SMPE spectroscopy becomes difficult. In such cases the measurement of electric field induced persistent hole splitting becomes an alternative. Using the active laser stabilization presented in the preceding Chapters, kHz Stark splittings of persistent holes could be observed.

The interaction of an impurity and its environment has been one of the major interests of impurity spectroscopy in solids, even of the entire field of solid state physics. In principle one can subdivide interactions into two forms: deterministic and stochastic interactions. Here, the term deterministic interaction is used to describe cases where after the application of the external deterministic perturbation the system immediately returns to its former configuration. Opposed to that are stochastic interactions, where the external (also deterministic) perturbation results in configurational changes in the environment which relax stochastically towards the thermal equilibrium configuration and thus act as a stochastic perturbation. Throughout this work these two forms will be referred to as deterministic or stochastic perturbation. Here, the reversibility upon the application of electric fields in RE ion doped crystals is investigated by means of SMPE spectroscopy.

The Chapter is structured as follows: in Section 6.2 a generalized SMPE theory is presented and experiments in different crystals are carried out. In Section 6.3 results of high resolution Stark splitting in $Eu^{3+}$ in $Y_2SiO_5$ are presented. Finally, Section 6.4 is devoted to the analysis of the reversibility of an electric field perturbation.

## 6.2 Site interference in SMPE

The recently developed technique of electric-field (or Stark) modulated photon-echo (SMPE) spectroscopy, has opened up a new way of measuring small Stark shifts induced by a static electric field in impurity-ion doped crystals [119–123]. The SMPE technique measures the 2PPE intensity, when a static electric field pulse (Stark pulse) is applied during the dephasing period, between the first pulse and the second pulse, or during the rephasing period between the second pulse and the echo. By recording the echo intensity $I$ as a function of the Stark pulse width $\tau_S$, one obtains a modulation pattern that gives the Stark shift frequencies as will be discussed in detail below. In comparison to the competing hole-burning techniques [51, 94, 117, 118], where the resolution is limited by the laser linewidth, the resolution of SMPE is solely determined by the pulse separation. Since for some RE ion transitions the pulse separation can be extended up to milliseconds due to the long dephasing time $T_2$, SMPE ensures the measurement of Stark shifts as small as 1 kHz or even less. Moreover, in contrast to hole-burning techniques, persistence of holes is not required.

### 6.2.1 Theory

Here, the behavior of the photon echo intensity upon application of an electric field pulse during the interpulse time $t_{12}$ is analyzed, starting from general considerations regarding SMPE behavior in crystals. Propagation effects and inhomogeneities in the excitation are ignored. Using Eq. (3.14), Eq. (3.15), and Eq. (3.20), for a discrete set of $N$ ions the photon echo $I$ normalized to the perfect rephasing case is expressed as

$$I = \left| \frac{1}{N} \sum_{j=1}^{N} \mathbf{P}_{0j} \left\langle \exp\left[ i \int_0^{t_{12}} \omega_j(t)\,\mathrm{d}t - i \int_{t_{12}}^{2t_{12}} \omega_j(t)\,\mathrm{d}t \right] \right\rangle \right|^2 , \qquad (6.1)$$

where $j$ runs over all $N$ participating ions and $\omega_j(t)$ denotes the $j$th ions resonance frequency. The amplitude $\mathbf{P}_{0j}$ depends on the angle between the transition dipole moment and the laser polarization.

In what follows, the case is analyzed, where at $t = t_0$ during the dephasing

period an electric field pulse $\mathbf{E}_S$ with pulse width $\tau_S$ is applied. This leads to a shift of the resonance frequencies. For the $j$th ion this can be written as

$$\omega_j(t) = \omega_{j0}(t) + k\ \Omega_j,\ \text{with}\ k = \begin{cases} 1 & : \ t_0 < t < t_0 + \tau_S \\ 0 & : \ \text{otherwise}\ , \end{cases} \tag{6.2}$$

implicitly assuming that after the application of the electric pulse the resonance frequency returns to its original value. This assumption will be verified in Section 6.4. The fluctuations of $\omega_{j0}(t)$ that lead to an echo attenuation due to dephasing will be studied in detail in Chapter 7. Here, they can be factored out since the echo is probed at a constant optical inter pulse time $t_{12}$. Therefore the averaging only yields a constant scaling factor, which can be set to unity. Thus, one only needs to consider the modulation caused by the Stark shift. Within the linear approximation, the Stark shift depends on the orientations of the ground and the excited state static dipole moments which in turn depend on the site the ion is located at. Explicitly, the Stark shift $\Omega_k$ of the $k$th site is given by $\Omega_k = (\delta\boldsymbol{\mu}_k \cdot \mathbf{E}_S)/\hbar$, where $\delta\boldsymbol{\mu}_k = \boldsymbol{\mu}_{ek} - \boldsymbol{\mu}_{gk}$ is the difference between the excited- and ground-state dipole moments, which is referred to as dipole moment hereafter.[1] Therefore, the number of sites $n_s$ corresponds to the number of possible Stark shifts. Assuming for simplicity that the impurity ions are randomly distributed, Eq. (6.1) can be rewritten as

$$I(\tau_S) = \left| \frac{1}{n_s} \sum_{k=1}^{n_s} \mathbf{P}_{0k} \exp\left[i\Omega_k \tau_S\right] \right|^2 . \tag{6.3}$$

Eq. (6.3) implies that $I(\tau_S)$ follows a complicated modulation behavior, which results from the interference between polarizations at different sites. By Fourier-transformation of $I(\tau_S)$, the Stark frequencies $\Omega_k$'s can be determined. The $\Omega_k$'s, recorded as a function of the $\mathbf{E}_S$ orientation allow for an accurate measurement of the orientations of the dipole moment, as well as of the crystal axes. This technique is analogous to that of optically detected nuclear magnetic resonance [124, 125] or Raman heterodyne detection [50], where the rotation of the static magnetic field

[1] Both, $\mathbf{E}_S$ and the $\delta\boldsymbol{\mu}_k$'s are assumed to be aligned along one distinct direction. In Section 6.4 it is shown that a non-prefect alignment leads to damping of the SMPE intensity.

is used to determine the crystal axes and nuclear quadrupole axes. Therefore, the present technique becomes a powerful alternative to identify crystal axes by optical means. Site interference was also reported for Stark-switched free induction decay [117], which differs from the SMPE technique in its spectral resolution, limited by the laser linewidth. It is important to note that the interferences described here are different from quantum beats. Quantum beats originate from a single quantum system, while here the modulations stem from two or more sets of oscillators with slightly different frequencies.

The remaining question is how to obtain the $\Omega_k$'s. In general, an impurity ion is located at one of several crystal sites that are related to each other by symmetry operations. Since, for a given crystal, the site symmetry group $\mathcal{G}_s$ is a subgroup of the crystal symmetry group $\mathcal{G}_c$, the number $n_s$ of different sites can be obtained by dividing the order $g_c$ of $\mathcal{G}_c$ by the order $g_s$ of $\mathcal{G}_s$ ($n_s = g_c/g_s$). All the different sites form cosets in $\mathcal{G}_c$ [126] and, accordingly, the symmetry operations leading from one to another site are given. Furthermore, the dipole moment $\delta\boldsymbol{\mu}_1$ has to transform as the identity representation of $\mathcal{G}_s$. This implies that the inversion element can not be contained in $\mathcal{G}_s$ in order to have a non-vanishing dipole moment. Once $\delta\boldsymbol{\mu}_1$ is fixed, all the $\delta\boldsymbol{\mu}_k$'s ($k = 2,\ldots,n_s$) can be calculated by applying the symmetry operations of $\mathcal{G}_c$ to $\delta\boldsymbol{\mu}_1$ [109]. In the case where $\mathcal{G}_c$ has an inversion symmetry, $n_s$ is an even number, i.e. $n_s = 2n_i$, where $n_i$ is the number of inequivalent sites. Thus, $\Omega_{n_i+k} = -\Omega_k$ for $k = 1,2,\ldots,n_i$. In this case Eq. (6.3) reduces to

$$I(\tau_S) = \left| \frac{1}{n_i} \sum_{k=1}^{n_i} \mathbf{P}_{0k} \cos(\Omega_k \tau_S) \right|^2 . \tag{6.4}$$

To better visualize the meaning of Eq. (6.4), the easiest possible case is considered first, namely if a single modulation frequency occurs. This corresponds to the observation of Wang and Meltzer [119] and Meixner et al. [120]. In Fig. (6.1) the phase evolution of a 2PPE is compared to that in SMPE spectroscopy. As discussed in Chapter 3, in the case of a 2PPE, due to slightly different resonance frequencies the polarization of the ions interfere randomly after a short time and no macroscopic polarization is observed. Due to the application of a second pulse at $t = t_{12}$, a photon echo is observed at twice the interpulse time. In the case of SMPE

an electric field pulse of length $\tau_S$ is applied within the dephasing period. For the sake of simplicity, the dipole moments of the ions are assumed to be aligned either parallel or anti-parallel to the electric field. As shown in Fig. (6.1) (b), this leads

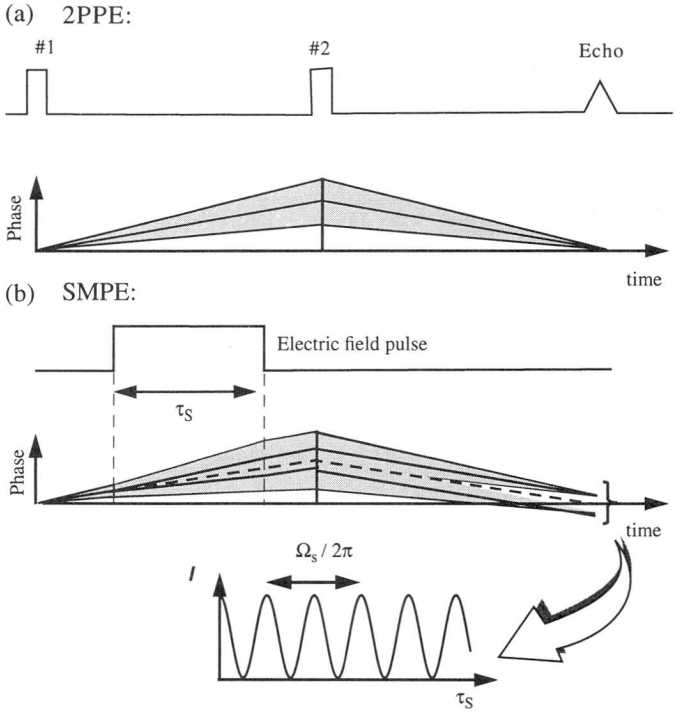


**Figure 6.1:** (a) Formation of a 2PPE. Shown is the phase evolution of the ensemble. As mentioned in Chapter 3, instead of a phase jump at $t = t_{12}$, here an inversion of the precision direction is illustrated. If an electric field is applied within the dephasing period an additional phase factor is accumulated (b). The magnitude of the phase shifts depends on the scalar product of the electric field and the dipole moment difference vectors. This leads to the formation of two macroscopic polarizations with different phases at $t = 2t_{12}$.

to an additional shift during the electric field pulse duration $\tau_S$ with its polarity depending on the alignment of the dipole moments. If reversibility is assumed, after the application of the electric field the slope of the phase evolution of every single frequency component will be identical to the one before. Thus, at the echo recovery

time again a macroscopic polarization will be formed. However, for the two different sets of ions (parallel and anti-parallel), the phase of the the polarization will be shifted, resulting in a beating of two macroscopic polarizations.

To clarify the determination of possible dipole moments from group theory, the case of a $YAlO_3$ crystal is analyzed, even though some of the statements may appear trivial. However, the approach can be adapted to more complicated systems. Here, the crystal symmetry group $\mathcal{G}_c$ corresponds to $D_{2h}$, resulting in $g_c = 8$, and the site symmetry group $\mathcal{G}_s$ is $C_{1h}$ with $g_s = 2$. Thus $n_s = 4$ and $n_i = 2$. Here, the a-b plane corresponds to the mirror plane of the $C_{1h}$ group.[2] Using the character table for $C_{1h}$ shown in Table 6.1, one finds that the dipole moments must lay within the mirror plane, since only those vectors transform as the identity. Consequently the

| $C_{1h}$ | E | $\sigma_h$ |
|---|---|---|
| A'; a,b | 1 | 1 |
| A; c | 1 | -1 |

**Table 6.1:** Character table for the $C_{1h}$ group. Only vectors which transform as A' can contribute to a linear electric dipole moment difference.

two inequivalent dipole moments can be expressed as $\delta\boldsymbol{\mu}_1 = \delta\mu\,(\cos\alpha_S, \sin\alpha_S, 0)$ and $\delta\boldsymbol{\mu}_2 = \delta\mu\,(\cos\alpha_S, -\sin\alpha_S, 0)$, with $\delta\mu = |\delta\boldsymbol{\mu}_k|$, $\forall k$. $\delta\mu$ and $\alpha_S$ are parameters to be determined experimentally. If the direction of $\mathbf{E}_S$ is given by polar and azimuthal angles $\theta_S$ and $\phi_S$, the two Stark split frequencies are $\Omega_1 = \Omega_S \sin\theta_S \cos(\phi_S - \alpha_S)$ and $\Omega_2 = \Omega_S \sin\theta_S \cos(\phi_S + \alpha_S)$, where $\Omega_S$ was defined as $\Omega_S = |\mathbf{E}_S|\,\delta\mu/\hbar$. Generally, if $\mathcal{G}_c$ and $\mathcal{G}_s$ are known, the SMPE behavior can be calculated from Eq. (6.4). In Table 6.2, expected modulation frequencies are summarized for crystals often used in high resolution spectroscopy, i.e., $LaF_3$ [117], $YAlO_3$ [50, 109, 124, 125] , $Y_2SiO_5$ [41, 42, 51], YAG ($Y_3Al_5O_{12}$) [8], and $Y_2O_3$ [127], along with the previously described parameters. For cases with high site symmetry, like for a YAG crystal, the dipole moments vanish and no Stark modulation is expected. Otherwise, two or three inequivalent sites are predicted to cause interference.

[2] In Ref. [120] the mirror plane is called a-c plane. Here the c-axis is taken perpendicular to the mirror plane.

| Crystal | $\mathcal{G}_s$ ($g_s$) | $\mathcal{G}_c$ ($g_c$) | $n_i$: | $\delta\mu_k^a$ | $\Omega_k$ |
|---|---|---|---|---|---|
| $LaF_3$ | $C_2$ (2) | $D_{3d}$ (12) | 3 | $\delta\mu_1 = (\delta\mu, \pi/2, 0)$<br>$\delta\mu_2 = (\delta\mu, \pi/2, \pi/3)$<br>$\delta\mu_3 = (\delta\mu, \pi/2, -\pi/3)$ | $\Omega_1 = \Omega_S \sin\theta_S \cos\phi_S$<br>$\Omega_2 = \Omega_S \sin\theta_S \cos(\phi_S - \frac{\pi}{3})$<br>$\Omega_3 = \Omega_S \sin\theta_S \cos(\phi_S + \frac{\pi}{3})$ |
| $YAlO_3$ | $C_{1h}$ (2) | $D_{2h}$ (8) | 2 | $\delta\mu_1 = (\delta\mu, \pi/2, \alpha_S)$<br>$\delta\mu_2 = (\delta\mu, \pi/2, -\alpha_S)$ | $\Omega_1 = \Omega_S \sin\theta_S \cos(\phi_S - \alpha_S)$<br>$\Omega_2 = \Omega_S \sin\theta_S \cos(\phi_S + \alpha_S)$ |
| $Y_2SiO_5$ | $C_1$ (1) | $C_{2h}$ (4) | 2 | $\delta\mu_1 = (\mu, \beta_S, \alpha_S)$<br>$\delta\mu_2 = (\delta\mu, \pi - \beta_S, \alpha_S)$ | $\Omega_1 = \Omega_S [\mathcal{A} + \cos\theta_S \cos\beta_S]$<br>$\Omega_2 = \Omega_S [\mathcal{A} - \cos\theta_S \cos\beta_S]$ |
| YAG | $D_2$ (4) | $O_h$ (48) | 6 | $\delta\mu_k = 0$ | no modulation |
| $Y_2O_3$ | $C_2$ (2) | $T_h$ (24) | $6^b$ | $\delta\mu_1 = (\delta\mu, \pi/2, 0)$<br>$\delta\mu_2 = (\delta\mu, \pi/2, \pi/2)$<br>$\delta\mu_3 = (\delta\mu, 0, 0)$ | $\Omega_1 = \Omega_S \sin\theta_S \cos\phi_S$<br>$\Omega_2 = \Omega_S \sin\theta_S \sin\phi_S$<br>$\Omega_3 = \Omega_S \cos\theta_S$ |

**Table 6.2:** Summary of modulation frequencies $\Omega_i$ for typical crystals. All crystals have an inversion center therefore Eq. (6.4) can be applied, i.e. $n_i = n_s/2$. In the case of $Y_2O_3$ all three components are doubly degenerated and $\mathcal{A}$ is defined as $\mathcal{A} \equiv \sin\theta_S \sin\beta_S \cos(\phi_S - \alpha_S)$. For $YAlO_3$ the angle $\xi$ enclosed by the two dipole moments becomes $\xi = 2\alpha_S$. In $Y_2SiO_5$ $\xi = 2\beta_S$. Footnotes: [a]: $\delta\mu_k$ is expressed in spherical coordinates $(\delta\mu, \beta_S, \alpha_S)$.[b]: All three components are doubly degenerate.

### 6.2.2 Experimental setup

The SMPE experiment in $YAlO_3$ was performed using a 0.1 at. % $Eu^{3+}$: 0.01 at. % $Pr^{3+}$: 0.01 at. % $Nd^{3+}$: $YAlO_3$ crystal [128] of size 5 × 5 × 10 $mm^3$, with the long dimension parallel to the crystal c-axis. The multiple-doped crystal proved to be quite useful in checking whether the crystal axes obtained for one ion species coincide with those for the other ones. As shown in Fig. (6.2) the tetragonally shaped sample was embedded in a cylindrical poly-urethane mantle and could be rotated about the crystal c-axis while the electrodes were kept fixed. The Stark

plates were indium tin oxide (ITO) coated and spaced by 13.3 mm. Voltages up to $\sim$ 200 V could be applied. The dielectric constant of the mantle was chosen to be close to that of the crystal, to ensure a constant electric field upon rotation. Experiments carried out without a mantle resulted in non-sinusoidal modulations. The sample holder, constructed by A. Hunkeler was designed for these experiments.

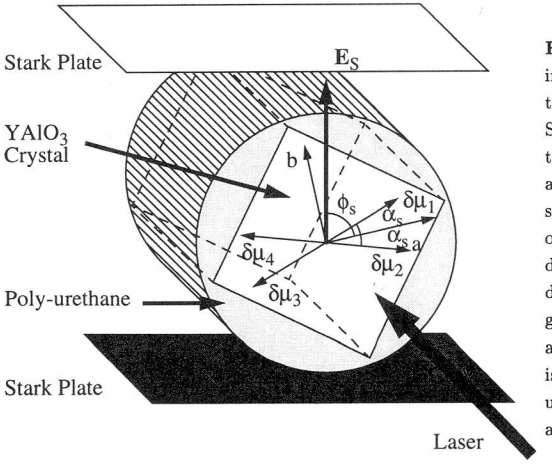


**Figure 6.2:** Experimental configuration of the $YAlO_3$ crystal and the Stark field $\mathbf{E}_S$. The crystal can be rotated in the a-b plane in a rotating sample holder with a fixed orientation of $\mathbf{E}_S$. The dipole moments of four different sites form the angle $\alpha_S$ with the crystal a-axis. The laser beam is propagating perpendicular to the a-b plane (parallel to the c-axis).

The sample holder was built out of a non-conductive material.[3] The holder was constructed such that the crystal could be freely rotated while the electrodes were kept fixed. This configuration yielded a strongly attenuated electric field at the sample since the dielectric constant of the mantle plus sample was much higher than the vacuum value. Therefore, the absolute value of the Stark coefficient was measured separately, using directly contacting electrodes, in which case the external electric field was directly given through the ratio of the voltage to the distance of the electrodes (planar plate configuration). The setup is shown in Fig. (6.3). For the photon echo measurement, a single-frequency tunable dye laser (CR 699-21) beam was chopped by a couple of acousto-optic modulators (AOM's) to generate two excitation pulses. In the case of $YAlO_3$, the laser wavelength was tuned either to the $^7F_0$-$^5D_0$ transition (581.68 nm) of the $Eu^{3+}$ ions or to the $^3H_4$-$^1D_2$ transition

[3]Ertacethal Angst & Pfister AG, Zürich, Switzerland.

(610.53 nm) of the $Pr^{3+}$ ions. The beam of power ~60 mW was focused by a lens (focal length = 85 mm) onto the center of rotation and was propagating along the crystal c-axis as shown in Fig. (6.2). The echo signal, after passing through an AOM shutter (AOM3), was detected by a photo-multiplier and recorded using boxcar integration. For the investigation of $Y_2SiO_5$, a 0.1 at. % $Pr^{3+}$ doped $Y_2SiO_5$ crystal was chosen with the optically allowed transitions ($^3H_4$-$^1D_2$) at 607.770 nm and 605.813 nm [41,42,51]. The experiments were carried out at a temperature of 1.7 K.

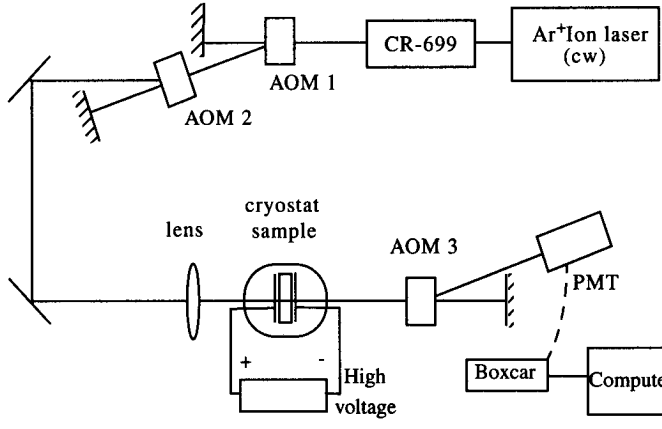


**Figure 6.3:** Experimental setup. Details are given in the text.

In both crystal hosts experimentally studied in this Chapter, the low crystal symmetry leads to a triaxial dielectric tensor resulting in a varying dielectric crystalline coefficient upon rotation. Since the axes of the dielectric tensor are quite generally not parallel to any of the dipole moments this should lead to deviations from the sinusoidal behavior as a function of the electric field orientation angles predicated according to Eq. (6.4). However, as will be shown below, perfect sinusoidal modulations were observed, indicating that the effective field change is very small upon rotation. There are different possible reasons for this: an almost spherical dielectric tensor and/or, a not very sensitive detection method to changes of the dielectric tensor. To verify the latter assumption, the magnitude of the expected change was roughly estimated. The sample/mantle were approximated by a sphere

with a dielectric constant of $\epsilon(0) \simeq 7$, a typical value for such crystals. The exact electrode distances corresponded to the ones used in the experimental configuration. Assuming an asymmetry of 20% in the dielectric axes resulted in an field change of roughly 10%. Thus, an approximate maximal magnitude of the dielectric tensor asymmetry of the mantle/crystal configuration can be estimated from the experimental results.

### 6.2.3 Results

#### (i) $Pr^{3+} : Eu^{3+} : YAlO_3$

In $YAlO_3$, generally two modulation frequencies are expected as can be seen from Table (6.2). According to the chosen geometrical configuration, $\theta_S = 90°$ and consequently $\Omega_1$ and $\Omega_2$ depend only on $\phi_S$. The position of the dipole moments are schematically shown in Fig. (6.1). In Fig. (6.4) experimental results are presented for $Eu^{3+}$ and $Pr^{3+}$ for a changing angle of the electric field.

For both investigated ions no polarization dependence of the modulation patterns was observed, although the magnitude of the signal changed. This observation implies that all amplitude factors $\mathbf{P}_{0j}$ in Eq. (6.4) are identical and can be set to unity. Thus, four components are expected in the Fourier transform of the modulation pattern, with frequencies $2\Omega_2$, $\Omega_2 + \Omega_1$, $\Omega_2 - \Omega_1$, and $2\Omega_1$ and intensity ratios of 1:2:2:1. It is worth noticing in particular that if the electric field is applied along an axis all four frequency components become equal. This corresponds to the geometry used by Wang and Meltzer [119], which explains their observation of a single sinusoidal modulation curve.

In Fig. (6.5) a comparison of two experimentally measured modulation curves are shown, along with the theoretically fitted traces. The Fourier transformed spectra are depicted in the insets. In the case of $\phi_S = -8°$ (a,b), the two frequency components are very close to each other, indicating that the electric field is applied almost parallel to one axis. The frequency components can be best identified by Fourier transformation of the modulation, which provides good initial guesses for the fitting procedure. Fig. (6.5) (c,d) shows a configuration where the four fre-

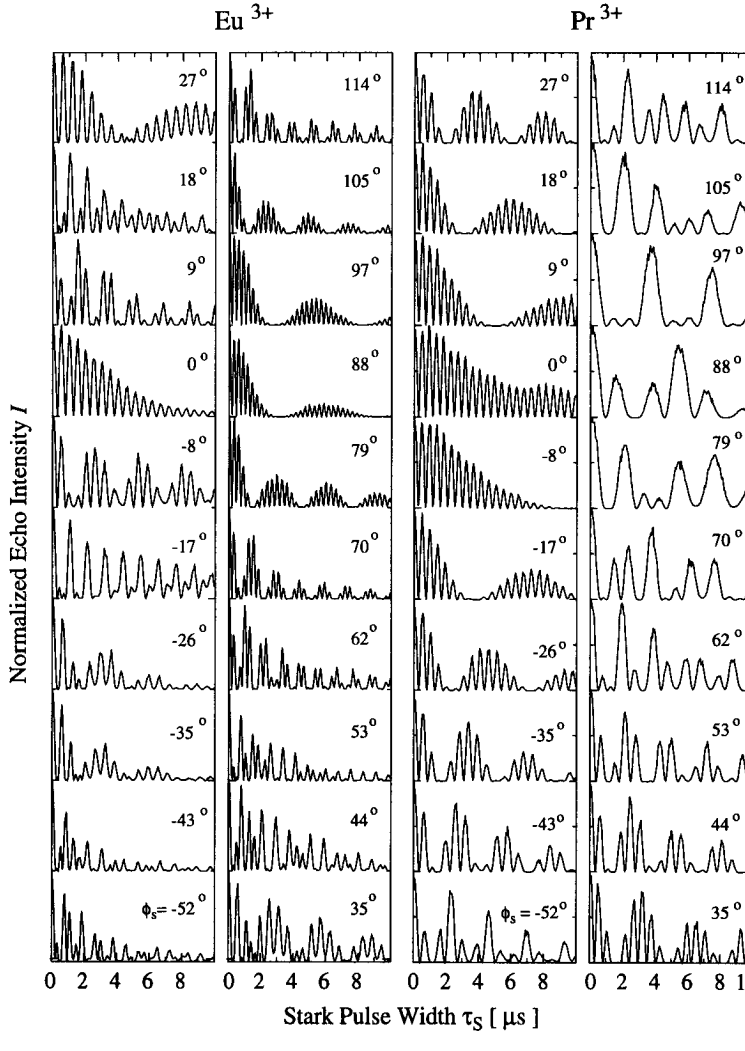


**Figure 6.4:** Modulation of the echo intensity for varying angle of the externally applied electric field. Shown are the modulations observed for $Eu^{3+}$ ($Pr^{3+}$) in $YAlO_3$ on the left and correspondingly on the right side. For $Pr^{3+}$ the frequency is slightly higher. The temporal decay of the signal is due to inhomogeneities of the Stark field in the crystal; for the fits it was approximated by an exponential.

quency components become clearly visible. The frequency components could be obtained with a standard deviation of better than 1 kHz/(Vcm$^{-1}$). The temporal decay of the signal is due to inhomogeneities of the Stark field in the crystal; here it was approximated by an exponential. Fitting was performed for all modulations shown in Fig. (6.4). Plotting $\Omega_1$ and $\Omega_2$ as a function of the rotation angle $\phi_S$, the

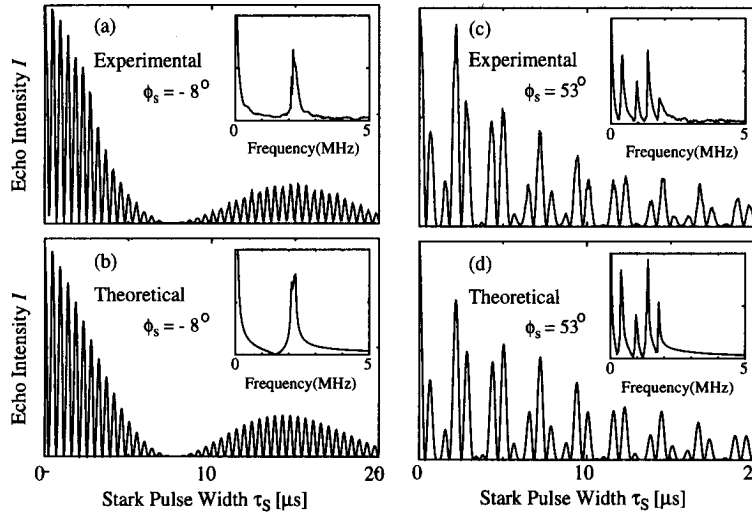


**Figure 6.5:** SMPE spectroscopy for the $^7F_0$-$^5D_0$ transition of $Eu^{3+}$:$YAlO_3$ at 581.68 nm. The pulse width $\tau_S$ of the Stark pulses was varied at a step size of 0.05$\mu$s. (a,c) Experimental plot of the echo decay for $\phi_S = 8°$, 53° and (b,d) theoretical fit according to Eq. (6.4) In the insets the corresponding Fourier transforms are shown.

orientations of the dipole moments at different sites for $Eu^{3+}$ and $Pr^{3+}$ could by determined. The results shown in Fig. (6.6) for $Eu^{3+}$ (a) and for $Pr^{3+}$ (b), were fitted to $\Omega_S \mid \cos(\phi_S \pm \alpha_S) \mid$, yielding the magnitudes and orientations of the two dipole moments as well as the orientation of the two crystal axes.[4] As mentioned earlier, the fitting of the theoretical curve to the experimental data is excellent and the maxima for the two modulation curves are of equal height, thus indicating a small electric field change upon rotation. Clearly the two ions gave the same

[4]Fitting was performed using Levenberg-Marquardt least-square algorithm. The standard deviations values are given with a 95% accuracy assuming student-t distribution.

orientations of the a and b axes. The directions of the dipole moments were determined as $\alpha_S = 13.7 \pm 0.6°$ for $Eu^{3+}$ and $\alpha_S = 60.8 \pm 0.4°$ for $Pr^{3+}$. The $Pr^{3+}$ result differs by about 6° from the 55° reported in Ref. [121]. The asterisks represent the additional measurements obtained for contacting electrodes. The modulations where scaled to intersect with these measurements. The Stark coefficients $\zeta_S$, with

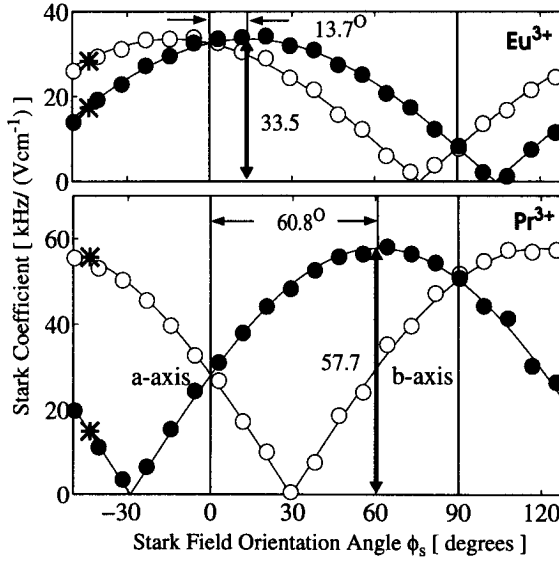


**Figure 6.6:** Stark coefficients for two inequivalent sites (open circles and filled circles) as a function of Stark field orientation for the $Eu^{3+}$:$YAlO_3$, $^7F_0$-$^5D_0$, and the $Pr^{3+}$:$YAlO_3$, $^3H_4$ – $^1D_2$ transition, respectively. The asterisks indicate the additional measurements obtained for contacting electrodes. The absolute magnitude of the modulation was determined by fitting the modulation pattern to these values. The fact that equal maxima of the modulation patterns are observed further supports the assumption of a negligible dielectric tensor asymmetry effect. If no polymer mantle was employed unequal modulation maxima where observed, which serves as further support.

$\zeta_S = \Omega_S|\mathbf{E}_S|^{-1}/(2\pi)$, were determined as $\zeta_S$= 33.5 ±1.6 kHz/(Vcm$^{-1}$) for $Eu^{3+}$ and $\zeta_S$ =57.7 ±2.7 kHz/(Vcm$^{-1}$) for $Pr^{3+}$. For $Pr^{3+}$ the present value is in good agreement with the previously obtained result [121], whereas for $Eu^{3+}$ it is at variance with earlier work [120]. For comparison, previously reported values and the present results are listed in Table 6.3.

| | Literature | Present work |
|---|---|---|
| $\zeta_S(Eu^{3+})$[kHz/(Vcm$^{-1}$)] | 45.5 | 33.5 ±1.5 |
| $\alpha_S(Eu^{3+})$[deg] | | 13.7 ±0.7 |
| $\zeta_S(Pr^{3+})$ [kHz/(Vcm$^{-1}$)] | 58.5 | 57.7 ±2.7 |
| $\alpha_S(Pr^{3+})$[deg] | 55 | 60.8 ±0.4 |

**Table 6.3:** Summary and comparison of experimental results in $YAlO_3$. The literature values of $Eu^{3+}$ and $Pr^{3+}$ are taken from Ref. [120] and Ref. [121], respectively.

### (ii) $Pr^{3+} : Y_2SiO_5$

In the case of $Y_2SiO_5$, again two frequency components are expected without any restrictions of the dipole moments to the (a-b) plane as can be seen from Table 6.2. For such a configuration the dipole moments cannot be determined from a two dimensional experiment. However, SMPE can be measured along two orthogonal planes at arbitrary orientations relative to the crystal axes. Since usually none of the rotation axes are either parallel or orthogonal to the crystal c-axis, modulations of unequal amplitudes are expected.

In Fig. (6.7) the modulation frequencies as a function of the rotating electric field are shown for two orthogonal planes, denoted by x-y (Fig. (6.7)(a) and (b)) and by y-z (Fig. (6.7)(c) and (d)). The absolute magnitude of the dipole moments, represented by asterisks were again determined by scaling the modulation to the values measured for fixed orientations using contacting electrodes. The exact angular positions for these values were given by the crystal shape. Fig. (6.7)(a) and (c) show the modulation for the optical transition at 605.813 nm. From the two modulation curves the Stark coefficients were determined as 112.1 kHz/(Vcm$^{-1}$) and 111.1 kHz/(Vcm$^{-1}$), respectively, yielding an averaged $\zeta_S \simeq 111.6$ kHz/(Vcm$^{-1}$). The fact that the two sets should yield equal magnitudes offers a way to verify the accuracy of the measurement which appears to be better than 5%. The angle $\xi$, enclosed by the two dipole moments was found to be $\xi$=24.8°. The same experiment

was performed in the optical transition at 607.770 nm shown in Fig. (6.7)(b) and (d) yielding Stark coefficients 94.2 kHz/(Vcm$^{-1}$) and 91.6 kHz/(Vcm$^{-1}$), resulting in $\zeta_S$ = 92.9 kHz/(Vcm$^{-1}$) and $\xi$=11.8°.

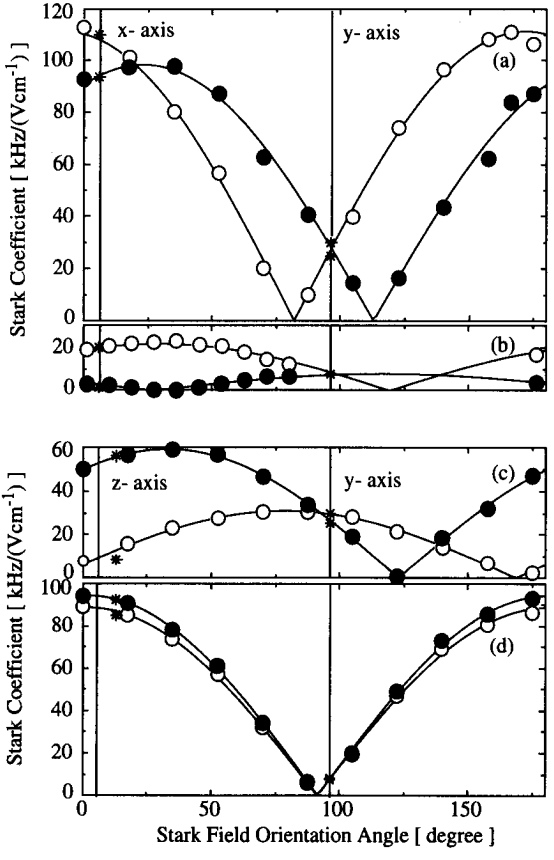


**Figure 6.7:** Stark coefficients for site I ((a) and (c)) and site II ((b) and (d)) in $Pr^{3+}$:$Y_2SiO_5$. Fig. (6.7) (a) and (b) correspond to the modulation of two inequivalent sites (open circles and filled circles) as a function of the rotation of the electric field orientation along an arbitrarily chosen x-y plane. Fig. (6.7) (c) and (d) are measured in the y-z plane, orthogonal to the x-y plane. As in Fig. (6.6), the asterisks represent additional measurements performed using contacting electrodes along three independent directions. Fitting of the data yields the components $(\delta\mu_x, \delta\mu_y, \delta\mu_z)/|E_S|$, i.e. the magnitude of $\zeta_S$, and the angle $\xi$ enclosed by the dipole moments of the inequivalent sites.

Summarizing, it can be concluded that for the first time complicated modulations in SMPE spectroscopy have been observed. The modulations have been interpreted in terms of different Stark shifts of static dipole moments at inequivalent sites, providing all the information about orientation and magnitude. For two different crystalline hosts the static dipole moments and orientations have been de-

termined with high precision. It is worth noticing that, once the dipole moments are fixed, SMPE allows for the sensitive measurement of any static electric field distribution.

## 6.3 Stark effect in the frequency domain

PSHB in RE doped crystals in combination with absorption [117] or holographic [51, 120] detection techniques had already been exploited in the past for the determination of electric dipole moments. The limitation given by the broad laser linewidth made the method less suited than SMPE, since large fields needed to be applied in order to observe the splitting. Inhomogeneities of the field made the signal quickly drop to zero, something wanted for an optical storage device [3], but disturbing when dipole moments need to be determined. Furthermore, the hologram diffraction efficiency is known to be proportional to the square of the amplitude. Thus when a splitting into four components is observed, the intensity of the holographic signal is expected to drop to 1/16, making the detection more difficult. It would therefore appear that PSHB may not be a valid alternative to the earlier presented SMPE technique.

However, there are different factors which can favor the use of PSHB for a determination of Stark splittings in the the frequency domain. If the persistence of the spectral holes is very strong, the echo amplitude will never totally disappear due to a superposition with an accumulated photon echo signal. This will lead to non-sinusoidal modulation curves which reduces the accuracy and quality of the SMPE measurements. Another advantage of PSHB over SMPE is that in the case of SMPE the number of modulation frequencies scales with the square of the number of inequivalent dipole moments, in contrast to hole burning where the relation is linear. Thus if the number of components is large, SMPE may fail in determining all the separate frequency components. For some systems, the observation of hole splittings of persistent holes in an electric field may therefore appear as a powerful alternative. The main problem which needs to be overcome is the stability of the light source. Using the actively stabilized laser system presented in Chapter 4 this problem is

resolved in great part. Here, results of measurements in an $Eu^{3+}:Y_2SiO_5$ 0.1 at.% sample are presented. The experiments were carried out in the two optically allowed transitions at 579.879 nm and 580.049 nm [92]. The setup corresponds to the one described in Chapter 5. Voltages where applied to the sample using contacting metal electrodes in the same vein as described in the previous Section. Spectral holes were burned with 30 $\mu W/cm^2$ to avoid power broadening. The exposure times ranged from 20 ms - 3 s. The readout power was attenuated by approximately two orders of magnitude to avoid further burning.

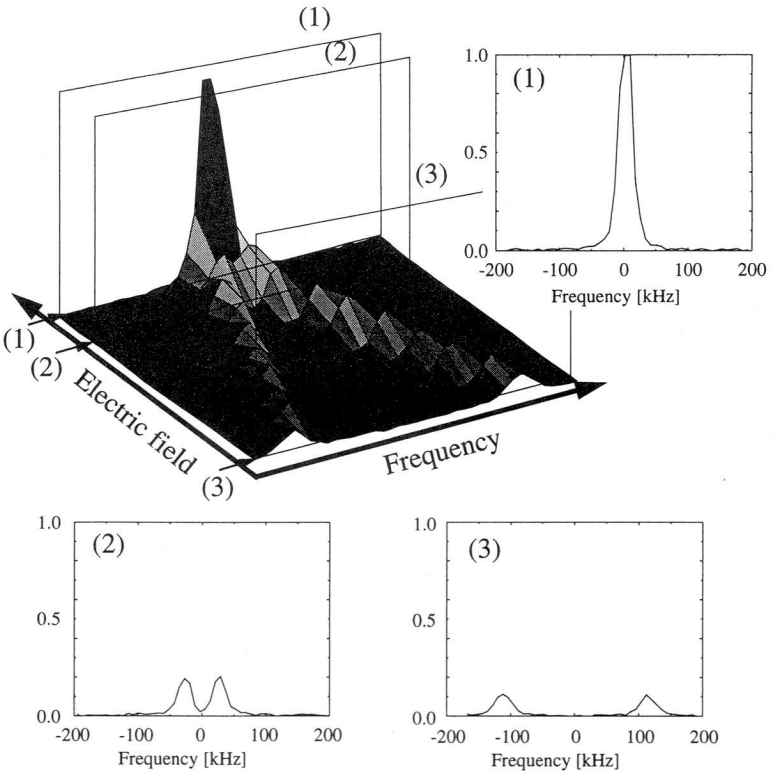


**Figure 6.8:** Two-dimensional scans over a spectral hologram. The insets show three frequency scans at constant electric fields. The hologram intensity drops to approximately a fourth, if the spectral hole splits into two components. At higher fields the amplitude further decreases and the linewidth broadens slightly.

In Fig. (6.8) a two dimensional scan over a spectral hologram of $Eu^{3+}$ in site I is shown. The insets show frequency scans at constant fields for E=0 V $cm^{-1}$ (1), E=1.2 V $cm^{-1}$ (2), and E=3.6 V $cm^{-1}$ (3). The hologram linewidth in these experiments was in the order of 20-30 kHz. Due to the high frequency resolution, only very small fields were needed in order to observe the hole splitting. Note explicitly the amplitude difference of the signal shown in (1) compared to inset (2). It can be clearly seen that the signal intensity drops to a fourth as expected for a single splitting. For an ideally aligned electric field and perfectly oriented dipole moments, the amplitude should remain constant also at higher voltages. However, due to small inhomogeneities, the amplitude decreases further and broadening is observed (Fig. (6.8) (2) and (3)) . This effect is similar to the line broadening of spectral holograms observed in dye doped polymers [112]. Implications of field inhomogeneities on the SMPE signals will be discussed in the next Section.

The number of expected dipole moments and their possible orientations is equal to the case of $Pr^{3+}$ in $Y_2SiO_5$, studied in the previous Section. Here, in contrast to the SMPE experiments, the measurements were only carried out for three orthogonal orientations. This in principle yields all the information of the orientation and magnitude of the different dipole moments. However, due to the the smaller amount of experimental data points, the error bars are distinctively bigger. In Fig. (6.9) contour plots of persistent spectral holes splittings in $Eu^{3+}$ site I are presented for two electric field orientations. Fig. (6.9) (a) shows a contour plot of a holographic signal along an arbitrary direction denoted as z. In (b) the splitting of a hole detected in transmission for an orthogonal direction x is reproduced. Note that in the transmission signal the generally expected four frequency components can be observed. The experimentally determined parameters yielded $\zeta_S$ =35 $\pm$5 kHz/(Vcm$^{-1}$) and $\xi = 17 \pm 8°$ for site I. The corresponding measurements in site II gave $\zeta_S$ =17 $\pm$5kHz/(Vcm$^{-1}$) and $\xi = 0 \pm 5°$, The magnitude of the dipole moments in site II is distinctively smaller than the ones in site I. As an overall tendency for both crystalline hosts studied here, the $Eu^{3+}$ dipole moments were found to be clearly smaller than the ones of $Pr^{3+}$.

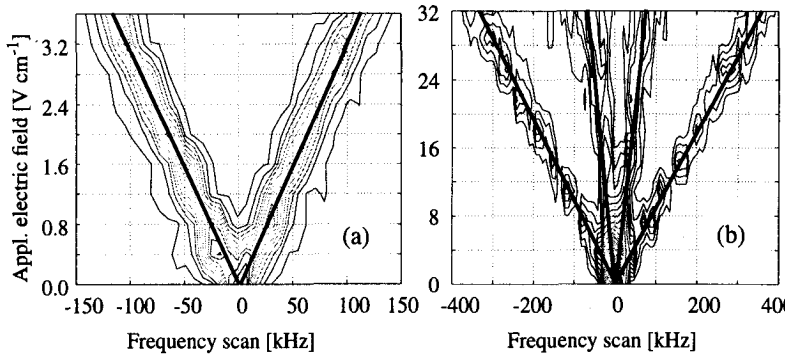


**Figure 6.9:** Measurements of the splitting of spectral holes in an externally applied electric field. Shown are two out of three measurements performed along orthogonal directions in $Eu^{3+}$: $Y_2SiO_5$ in site I. In (a) a contour plot of the holographic diffraction efficiency is presented for an electric field orientation along a crystal direction denoted as z. (b) depicts the transmission signal for an orthogonal crystal direction (x). In (a) only two frequency components are visible with a magnitude of 30 kHz/(Vcm$^{-1}$). In (b) four components, as generally expected can be clearly resolved. Evaluation of all components leads to a Stark coefficient of $35 \pm 5$ kHz/(Vcm$^{-1}$) and an angle $\xi = 17 \pm 8°$. For site II the corresponding measurements resulted in $17 \pm 5$ kHz/(Vcm$^{-1}$) and $\xi = 0 \pm 5°$.

In conclusion, it can be stated that hole splittings with fields of less than 5 Vcm$^{-1}$ have been observed in $Eu^{3+}Y_2SiO_5$. This has allowed for an accurate determination of dipole moment differences by an alternative method with a comparable resolution than using SMPE.

## 6.4 Deterministic perturbation of photon echoes

As discussed previously, photon echoes can be viewed as a result of delicate balancing between the phase shifts of each ion during the dephasing and the rephasing period, each of length $t = t_{12}$. Consequently, any perturbation that shifts the transition frequency $\omega(t)$ by the order of $1/t_{12}$ can easily affect the echo intensity $I$ and, if the perturbation is inhomogeneous to all the ions, it will experience attenuation. This strong sensitivity of the echo to small perturbations was used in many experiments to investigate the stochastic interaction of the RE ion with its surrounding and was

even employed as a tool for a novel type of spectroscopy [128]. In these experiments, the resonance frequency was shifted by the optical excitation of neighboring guest ions, which allowed for an indirect measurement of the absorption spectrum of the neighboring ion. Recently it was demonstrated that strongly attenuated echo signals can be partially recovered by carefully adjusting the perturbation and excitation times, thus partly cancelling the effect of perturbation, no matter how strong it is [106]. This was addressed as "dephasing-rephasing balancing". However, only partial recovery could be obtained since stochastic perturbations were considered. The recovery is expected to be much more pronounced if a deterministic perturbation is employed. In this case the perturbation can be applied in a controlled fashion, and the energy shift of the ions is predictable. The recovery of such a signal will be referred to as Stark echo and is discussed in the next Subsection.

### 6.4.1 Stark echoes

The time dependence of the eigenfrequency $\omega_j(t)$ of the $j$th ion is again considered to be describable through Eq. (6.2). In contrast to the preceding Sections, inhomogeneously distributed $\Omega_j$'s are considered here. This inhomogeneity can either originate from a change in the orientation or magnitude of the dipole moments or the electric field. Thus, by switching on an external field another kind of dephasing starts to take place related to this inhomogeneity [129]. This results in a second kind of "free induction decay". The discussion presented here is restricted to a single Stark splitting. An extension to the more general case considered in the previous Sections is trivial, since Eq. (6.4) is linear. The Stark field is assumed to be inhomogeneously varying over the whole sample volume both in magnitude and in angle. For simplicity, the variation is taken to be given by two independent Gaussian distributions of the amplitude $|\mathbf{E}_S|$ and angle $\theta$, with mean values $E_{S0}$ and $\theta_{S0}$ and variances $\sigma_E$ and $\sigma_\theta$, respectively. For a fixed $t_{12}$ this implies, that in order to calculate Eq. (3.14), the average over the normalized polarization $\mathbf{P_0}$ needs to be carried out. This requires a spatial average over all possible orientations of the dipole moments $\delta\boldsymbol{\mu}$ and the electric field amplitudes $\mathbf{E}_S$. For this specific type of distribution and for a single

pseudo Stark splitting, $|\mathbf{P_0}|$ can be written as

$$|\mathbf{P_0}| \sim \int \mathrm{d}|\mathbf{E_S}| \int \mathrm{d}\theta_S \cos\left(|\mathbf{E_S}||\delta\boldsymbol{\mu}|/\hbar \cos(\theta_S)\right) D(|\mathbf{E_S}|, \theta_S) \ , \tag{6.5}$$

with

$$D(|\mathbf{E_S}|, \theta_S) = \exp\left(-\left(\frac{\theta_S - \theta_{S0}}{\sqrt{2}\sigma_\theta}\right)^2 - \left(\frac{|\mathbf{E_S}| - E_{S0}}{\sqrt{2}\sigma_E}\right)^2\right) .$$

For the averaging, $\sigma_\theta \ll 1$ is assumed since highly diluted and thus almost perfect single crystals are considered. Of additional help is that since the process is non-linear in the intensity, the probed volume becomes very small. Thus, Eq. (6.5) can be integrated and the normalized echo intensity as a function of the Stark pulse width $\tau_{S1}$ becomes

$$I(\tau_{S1}) = \frac{1}{2}\left[1 + \cos(2\ \Omega_{S0}\tau_{S1})\right] e^{-(\sigma_S \tau_{S1})^2}, \tag{6.6}$$

where

$$\sigma_S = \frac{|\delta\mu|}{\hbar}\sqrt{\sigma_E^2 \cos^2(\theta_{S0}) + \sigma_\theta^2 E_{S0}^2 \sin^2(\theta_{S0})} \ , \tag{6.7}$$

and $\Omega_{S0} \equiv |\delta\mu| E_{S0} \cos(\theta_{S0})$ corresponds to the mean oscillation frequency. Eq. (6.6) describes a sinusoidal modulation with a Gaussian damping envelope. The phase evolution of such an echo is depicted in Fig. (6.10)(a). Analogously to Fig. (6.1)(b), at ($t = 2t_{12}$), rephasing occurs at two positions in the phase space. However, due the inhomogeneity, these positions are smeared out leading to an attenuation of the echo intensity.

Applying Stark pulses within the dephasing period will always lead to a decrease of the echo signal. However, the echo can be recovered by additionally applying a Stark pulse during the rephasing period. In order to obtain best recovery, which for a reversible system corresponds to full recovery, the dephasing-rephasing balancing condition

$$\int_0^{t_{12}} E_S(t)\mathrm{d}t = \int_{t_{12}}^{2t_{12}} E_S(t)\mathrm{d}t \tag{6.8}$$

needs to be fulfilled. Signals obtained under those conditions will be referred to as Stark echoes.

Stark echoes can be interpreted as *an echo in the echo,* or a second kind of rephasing process and are observed by leaving $\tau_{S1}$ constant and plotting the echo intensity as a function of the second electric-field pulse width $\tau_{S2}$. This is depicted in Fig. (6.10)(b), where the recovery is observed at a single point in the phase space.

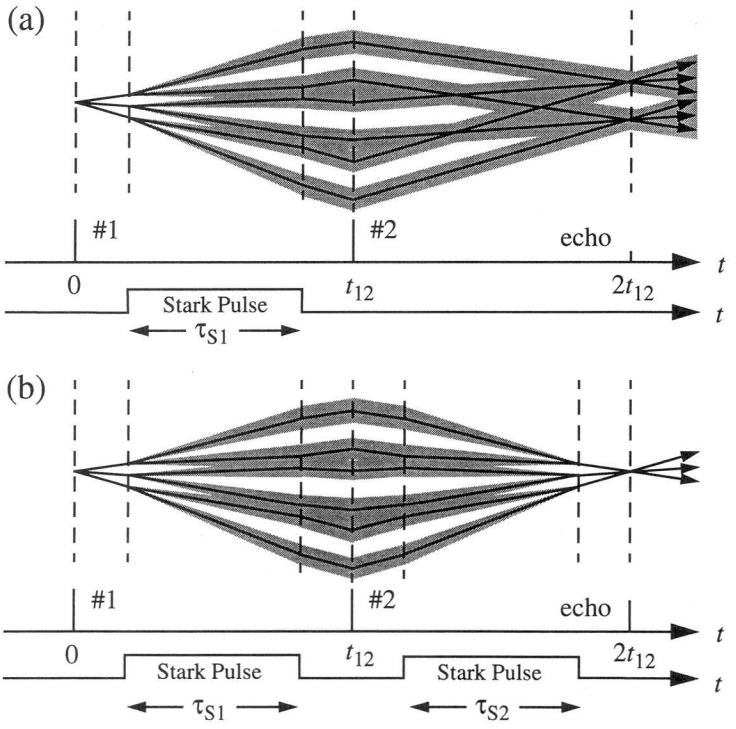


**Figure 6.10:** Timing sequence of a 2PPE with a Stark pulse applied during dephasing period (a). In (b) a perfectly recovered Stark modulated photon echo is depicted. Such a recovery can be achieved if the areas of the two electric field pulses are properly adjusted. Details can be found in the text.

The Stark echo can also be described by Eq. (6.6) after replacing $\tau_{S1}$ by $(\tau_{S1} - \tau_{S2})$. From Eq. (6.6) one sees that, in order to obtain very sharp decay and recovery curves, large $\sigma_S$ is desirable. This is in clear contrast to the ordinary Stark modulation spectroscopy presented above, where a smaller $\sigma_S$ is favorable for an accurate determination of $\Omega_{S0}$. It is worth mentioning that the idea of gradient fields is also exploited in magnetic resonance imaging (MRI), where a magnetic field gradient methods is used to increase the spatial resolution [81].

### 6.4.2 Results

The experimental setup corresponds to the one drawn in Fig. (6.3). Detailed experimental parameters corresponding to the individual experiment are given in the Figures. In Fig. (6.11), an experimentally measured Stark echo is shown. The echo intensity is plotted for variable pulse length $\tau_{S2}$ of the rectangular electric field pulse applied during the rephasing period. Results are presented with or without a first pulse of fixed length ($\tau_{S1} = 4$ $\mu$s), applied during the dephasing interval. As a function of $\tau_{S2}$, a dramatic recovery of the echo signal can be observed (b,d). The electric field values used for this experiment were $E_{S1} = 640$ Vcm$^{-1}$ for pulse I and $E_{S2} = 560$ Vcm$^{-1}$ for pulse II, respectively. Thus, maximal recovery is expected at $\tau_{S2} = 4.6$ $\mu$s, for which the dephasing-rephasing balancing condition $E_{S1}\tau_{S1} = E_{S2}\tau_{S2}$ is satisfied. The temporal width of the Stark echo is an order shorter than the one of the optical excitation pulse widths, showing that the width is solely determined by $\sigma_S$ (Eq. (6.7)). It can be further shortened by applying higher electric fields. Theoretically, there is no intrinsic lowest limit to the temporal extension of Stark echoes. In Fig. (6.11) (d) the total recovery is shown for an configuration where a single modulation frequency is observed. As predicted by Eq. (6.6), the envelope can be fitted by a Gaussian. In principle echo recovery can also be obtained using a single voltage pulse spreading over the dephasing and rephasing period and fulfilling Eq. (6.1). However, effectively the pulses always have a finite width which disables one to accurately define the limits of the dephasing and rephasing periods and the recovery signal has to be expressed by a convolution with the second pulse. Experimental observations of this effect are shown in Fig. (6.12).

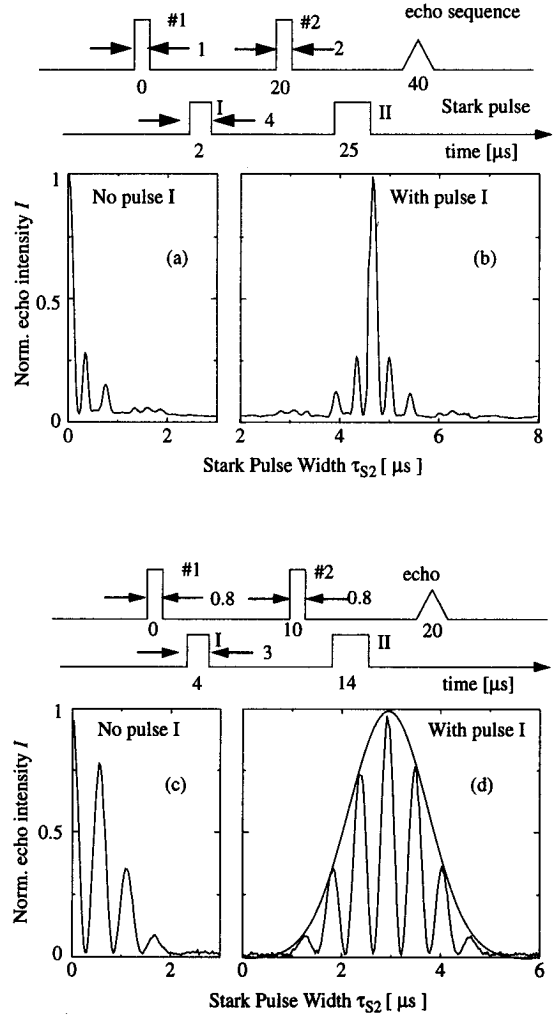


**Figure 6.11:** Decay and recovery of the photon echo for the $^7F_0 - {}^5D_0$ transition of $Eu^{3+}$ ((a) and (b)) and the $^3H_4 - {}^1D_2$ transition of $Pr^{3+}$ in $Y_2SiO_5$ ((c) and (d)). In the case of $Pr^{3+}$ the electric field was applied along a direction such that a single modulation curve can be observed, corresponding to the description of Eq. (6.6). In all cases the Stark pulses were chosen to be rectangular. In (a,c), pulse I is absent and the width of pulse II is varied. In (b,d), pulse I is present and the width of pulse II is varied. It can be seen that if the dephasing-rephasing balancing condition $E_{S1}\tau_{S1} = E_{S2}\tau_{S2}$ is fulfilled, total recovery is observed. For $Pr^{3+}$ a fit of a Gaussian envelope to the decay is shown (d).

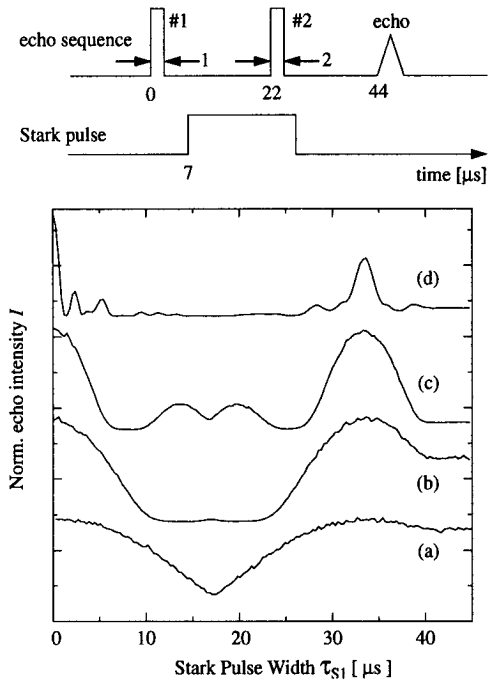


**Figure 6.12:** Echo intensity vs. Stark pulse width for four different Stark field strengths; $E_S$ = (a) 4, (b) 8, (c) 16 and (d) 80 $Vcm^{-1}$, for the $^7F_0 - {}^5D_0$ transition of $Eu^{3+}$ in $Y_2SiO_5$. As can be seen from (d), the recovery signal has a smaller amplitude than the free induction part of the Stark echo, the reason being that the finite width of the pulse disables one to accurately define the limits of the dephasing and rephasing periods. This leads to a convolution of the ideal Stark pulse with the temporal width of the second excitation pulse.

The only condition which needs to be fulfilled in order to obtain full recovery of the echo signal is given by Eq. (6.8). This implies that the echo amplitude is purely sensitive to the total area and not to the specific pulse profile of the electric field pulses. To experimentally verify this, Stark pulses of different shapes were applied during the dephasing period and/or the rephasing period. Total recovery was always observed when the dephasing-rephasing balancing condition was satisfied, meaning that this system is functioning as a pulse-area comparator as demonstrated in Fig. (6.13). Here, Pulse I in the dephasing period is an arbitrary-shaped pulse whose area is to be measured. Pulse II in the rephasing period is a rectangular reference pulse with known amplitude. The Stark echo as a function of $\tau_{S2}$ will indicate accurately the area of Pulse I taking into account the polarity of the voltage. As shown in Fig. (6.13), the Stark echo was observed when the two pulse areas exactly matched. Numerical integration showed that the two areas are the same within the error of 2%, which is within the experimental accuracy.

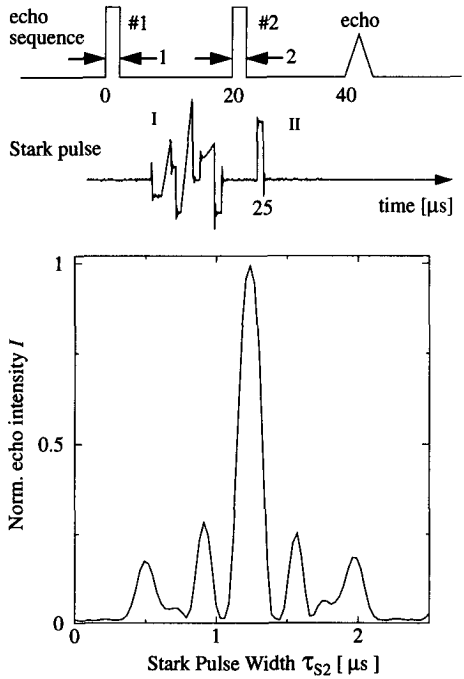


**Figure 6.13:** Pulse-area comparator by dephasing-rephasing balancing. Arbitrary-shaped Stark Pulse I is applied in the dephasing period. Shown is a measurement which was performed in the $^7F_0 - ^5D_0$ transition of $Eu^{3+}$ in $Y_2SiO_5$ . The total areas of the pulses applied within the two time periods are identical to within 2%, corresponding to the error bar of the experiment.

In summary, it can be concluded that the influence of a deterministic perturbation the echo intensity has been investigated. Within the accuracy of the measurements of 1-2%, the application of an electric field was found to lead to fully reversible frequency shifts. This effect could be described as an echo in the echo and was intitulated Stark echo. This phenomenon is important as a new type of "echo" that originates from the inhomogeneity of the external electric field. Finally, it was shown that the width of the Stark echo is not given by the lifetime or anything like that but rather by the total Stark shift.

It is worth remembering that a total recovery of the Stark echo is only expected in cases of fully reversible interactions. Thus, reversible frequency shifts appear to be dominant for the system and parameters described here. Nevertheless, irreversible interactions such as induced dipolar fluctuations can in general occur. They will show up in a change of the transition frequency $\omega_0(t)$ (defined through Eq. (6.2))

and lead to a stochastic contribution. Analyzing PSHB in glasses at very low temperatures (50 mK), Maier et al. noted an additional broadening of the linewidth upon application of a static electric field [130]. Relaxation back to the equilibrium linewidth was observed to occur only slowly after the electric field was switched off. The phenomenon was explained in terms of stochastically distributed TLS'es whose flipping rates were affected by the external field. Similarly, Stark echoes may be used to study configurational changes occuring on time scales much shorter than the ones accessible to PSHB. The proposed technique is similar to an ordinary $T_2$ measurement, where the echo peak is plotted as a function of the optical pulse separation. Here, the optical pulses are kept constant. The electric field pulse applied during the dephasing period is kept at a fixed length $\tau_{S1}$ while the rephasing pulse width $\tau_{S2}$ is scanned. Plotting the Stark echo intensity as a function of $\tau_{S1}$ should yield a measure of the amount of irreversible interaction. However, up to now such configurational changes could not be observed for any of the studied systems. It appears that glassy matrices, maintained at temperatures below 1 Kelvin may be better candidates for their possible occurrence.

## 6.5 Conclusions

In this Chapter the behavior of RE ion doped crystals upon application of electric fields has been investigated. Using simple group theoretical considerations it was shown that the number of all possible induced dipole moment differences can be determined. It has been demonstrated that different techniques such Stark modulated photon echoes or high resolution persistent hole burning allow for the accurate measurements of the magnitude as well as the orientations of the induced dipole moment differences of the RE ions. Experimental results of $Eu^{3+}$ and $Pr^{3+}$ both doped in $YAlO_3$ and $Y_2SiO_5$ have been presented. As shown in the next Chapter, the knowledge of these magnitudes is crucial for the predictions and the understanding of ion interactions in solids.

The treatment of the electric field was based on the assumption that the application of a deterministic perturbation leads to fully reversible and deterministic shifts

of the respective transition frequencies. Here, it was verified experimentally that by properly adjusting the electric field pulse durations applied during the rephasing and dephasing periods, full recovery of the echo is observed. This novel type of rephasing phenomenon was referred to as Stark echo. Finally, a method was proposed which may allow for the measurement of electric field induced configurational changes by means of Stark echoes on much faster time scales than the ones accessible to hole burning techniques.

# 7. Attenuation of photon echoes by dynamical interactions

The photon-echo attenuation by various dynamical processes is studied. The experimental investigations concentrate on a $Pr^{3+}$:$Eu^{3+}$:$Nd^{3+}$co-doped $Y_2SiO_5$ crystal at low temperatures. Two-pulse photon-echo intensities are measured as a function of the pulse intensities when either the $Pr^{3+}$ or the $Eu^{3+}$ ions are excited. For the quantitative interpretation primarily excitation-induced frequency shifts (EFS) by diagonal and off-diagonal interactions are considered. It is shown that for the systems under consideration EFS are dominated by diagonal interactions. The observed echo attenuation by EFS is compared with the predictions calculated from independent Stark-field measurements and reasonable agreement is obtained. Finally, the broadening by spin-ion interactions, by non-equilibrium phonons and the dependence of the echo attenuation on the frequency position in the inhomogeneously broadened band are analyzed.

## 7.1 Introduction

Photon echoes have been extensively employed to study quantum coherence and mechanisms which lead to a destruction of the coherence by dephasing [23, 25, 106, 107, 127, 131–135]. It has become clear that the dephasing depends very sensitively on the dynamics in the environment of the photo-active species, so that photon echoes represent a tool for the investigation of extremely small changes in the environmental conditions. Dephasing is closely related to line broadening, so that the investigation of echo attenuation and of line broadening are complementary disciplines, yielding similar information on different time scales [23, 136]. The analyses of photon echoes in solids have shown that several dynamical processes can give rise to an attenuation of the echoes. Such attenuation has been investigated for photo-active species diluted to low concentrations in crystals of high quality at low temperatures. These investigations have been essential for the understanding of the different attenuation mechanisms and as a result progressively narrower linewidths have been observed during the last years.

When studying line broadening mechanisms, several dynamical processes have to be considered in the analyses of photon-echo attenuation. Naturally, these processes simultaneously affect the excitation coherence so that it is not easy to unscramble the various terms contributing to the echo attenuation. Based on Eq. (2.1), Eq. (2.6) and Eq. (3.21), the homogeneously broadened line can be decomposed as

$$\Gamma = \Gamma_{\mathrm{LT}} + \Gamma_{\mathrm{EQP}} + \Gamma_{\mathrm{TLS}} + \Gamma_{\mathrm{SI}} + \Gamma_{\mathrm{EFS}} + \Gamma_{\mathrm{NQP}} \; . \tag{7.1}$$

Since the individual broadening mechanisms do not necessarily lead to an exponential attenuation of the echo intensity, expression (7.1) is only a schematic representation of the broadening. Here, $\Gamma_{\mathrm{LT}}$ represents the lifetime limited value, $\Gamma_{\mathrm{EQP}}$ stands for contributions from equilibrium phonons and $\Gamma_{\mathrm{TLS}}$ takes into account effects due to lattice two-level systems (TLS). $\Gamma_{\mathrm{SI}}$ results from the spin-ion interaction (SI) between the nuclear spins of the RE and the host ions. Finally $\Gamma_{\mathrm{EFS}}$ denotes the excitation induced frequency shifts (EFS) and $\Gamma_{\mathrm{NQP}}$ takes into account the broadening by non-equilibrium phonons (NQP). These different broadening mechanisms have been studied over the last three decades. In this Chapter, they are discussed

independently, beginning with an overview.

The first term in Eq. (7.1), $\Gamma_{\mathrm{LT}}$, covers contributions from radiative and non-radiative decays and establishes the ultimate limit of $\Gamma$. It can be evaluated in different ways, one being the measurement of fluorescence decays. At cryogenic temperatures, the lifetime of RE ions in crystals ranges from $\mu$s up to ms. An overview of RE ion spectroscopy data is given in Ref. [8].

$\Gamma_{\mathrm{EQP}}$ addresses the broadening by phonons at thermal equilibrium [28,137–139]; one- and two photon processes have to be taken into account. $\Gamma_{\mathrm{TLS}}$, referring to lattice two-level systems, is a weak effect in RE ion doped crystals and has only rarely been the subject in the analyses of these systems. However, for crystals grown under different conditions, Flinn et al. [140] observed a tremendous change of the extrapolated zero-intensity broadening and a change of the temperature dependence from a $T^7$-law to a linear behavior. The latter behavior is known for glassy systems [30] and has been interpreted in terms of the standard TLS model [32,134].

$\Gamma_{\mathrm{SI}}$ depends on the dynamics of the host spins which magnetically interact with the guest ions. This type of phenomenon was studied by Anderson and Weiss [141,142] and by Kubo [143,144] to describe the line shapes observed in paramagnetic resonance. Klauder and Anderson [74] initiated the notion of the aforementioned sudden-jump model which was studied in detail [145–150]. Optical evidence for spin-ion interactions was first given by Shelby et al. [117] in $Pr^{3+} : LaF_3$ and was confirmed by Monte Carlo simulations [24]. Weak permanent magnetic fields of the order of 100 Gauss were applied to slow down the spin dynamics which allowed the measurement of linewidths very close to the lifetime limit [21,42]. A particular case arises when the guest ion has a large enhanced magnetic dipole moment in the excited state. This leads to non-uniform lattice spin dynamics in the crystal, since the flipping of a lattice spin is frozen-in close to the guest ions. This effect has been discussed in terms of the "frozen core" model [151–153]. Consequently, the echo intensity decay is modified and can be described by $\ln(I/I_0) \sim -(4t_{12}/T_M)^x$ for short $t_{12}$ where $x = 2$ denotes the regular case and $x > 2$ indicates a frozen core effect [151–153].

The four first terms in Eq. (7.1) can be the attributed to properties of the

guest-host system and do not depend on the number of excited ions involved in the echo formation. This is different for $\Gamma_{\mathrm{EFS}}$ and $\Gamma_{\mathrm{NQP}}$. Excitation induced frequency shifts (EFS) in the optical regime have been proposed by Taylor and Hessler [148] for the interpretation of the concentration dependent dephasing reported by Liao and Hartmann [154]. Unambiguous experimental evidence of EFS in RE ion doped crystals was first given by Cone and Liu [107, 133] and Huang et al. [25]. Further experimental [36, 106, 135, 155, 156], and theoretical studies [73, 157, 158] have been devoted to EFS. The theoretical models were initially based on off-diagonal ion-ion interactions [38, 157, 159, 160]. It turned out that the averaging over the temporal realizations of the excitation dynamics and over spatial and energetic configurations is involved. Asadullin [73] applied a mean-field type of approach for the analysis of dephasing by EFS. Macfarlane and Shelby [127] observed a broadening in 2PPE depending on the frequency position in the inhomogeneous band and explained their observations in terms of off-diagonal or quasi-resonant interactions. These findings were analyzed in more detail by Root and Skinner [158] in terms of off-diagonal interactions. Later it was speculated that diagonal interactions may dominate in EFS [42]. Huang et al. [25], Mitsunaga et al. [135] and Altner et al. [128] applied a separate laser to independently induce a high excitation density and the 2PPE intensities were recorded as a function of this density. These experiments made clear that diagonal interactions can lead to a strong attenuation. However, it remained unclear whether diagonal or off-diagonal interactions dominate in pure 2PPE experiments.

Finally, the last term in Eq. (7.1), $\Gamma_{\mathrm{NQP}}$, accounts for non-equilibrium phonons (NQP) [161] which are generated by the decay of the electronic excitations. In a bichromatic experiment, Macfarlane and Meltzer [132] pumped an upper Stark level. An increased line broadening was observed which was interpreted in terms of NQP generated by the phonon assisted relaxation of the upper into the lower level. Kröll et al. observed a dephasing in a standard 2PPE experiment, which could not be explained in terms of EFS and the authors conjectured a broadening by NQP [162–164]. By a variation of the focal area, Bai and Kachru [131] clearly demonstrated that NQP play an important role in the dephasing for $Pr^{3+}$: $YAlO_3$.

In the present work, results of 2PPE attenuation in a codoped $Eu^{3+}$:$Pr^{3+}$:$Nd^{3+}$:$Y_2SiO_5$ crystal are presented. The characteristic behaviors of the

different broadening mechanisms are discussed, particularly concentrating on the EFS broadening by diagonal and off-diagonal interactions. The Chapter is structured as follows: In Section 7.2 the experimental setup and the experimental conditions are shortly described. In Section 7.3 broadening by various dynamical processes is discussed with emphasis on the echo attenuation by EFS. Closing remarks are given in Section 7.4.

## 7.2 Experimental setup

The experimental setup largely corresponds to the one presented in Section 6.2. The laser beam from a single-frequency tunable dye laser (CR 699-21) was chopped by two acousto-optic modulators (AOM1 and AOM2) (Matshusita EFLM 200) to generate excitation pulse with typical lengths of 0.7-1.5 $\mu$s. The AOM driver (Brimrose VFA 200-75-B1-F1.25-E) allowed for fast frequency shifting of up to 1 MHz/ns. Using an additional electro-optic modulator (EOM) (Leysop driven by a New Focus high voltage amplifier 3211) the pulse amplitudes could be independently controlled. Beams of powers up to 30 mW were focused by a 120 mm focal length lens onto the crystal resulting in a beam waist of approximately 45 $\mu$m.

The experiments were carried out on a $5 \times 5 \times 5$ mm$^3$ 0.1 $Eu^{3+}$: 0.01 $Pr^{3+}$: 0.01 $Nd^{3+}$ at. % co-doped $Y_2SiO_5$ crystal [128]. The pulse propagation direction was chosen close to one of the crystal axes and the light polarization was adjusted to the maximum absorption. The use of a multiply-doped crystal proved to be very useful because it allowed for the measurement of different broadening effects in one and the same system for different RE parameters. The laser wavelength was tuned either to the $^7F_0$-$^5D_0$ site I transition of $Eu^{3+}$ or to either site I or site II of the $^3H_4$-$^1D_2$ transition of $Pr^{3+}$, respectively [41, 42, 51]. To avoid persistent hole burning, the laser was repetitively scanned over a 400 MHz range in 250 ms. The echo signal, after passing through AOM3 was detected by a photo-multiplier (Hamamatsu 928) and recorded using boxcar integration. For each $t_{12}$, the residual background was additionally recorded. In this way the effect of hole burning and of slow baseline drifts could be eliminated. Averages were taken over 100 echoes at each

time delay. The pulse power was synchronously monitored in order to control power drifts. All experiments were carried out at a temperature of 1.7 K. A summary of results obtained in this work, along with data taken from the literature is given in Table 7.1.

## 7.3 Line-broadening mechanisms

In this Section, the broadening by the various dynamical processes as schematically presented in Eq. (7.1) is discussed. These processes are classified as follows: (i) the broadening limited by the lifetime, (ii) lattice vibrations treated as equilibrium and non-equilibrium phonons, and (iii) TLS, SI, and EFS mechanisms, discussed in terms of the sudden-jump model.

### 7.3.1 Lifetime limits, equilibrium phonons, and TLS

The $^7F_0$-$^5D_0$ transition of $Eu^{3+}$ in $Y_2SiO_5$ has been repeatedly investigated, the main objective being its very small lifetime limited broadening of $\Gamma_{LT} \simeq 80$ Hz in site I [92]. A homogeneous linewidth close to this limit, $\Gamma_h \simeq 105$ Hz [21], has been obtained. For the $^3H_4$-$^1D_2$ transition of $Pr^{3+}$ the lifetime limited linewidths are considerably larger but still in the sub kHz range, namely $\Gamma_{LT} \simeq 970$ Hz and 720 Hz for site I and site II, respectively [42, 51].

The line broadening by thermal phonons was measured for $Eu^{3+}$ in $Y_2SiO_5$ by Altner et al. [36]. A $T^7$-dependence was observed, which indicates that the broadening is governed by a Raman-type process. An onset of the broadening was recorded at temperatures $> 8$ K. Thus for temperatures of $T \simeq 1.7$ K used in the present work the broadening by equilibrium phonons can be disregarded for this transition.

Referring to the work of Flinn et al. mentioned above [140], the broadening extrapolated to zero temperature may change by two orders of magnitude depending on the technique applied for the crystal growth. It is thus not surprising that

| Parameters | $Eu^{3+}$ site I | $Pr^{3+}$ site I | $Pr^{3+}$ site II | |
|---|---|---|---|---|
| $\lambda_0$(vacuum) [nm] | 579.879 | 605.813 | 607.770 | Ref. [51] |
| $\Gamma_{LT} = 1/(2\pi T_1)$ [Hz] | 80 | 970 | 720 | Refs. [42,92] |
| $\Gamma_{inh}$ [GHz] | 2.5 | 7 | 3 | a) |
| $\Gamma_h(H = 0)$ [Hz] | 210 | | | b) |
| $\Gamma_h(H = 0)$ [Hz] | 195 | | | Ref. [21] c) |
| $\Gamma_h(H = 100$ G) [Hz] | 105 | | | Ref. [21] |
| $\Gamma_h(H = 0)$ [Hz] | | 2400 | 1050 | Ref. [42] d) |
| $\Gamma_h(H = 80$ G) [Hz] | | 1800 | 850 | Ref. [42] |
| $\Gamma_h(H = 0)$ [Hz] | 330 | 1650 | 1000 | a) |
| $\Gamma_h(H > 500$ G) [Hz] | | 1200 | 900 | a) |
| $\alpha$ [$cm^{-1}$] | 2.7 | 1.4 | 0.18 | a) |
| f' e) | $5.3 \times 10^{-8}$ | $7.7 \times 10^{-7}$ | $4.5 \times 10^{-8}$ | a) |
| $\mu$ [D] f) | $2.0 \times 10^{-3}$ | $7.5 \times 10^{-3}$ | $1.9 \times 10^{-3}$ | a) |
| $\zeta_S$ [kHz/(V $cm^{-1}$)] | 35 | 110 | 90 | g) |
| $\delta\mu$ [D] h) | $2.3 \times 10^{-2}$ | $7.3 \times 10^{-2}$ | $6.0 \times 10^{-2}$ | |

**Table 7.1:** Spectroscopic data measured in the present work and data taken from the literature for $Pr^{3+}$ and $Eu^{3+}$ in $Y_2SiO_5$ crystals. The units are given in rectangular brackets. The homogeneous linebroadening $\Gamma_h$ are the extrapolated values to zero-pulse strengths and depend on the applied magnetic field $H$. References are given in the last column together with information on the doping. Data for the absorption $\alpha$ and corresponding oscillator strengths $f'$ are given for the optical geometry chosen in this work.

Footnotes: a): 0.1 % $Eu^{3+}$: 0.01 % $Pr^{3+}$ 0.01 % $Nd^{3+}$; b): 0.1 at. % $Eu^{3+}$ c): 0.1 at. % $Eu^{3+}$ different crystal; d): 0.02 at. % $Pr^{3+}$ ; e): oscillator strengths along electro-magnetic field polarization. ; f):Eq. (7.26) with $\epsilon(\omega_0) = 1.8$ [165]; g): see Chapter 6.; h): See Eq. (7.27) using $\epsilon(0) = 7$.

the linewidth measured for crystals grown under nominally identical conditions may also significantly differ from each other because the crystals are not identical. A minor change in the crystal quality may lead to a measurable change in the width. In Fig. (7.1) the linewidths are shown for $Eu^{3+}$ site I diluted in two $Y_2SiO_5$ crys-

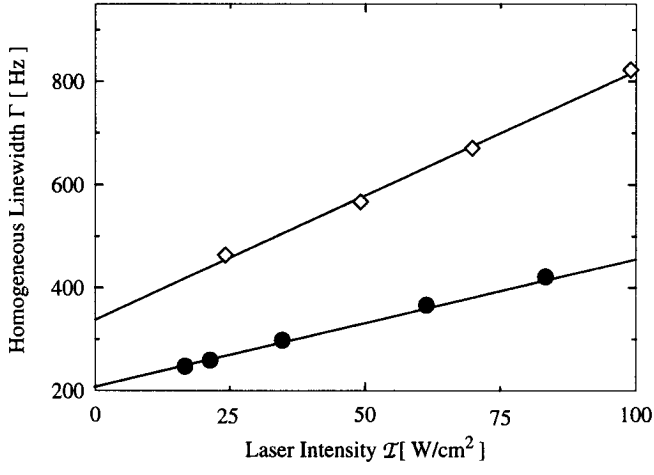


**Figure 7.1:** Linewidth of the $Eu^{3+}$ site I transition in $Y_2SiO_5$ for two crystals grown by flame fusion. The diamonds and circles are for a multiply doped and a singly doped crystal, respectively. In both cases the concentration of the $Eu^{3+}$ ions is 0.1 at. %. Straight lines are linear fits to the data. Note the difference in the extrapolated zero-energy values.

tals. Both crystals were grown by the flame-fusion method for equal concentrations of $Eu^{3+}$ ions. Assuming a linear dependence on the pulse energy, the extrapolated zero-energy linewidths are 210 and 330 Hz. The smaller of the two values is consistent with the 195 Hz recorded without magnetic field by Equall et al. [21]. Inspired by the measurements of Flinn et al. [140] and assuming a gradual change from a crystalline towards a glassy type behavior with increasing disorder, the differences in the linewidth are attributed to the TLS dynamics. This argument is supported by the following reasoning. The differences of some hundreds of Hz between the broadenings of different crystals are small, if compared with the inhomogeneous broadening on scales larger by six orders of magnitude. The latter broadening also results from lattice imperfections. Only a marginal part of these imperfections have

to undergo dynamics so that fluctuations of the order of kHz arise in the transition frequency. Thus, TLS contributions are believed to be a possible reason for some of the differences between broadening data of the present study and of that found in the literature. Concerning the temperature dependence, a linear increase is expected for $\Gamma_{\mathrm{TLS}}$ according to the standard TLS model. Correspondingly, the overall temperature dependence would follow a superposition of the linear and the $T^7$-law. Such a superposition is difficult to be traced from experimental data, because the $T^7$-law is only approximate and especially because the broadening by TLS is expected to be small and may thus be masked by stronger effects, as discussed below.

### 7.3.2 Spin-ion interactions

Spin-ion interactions have been analyzed in terms of the sudden-jump model which was initiated by Klauder and Anderson [74] and was extended by Hu and Hartmann [149] and by Hu and Walker [150]. In this model, the ions involved in the echo process interact magnetically with randomly flipping host spins. These interactions lead to fluctuations of the transition frequency and correspondingly to a dephasing.

According to Eq. (27) of Ref. [150] the 2PPE intensities are

$$-\ln\left(\frac{I}{I_0}\right)_{\mathrm{SI}} = c_{\mathrm{SI}}\ \exp(-x) \int_0^x \tilde{I}_0(\tilde{\xi}(x-x'))x' \left[\tilde{I}_0(x') + \tilde{I}_1(x')\right] \mathrm{d}x', \tag{7.2}$$

where

$$\tilde{\xi} = \frac{k_1 - k_2}{k_1 + k_2} \ \text{ and } \ x = (k_1 + k_2)t_{12}\ . \tag{7.3}$$

$c_{\mathrm{SI}}$ is a constant and $\tilde{I}_j$ denotes the modified Bessel function of the first kind and of argument $j$. $k_1$ and $k_2$ in Eq. (7.3) are rates of the up- and down spin flips. In the high-temperature limit, $\tilde{\xi} = 0$, and one has for the asymptotic behavior

$$\ln\left(\frac{I}{I_0}\right)_{\mathrm{SI}} \sim \begin{cases} -t_{12}^2 & ,\ t_{12}/T_{\mathrm{m}} \ll 1 \\ -\sqrt{t_{12}} & ,\ t_{12}/T_{\mathrm{m}} \gg 1 \end{cases}, \tag{7.4}$$

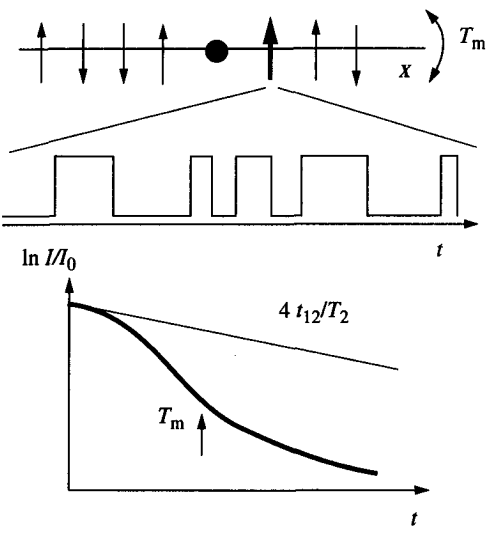


**Figure 7.2:** Schematic representation of the sudden-jump model. The arrows denote up and down states of the spins located for simplicity on a one-dimensional regular lattice. The flips occur randomly at a rate $T_m^{-1}$ for which a temporal realization is illustrated by the telegraphers function for a single spin. The ion, indicated by the dot, interacts with the spins, so that the the flips give rise to fluctuations in the ion's transition frequency. In the lower part the attenuation by spin-ion interaction is schematically depicted. The thin line represents the intrinsic broadening and the thick line includes the spin-ion interaction. A crossover is expected at $t_{12} = T_m$.

where $k_1 = k_2 = T_m^{-1}$, with $T_m$ denoting the spin flip time. From Eq. (7.4) it follows that with increasing $t_{12}$ the echo intensity undergoes a cross-over between the two asymptotic behaviors, as schematically shown in Fig. (7.2). In the next Subsection, use will be made of expression (7.2).

### 7.3.3 Excitation induced frequency shifts

One of the major attempts in this Chapter is to calculate the echo-attenuation by EFS from first principles. Based on off-diagonal interactions, similar calculations have already been undertaken by Root and Skinner [158]. However, their predicted line broadening was two orders of magnitude too small if compared with experimental observations by Macfarlane and Shelby [127]. The present analysis strongly indicates that for the systems studied here, EFS results predominantly from diagonal interactions. To discriminate between the two types of interactions, approximate expressions for the echo attenuation due to these interactions are first derived. An experiment is proposed which allows for the distinction between the two effects and

finally the broadening by EFS is calculated from first principles.

The here presented approach is based on a statistical description of the excitations and is motivated by the sudden-jump model introduced for the spin dynamics. The dynamics of excitation and de-excitation are treated as sudden events equivalent to the sudden spin flips. In this picture the sudden-jump and EFS model differ only by the nature of interaction and by the temporal realization of the dynamics. The approach is therefore semi-classical in the sense that the ions are considered as a quantum two-level systems interacting with classical fields induced by spins and excitations.

### EFS by diagonal interactions

In Ref. [36], EFS was studied for the case where a high excitation density is induced by a stronger scrambler pulse. Here, this analysis is extended to the case where the high excitation density is generated by the two echo inducing pulses. Starting from the Hamiltonian given in Eq. (2.14), the time dependent electronic transition frequency $\omega_j(t)$ of the $j$th ion can be written as

$$\omega_j(t) = \omega_{0j} + \sum_k{}' D_{jk}\xi_k u_k(t) \;, \tag{7.5}$$

where the sum runs over all lattice sites, except $j$ (indicated by the apostrophe). $\omega_{0j}$ is the ions static transition frequency at site $j$. The $\omega_{0j}$ frequencies are assumed to be distributed according to the inhomogeneous broadening; spatial correlations of the site energies are not considered here [158]. $D_{jk}$ in Eq. (7.5) is the frequency shift induced by the excitation of the ion at a displacement $\mathbf{r}_{jk}$. The $\xi_k u_k(t)$ term is introduced to account for the randomness of ion positions and for the stochastic nature of the ion excitations.

$\xi_k$ is a variable indicating whether the $k$th site is occupied

$$\xi_k = \begin{cases} 1 & \text{, with probability} \quad p \\ 0 & \text{, with probability} \quad 1-p \end{cases} \;, \tag{7.6}$$

where $p$ denotes the probability of a lattice site to be occupied by a guest ion. $u(t)$ in Eq. (7.5) is considered to be a stochastic variable taking values 0 and 1, for the electronic ground and excited state of the ion, respectively. The state of the ion depends on the transition probability, the pulse energies, and the offset $\Delta$ between the laser and the transition frequency. As discussed in Appendix A, $w_1$ denotes the excitation probability right after the first pulse and $w_2$ the probability of changing state upon the second pulse. Taking into account that the pulse times are short if compared with the inter-pulse time $t_{12}$, the damping during the pulse periods can be disregarded. One thus can write

$$\text{Prob.}\,[u(t)=1] \simeq \begin{cases} w_1 e^{-\gamma_1 t} & , \; 0 < t < t_{12} \\ w_1\,(1-2w_2)\,e^{-\gamma_1 t} + w_2 e^{-\gamma_1 (t-t_{12})} & , \; t_{12} < t < 2t_{12} \end{cases} . \tag{7.7}$$

The probability for $u(t) = 0$ results from Prob.$[u = 0]$ = 1 - Prob.$[u = 1]$. $\gamma_1$ in Eq. (7.7) again denotes the inverse lifetime $\gamma_1 = 1/T_1$ of the excited state and is considered to be independent of the lattice site. $w_1$ and $w_2$ depend on the frequency offset $\Delta$ and the averages have to be taken over the inhomogeneous line shape. According to Appendix A for weak laser pulses

$$\langle w_{1,2} \rangle \simeq c\mathcal{T}_{1,2} \quad , \quad c = \frac{1}{4\sqrt{2\pi}\sigma_\nu} \, , \tag{7.8}$$

where $\sigma_\nu$ is the standard deviation of the inhomogeneously broadened band in units of Hz. $\mathcal{T}_{1,2}$ denote the pulse energies $\mathcal{T}_{1,2} = \chi_{1,2}^2 \tau_{1,2}$, with $\chi_{1,2}$ and $\tau_{1,2}$ being the Rabi frequencies and pulse times, respectively.

Using Eqs. (3.15) and (7.5) the accumulated phase of the $j$th ion thus becomes

$$\int_0^{t_{12}} \omega_j(t)dt - \int_{t_{12}}^{2t_{12}} \omega_j(t)dt = {\sum_k}' D_{jk}\xi_k\theta_k \, , \tag{7.9}$$

where

$$\theta_k = \int_0^{t_{12}} u_k(t)dt - \int_{t_{12}}^{2t_{12}} u_k(t)dt \, , \tag{7.10}$$

is a random variable through the stochastic nature of $u(t)$ and depends on the offset $\Delta_k$. Making use of Eq. (3.14), Eq. (7.9), and Eq. (7.10) one finds

$$P(t_{12}) = P_0 \left\langle \prod_k{}' \exp\left(iD_{jk}\xi_k\theta_k\right) \right\rangle_{\xi_k,\theta_k,\Omega_k,\Delta_k} , \tag{7.11}$$

where the average is taken over the site-occupations $\xi_k$, over the temporal realizations of $\theta_k$, over all angles $\Omega_k$, and over the distribution of each offset $\Delta_k$. Writing Eq. (7.11), the vectorial properties of the echo polarization are disregarded. If the $(\xi_k, \theta_k, \xi_k, \Omega_k, \Delta_k)$ are assumed to be independently distributed variables, the average and the product can be interchanged. Applying additionally Eq. (7.6), Eq. (7.11) can be re-written as

$$P(t_{12}) = P_0 \prod_k{}' \left( 1 - p\left[1 - \langle \exp\left(iD_{jk}\theta_k\right) \rangle_{\theta_k,\Omega_k,\Delta_k}\right]\right) . \tag{7.12}$$

Such an expression has been discussed by Mitsunaga et al. for the case of a scrambler pulse, and an analytic solution has been presented [135]. For small $p$ values, a condition clearly fulfilled in highly diluted RE ion crystals,

$$\begin{aligned} P(t_{12})/P_0 &= \exp\left\{\ln\left(\prod_k{}' 1 - p\left[1 - \langle \exp\left(iD_{jk}\theta_k\right) \rangle_{\theta_k,\Omega_k,\Delta_k}\right]\right)\right\} \\ &\simeq \exp\left\{-p\sum_k{}' \left[1 - \langle \exp\left(iD_{jk}\theta_k\right) \rangle_{\theta_k,\Omega_k,\Delta_k}\right]\right\} , \end{aligned} \tag{7.13}$$

keeping in mind that for $x \ll 1$, $\ln(1-x) \simeq -x$.

In the dipole-dipole approximation the ion-ion interaction is given by

$$D_{jk} = (r_0/|\mathbf{r}_{jk}|)^3 \kappa(\Omega_{jk}) D_0 \ , \ \text{with} \ \ D_0 = \eta(0)\frac{(\delta\mu)^2}{4\pi\epsilon_0\hbar r_0^3} , \tag{7.14}$$

where $D_0$ represents the interaction between two dipoles at a unit distance $r_0$. $\eta(\omega)$ in Eq. (7.14) stands for the dielectric correction which reads [166]

$$\eta(\omega) = \frac{1}{\epsilon(\omega)}\left(\frac{\epsilon(\omega)+2}{3}\right)^2 , \tag{7.15}$$

where $\epsilon(\omega)$ is the dielectric constant of the host medium at frequency $\omega$. $\kappa(\Omega_{jk})$ in Eq. (7.14) gives the angular dependence of the interaction, $\kappa(\Omega_{jk}) = (\widehat{\delta\mu}_j, \widehat{\delta\mu}_k) - 3(\widehat{r}_{jk}, \widehat{\delta\mu}_j)(\widehat{r}_{jk}, \widehat{\delta\mu}_k)$, where $\widehat{\delta\mu}$ and $\widehat{r}$ are unit vectors for the dipoles and the displacement, respectively and $\Omega$ denotes the set of angles defining the corresponding spatial orientations. In the continuum approximation [36], Eq. (7.13) reads

$$\begin{aligned} \ln|P(t_{12})/P_0| &\simeq -4\pi\rho_0 p \left\langle \int_0^\infty dr r^2 \left\{1 - \cos\left[D_0\kappa(\Delta)(r_0/r)^3\theta\right]\right\} \right\rangle_{\theta,\Omega,\Delta} \\ &= -C_1 \langle|\theta|\rangle_{\theta,\Delta} \ , \end{aligned} \tag{7.16}$$

where $\rho_0$ is the density of sites which can substitutionally be occupied by RE ions. Only the absolute of the polarization is considered here since according to Eq. (3.20), $I(t_{12}) \sim |\mathbf{P}(t_{12})|^2$. The constant $C_1$ is equal to $(2/3)\pi^2 r_0^3 \rho_0 p \langle|\kappa|\rangle_\Omega D_0$ where the dimensionless quantity $\langle|\kappa|\rangle_\Omega$ is of the order 1. For the particular case where all dipoles are parallel, $\langle|\kappa|\rangle_{\|} = 4/\sqrt{27}$, and when all dipoles are perpendicular with respect to the dipole at the origin, $\langle|\kappa|\rangle_\perp = 2/\pi$ [36].

The derivation of $\langle|\theta(t)|\rangle$ as a function of the excitation probabilities is given in Appendix B. Making use of Eqs. (7.16) and (B.9) one obtains for the echo intensity

$$\begin{aligned} \ln\left(\frac{I}{I_0}\right)_{\text{EFS-D}} \simeq -2C_1\gamma_1^{-1} \Big[ &\langle w_1 (1 - w_2)\rangle \left(1 - e^{-t_{12}\gamma_1}\right)^2 \\ &+ \langle w_2\rangle \left(1 - e^{-t_{12}\gamma_1}\right) \Big] \ , \end{aligned} \tag{7.17}$$

where the subscript EFS-D indicates EFS by diagonal interactions. For weak pulses this yields

$$\ln\left(\frac{I}{I_0}\right)_{\text{EFS-D}} \simeq -2cC_1\gamma_1^{-1} \left[\mathcal{T}_1 \left(1 - e^{-t_{12}\gamma_1}\right)^2 + \mathcal{T}_2 \left(1 - e^{-t_{12}\gamma_1}\right)\right] \ . \tag{7.18}$$

Writing for the echo intensity $\ln(I/I_0) = -4t_{12}/T_2$, the broadening $\Gamma$ in units of Hz is related to the dephasing time $T_2$ by $\Gamma = (1/\pi T_2)$. For $\gamma_1 t_{12} \ll 1$ and from

Eq. (7.18) the broadening is therefore

$$\Gamma_{\text{EFS-D}} \simeq \frac{1}{2\pi} C_1 \langle w_2 \rangle \simeq \frac{1}{2\pi} c C_1 \mathcal{T}_2 \,, \tag{7.19}$$

where the latter equality holds for weak pulse strengths. One thus finds that for short $t_{12}$ the broadening depends predominantly on the energy of the second pulse, in agreement with previous results [21,25,106,107,133,135]. This behavior is regarded as a signature of the broadening by EFS in 2PPE.

### EFS by off-diagonal interactions

EFS by off-diagonal interactions was studied by Root and Skinner [157,158] using a cumulant expansion technique. Inspired by the analysis of EFS by diagonal interactions, here, a slightly different method is applied. The treatment of the full problem is involved. The fully coupled system is therefore approximated by sums of independent ion-pair interactions. For each pair the frequency shifts are calculated independently from the diagonalization of a two-by-two problem. Making use of the treatment presented in Chapter 2 (Eq. (2.18)), the transition frequency of the $j$th ion then reads

$$\omega_j(t) \simeq \omega_{0j} + \sum_k{}' \xi_k \left(1 - u_k(t)\right) \sigma_{jk} \left[\sqrt{J_{jk}^2 + \left(\Delta_{jk}/2\right)^2} - |\Delta_{jk}/2|\right] \,, \tag{7.20}$$

where $\Delta_{jk} = \omega_{0j} - \omega_{0k}$ and $\sigma_{jk} = \text{sign}(\omega_{0j} - \omega_{0k})$. $\xi_k$ and $u_k(t)$ are defined as in Eq. (7.5). The term $(1 - u_k(t))$ indicates that the off-diagonal interaction arises when the $k$th ion is in the ground state. For $|J_{jk}/\Delta_{jk}| \ll 1$, the term in rectangular brackets in Eq. (7.20) equals $J_{jk}^2/|\Delta_{jk}|$, which corresponds to the perturbation calculation up to the second order applied to the full problem, since the first order term vanishes for an off-diagonal perturbation operator. As shall be shown below, for the here studied systems the condition $|J_{jk}/\Delta_{jk}| \ll 1$, is clearly fulfilled.

The calculation of expectation values is complicated because the averaging includes the conditional probabilities of site $j$ and $k$ excitations separated by the frequency $\Delta_{jk}$. To simplify the calculations, the frequency of site $j$ is assumed to coincide with the laser frequency. Further, the frequency $\Delta_{jk}$ is either fixed to a value

$|\Delta\omega_s|$ if a high excitation density is generated with a scrambler pulse shifted in frequency by $\Delta\omega_s$ or is restricted to the range $[-\Delta_{\max}, \Delta_{\max}]$ which corresponds to spectral width of laser excitation. $\Delta_{\max}$ is thus approximately $\Delta_{\max} \simeq \max\{\chi, \Delta_{\text{laser}}/2\}$ where $\chi$ and $\Delta_{\text{laser}}$ denote the Rabi frequency and the spectral width of some average pulse, given by the pulse-width limit or the laser jitter, respectively. The spectral density is considered to be constant within the range $[-\Delta_{\max}, \Delta_{\max}]$ because $\Delta_{\max}$ is much smaller than the inhomogeneous linewidth $\Gamma_{\text{inh}}$. Similarly to Eq. (7.12) and Eq. (7.13) one finds for the polarization

$$\ln|P(t_{12})/P_0| \simeq -p\sum_k{}' \left\{ 1 - \right.$$
$$\left. - \left\langle \cos\left[ -i\,\theta_k\,\sigma_{jk}\left( \sqrt{J_{jk}^2 + (\Delta_{jk}/2)^2} - |\Delta_{jk}/2| \right) \right] \right\rangle_{\theta_k, \Delta_{jk}} \right\}, \quad (7.21)$$

and $\theta_k$ is given by Eq. (7.10). The average is also taken over the distributions of the $\Delta_{jk}$. Furthermore,

$$J_{jk} = J_0 \kappa(\Omega_{jk})\,(r_0/|\boldsymbol{r}_{jk}|)^3 \quad , \quad J_0 = \eta(\omega_0)\frac{\mu^2}{4\pi\epsilon_0 r_0^3 \hbar}\,, \quad (7.22)$$

where $\mu$ denotes the transition dipole-moment and the dielectric correction $\eta(\omega_0)$ of Eq. (7.15) is given for the transition frequency $\omega_0$. Typical distances $r_{jk}$ for two ions absorbing within the same spectral width of $\sim \Delta\omega_{\max}$ are calculated below as a few 10 nm's. Using Eq. (7.22) and the parameters given in Table (7.1), one finds that $|J_{jk}/\Delta_{jk}| \sim 0.01$, thus motivating the use of Eq. (7.20). Approximate expressions of Eq. (7.21) are derived in Appendix C. From Eqs. (C.7) and (C.12) one obtains

$$\ln\left(\frac{I}{I_0}\right)_{\text{EFS-J}} \simeq \begin{cases} -2C_2\,\langle|\theta|\rangle & , \; t_{12}\Delta_{\max} \ll 1 \\ -2^{3/2}C_2 \dfrac{\left\langle|\sqrt{\theta}|\right\rangle}{\sqrt{\pi\Delta_{\max}}} & , \; t_{12}\Delta_{\max} \gg 1 \end{cases}, \quad (7.23)$$

where $C_2 = (2\pi^2/3)J_0 p r_0^3 \rho\,\langle|\kappa|\rangle$. For small $t_{12}\gamma_1$, according to Eq. (B.11) $\langle|\theta|\rangle \simeq \langle w_2\rangle\, t_{12}$. Similarly, $\left\langle\sqrt{|\theta|}\right\rangle \simeq \langle w_2\rangle\sqrt{t_{12}}$. Thus with increasing $t_{12}$, a crossover from linear to square-root behavior is expected. As in Eq. (7.19) for

$t_{12}\gamma_1 \ll 1$ one finds

$$\Gamma_{\text{EFS-J}} \simeq \frac{1}{2\pi} C_2 \langle w_2 \rangle \simeq \frac{1}{2\pi} c C_2 \mathcal{T}_2 \,, \tag{7.24}$$

where again the latter equality holds for a weak second pulse. Interestingly, the condition $t_{12}\Delta_{\max} \ll 1$ in Eq. (7.23), required for an exponential decay, is unlikely to be satisfied in 2PPE. For the pulse-time limited width, one has $\Delta_{\max} \simeq \pi/\tau$ and consequently the exponential decay is limited to the regime $t_{12}/\tau \leq \pi$. Thus primarily the square-root behavior should be observed. Nevertheless, Eq. (7.24) may serve as an upper bound for the EFS broadening by off-diagonal interactions.

### EFS by diagonal versus EFS by off-diagonal interactions

In order to investigate how diagonal and off-diagonal interactions contribute to the line broadening, a particular experiment has been designed, with a scheme inspired by Eq. (7.23) and by the investigations in Refs. (25, 106, 131, 135), where with an extra laser pulse a high excitation density was induced in the system. The timing and laser frequencies are schematically shown in the upper part of Fig. (7.3).

With two weak pulses the echo is generated, whilst with a third scrambler pulse applied during the rephasing period, a strong excitation density is induced. The scrambler pulse is chosen to be in the rephasing period to maximize the broadening effect. To examine whether there is a dependence of the echo on the scrambler frequency, the frequency of the third pulse is shifted by $\Delta\omega_s$.

For the data of $Eu^{3+}$ in $Y_2SiO_5$ , shown in Fig. (7.3), the echo intensity was recorded as a function of $t_{12}$ without and with scrambler pulse. In the latter case the time interval between the second and the third pulse was kept fixed. The scrambler pulse energy was chosen to be three times stronger than the echo pulses. In a third case the scrambler pulse was shifted by $\Delta\omega_s/2\pi = 20$ MHz, a shift clearly larger than the Rabi frequency and the laser jitter of approximately 1-2 MHz. For the predictions, Eq. (7.23) has to be modified by replacing $\Delta_{\max}$ by $|\Delta\omega_s|$, in the case where $|\Delta\omega_s| > \Delta_{\max}$. Assuming a $\delta$-shaped pulse, $\langle|\theta|\rangle$ can be approximated by $\langle|\theta|\rangle \simeq \langle w_3 \rangle (2t_{12} - t_s)$ where $t_s$ denotes the time instance of the scrambler pulse,

and $\langle w_3 \rangle$ is the excitation probability of the scrambler pulse. Correspondingly, $\left\langle \sqrt{|\theta|} \right\rangle \simeq \langle w_3 \rangle \sqrt{2t_{12} - t_s}$. The experimental data suggest that in all three cases only a linear behavior of $\ln(I/I_0)$ is present. Furthermore, up to the experimental accuracy the echo intensity does not dependent on the offset $\Delta\omega_s$. These observations indicate that off-diagonal interactions are negligible for the broadening in the present system and additionally justify the separation of the averages as performed in Eq. (3.16).

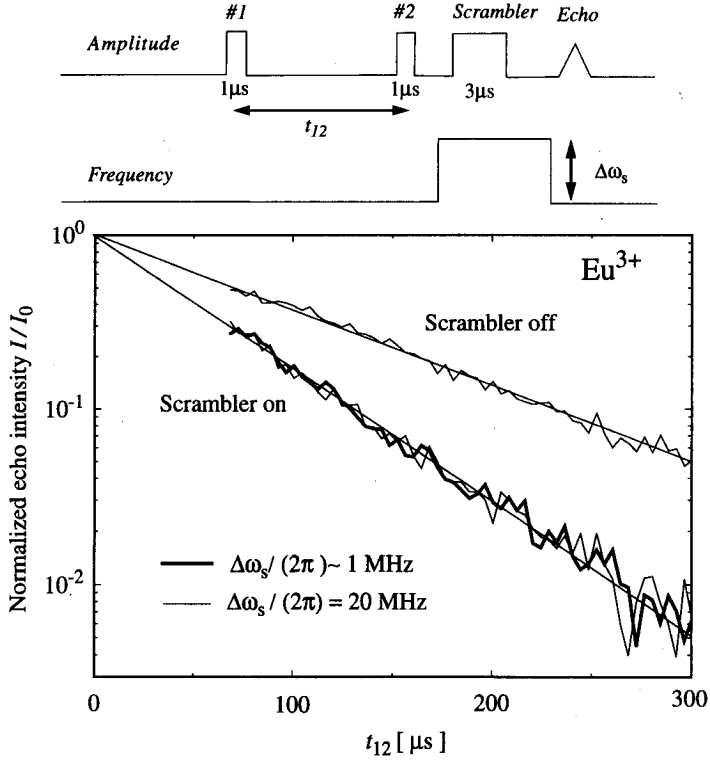


**Figure 7.3:** Echo intensities as a function of the scrambler excitations for $Eu^{3+}$ in $Y_2SiO_5$. In the upper part of the figure the timing of the pulses and the excitation frequencies are depicted. The scrambler pulse is applied at the time $t_s$ in the rephasing period at a frequency shifted by $\Delta\omega_s$. In the lower part the echo intensities are plotted with the scrambler pulse set off and on. The straight lines are guides to the eye. The fact that there is no dependence on the frequency offset $\Delta\omega_s$ suggests that EFS by off-diagonal interactions is negligible.

For the quantitative predictions of the broadening by EFS, the ratio $R$ of the broadening by diagonal and off-diagonal interactions can be calculated. Considering Eqs. (7.19) and (7.24) , $R$ takes the simple form

$$R \equiv \frac{\Gamma_{\mathrm{EFS-J}}}{\Gamma_{\mathrm{EFS-D}}} = \frac{\eta(\omega_0)\mu^2}{\eta(0)(\delta\mu)^2} , \tag{7.25}$$

where, recalling, $\mu$ and $\delta\mu$ are the transition dipole moment along the laser polarization and the static dipole moment difference. $\mu$ can be determined using the expression

$$\mu^2 = \frac{3\hbar e^2 f'}{2\omega_0 m_e} \frac{9\sqrt{\epsilon(\omega_0)}}{(\epsilon(\omega_0)+2)^2} , \tag{7.26}$$

where $f'$ denotes the oscillator strength of the transition in the solid along the electric field polarization. The oscillator strengths is given by $f = 4\pi m_e c\epsilon_0 \ln(10)/(N_A e^2)\mathcal{A} \simeq 1.4 \cdot 10^{-19}\mathcal{A}$, where $\mathcal{A} = \int \epsilon_{\mathrm{ext}}(\nu)\mathrm{d}\nu$ is the integral over the inhomogeneous band of the molar extinction coefficient to the base of ten measured in units of [s mol $10^{-3}$/cm$^2$]. Therefore $f'$ could be determined independently from absorption measurements, employing the same laser polarization and crystal orientation that were used in the current experiments. The second ratio in Eq. (7.26) is the dielectric correction which accounts for $\mu$ being the dipole moment in the vacuum [167]. $\epsilon(\omega_0) \simeq 3.2$ is the dielectric constant at the transition frequency $\omega_0$ [165]. The Stark coefficients $\zeta_S$ are taken from Chapter 6 and serve to determine $\delta\mu$, since

$$\delta\mu = \frac{3\hbar}{\epsilon(0)+2}\zeta_S , \tag{7.27}$$

where the Lorentz field factor accounts for the dielectric correction [168]. The values for $f'$, $\mu$, and $\zeta_S$ are collected in Table 7.1. The dc-dielectric constant $\epsilon(0)$ had to be estimated from values of similar crystals, since for $Y_2SiO_5$ no experimental data is available. Here, it was approximated by $\epsilon(0) \simeq 7$. Based on these parameters, the ratio $R$ of Eq. (7.25) are calculated as $5\times10^{-3}$, $8\times10^{-3}$, and $7\times10^{-4}$ for $Eu^{3+}$ site I, $Pr^{3+}$ site I and $Pr^{3+}$ site II, respectively. These ratios indicate very strongly that in these systems the broadening by off-diagonal interactions is much smaller than that caused by diagonal interactions. This finding is in agreement with the results

of the experiment discussed above and presented in Fig. (7.3). It is furthermore supported by the observation of Root and Skinner, although for a different system, that the predictions based on off-diagonal interactions are significantly smaller than the experimentally measured broadening [158]. Therefore, the further analysis is restricted to diagonal EFS interactions.

**Broadening in $Eu^{3+}$.** The behavior of broadening by EFS is first analyzed for the $Eu^{3+}$ ions. Typical attenuation decays are shown in Fig. (7.4) together with a fit of Eqs. (7.16) and (7.18) to the data using $cC_1$ as the only fitting parameter. The echo

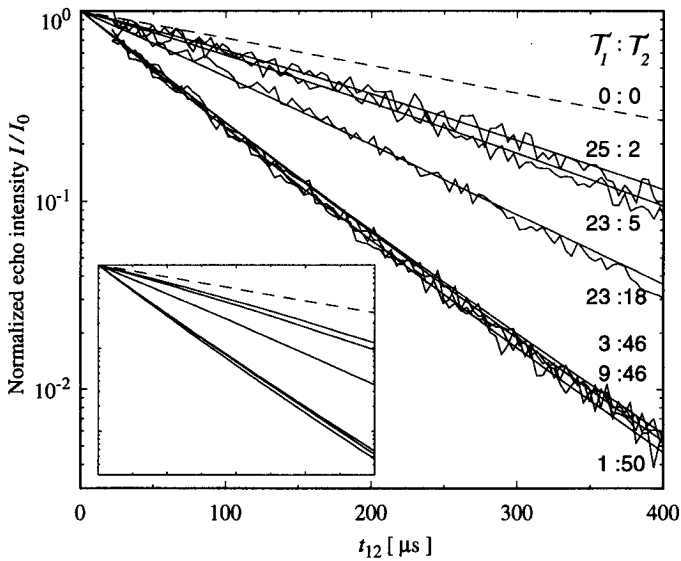


**Figure 7.4:** Echo attenuation by EFS for $Eu^{3+}$ site I in $Y_2SiO_5$. Plotted are the experimental echo intensities along with the fits as a function of the interpulse time $t_{12}$ and the pulse energies $\mathcal{T}_i$. The fits are again reproduced in the inset. The full smooth lines give the calculations according to Eq. (7.18) with a single $cC_1$ value taken as a fitting parameter. The dashed line corresponds to the zero-energy extrapolated broadening, $\Gamma_h = 330$ Hz. (compare Fig. (7.5))

intensity depends predominantly on the energy of the second pulse in agreement with (7.18). Further, a weak tendency of the decay deviating from an exponential towards a more Gaussian behavior for a strong first pulse and towards a stretched

exponential behavior for a strong second pulse can be observed [25].

The echo attenuation was additionally investigated as a function of the frequency position within the inhomogeneously broadened band. The echo intensities were recorded for different total energies $\mathcal{T} = \mathcal{T}_1 + \mathcal{T}_2$ using a fixed ratio $\mathcal{T}_1 : \mathcal{T}_2$. The results are shown in Fig. (7.5). From Eq. (7.18) it is obvious that the broadening by EFS depends linearly on the excitation density in the system. The experimental data of Fig. (7.5) are consistent with such a behavior. As shown in the inset of upon rescaling of the laser-intensity dependent broadening $(\Gamma - \Gamma_\mathrm{h})$ by $\rho_\nu(\nu)$ (the spectral density at the frequency position $\nu$), a data collapse results. As a matter of fact, the extrapolation to small intensities gives the same limiting value $\Gamma_\mathrm{h} = 330$ Hz for all spectral positions. The data collapse confirms the conclusion that the broadening by EFS depends linearly on the excitation density in the system. Additionally it justifies the initial assumption of spatially non-correlated site energies. The present results are in agreement with similar observations in Refs. [127,155,156,169] for other crystals. However, the linear dependence of the broadening on the excitation density is not a unique feature of EFS by diagonal interactions. Root and Skinner [157,158] showed that the broadening by off-diagonal interactions also scales linearly with the concentration and used their approach for the interpretation of the experimental results of Macfarlane et al. [127]. For $Pr^{3+} : LaF_3$ Zhang et al. [156] assigned the dependence of the broadening on the frequency position in the inhomogeneous band to EFS. A linear dependence is also expected for the broadening by NQP, as shall be seen below. Therefore 2PPE measurements carried out at different positions in the inhomogeneous band neither allow for a discrimination between the two type of EFS interactions nor permit for the distinction between EFS or NQP broadening.

Making use of Eqs. (7.14), (7.19), and (7.27) the EFS by diagonal interactions can be quantitatively determined. Again, the calculations are exemplified for the $Eu^{3+}$ ions. One finds that

$$\Gamma_{\mathrm{EFS-D}} \simeq \frac{4\pi}{3\sqrt{27}} p \rho_0 r_0^3 \langle \mathrm{w}_2 \rangle D_0 = \frac{2\pi h p \langle \mathrm{w}_2 \rangle}{3\sqrt{27}\epsilon_0 \epsilon(0) r_0^3} \zeta_\mathrm{S}^2 \,, \tag{7.28}$$

where the parallel case, $\langle |\kappa| \rangle_{||} = 4/\sqrt{27}$ was considered. In expression (7.28), the dielectric correction is reduced to a $1/\epsilon(0)$ screening. $p$, as defined above, denotes

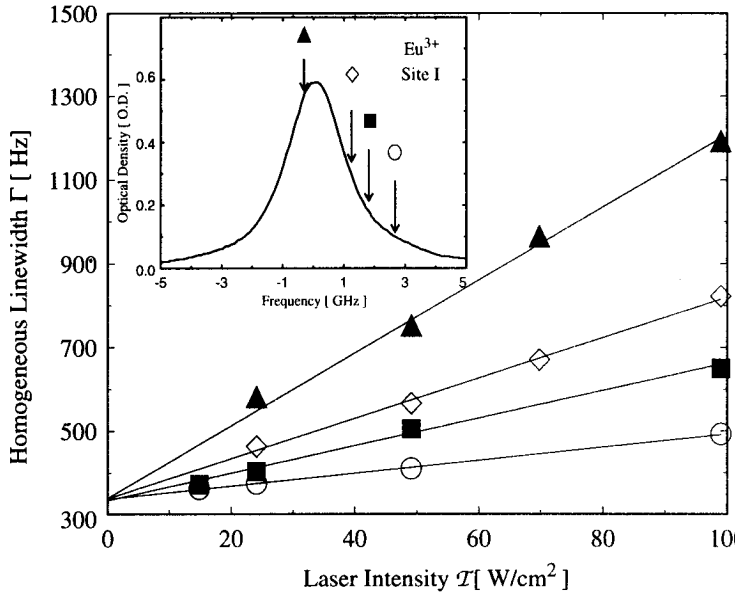


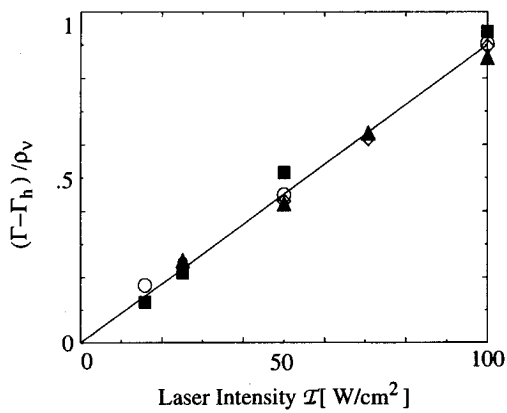


**Figure 7.5:** Line broadening as a function of the position in the inhomogeneously broadened band of $Eu^{3+}$ in $Y_2SiO_5$ . The positions in the inhomogeneous band were the individual curves were recorded are marked in the inset. The linewidths are plotted for these positions as a function of the laser intensity. The straight lines correspond to linear fits. All curves yield the same extrapolated value $\Gamma_h$ = 330 Hz which limits the broadening for this crystal. The figure below depicts the relative broadening $(\Gamma - \Gamma_h)$ rescaled by the line profile $\rho_\nu(\nu)$ on an arbitrary scale. The data collapse indicates that the broadening depends solely on the excitation density in the system.

the relative site-occupation probability which is calculated from the $Eu^{3+}$-ion concentration of 0.1 at.%, corresponding to 0.025 mol-%. Thus $p \simeq 1.25 \times 10^{-4}$, where an extra factor of 1/2 has been introduced because the ions substitutionally occupy two optically distinct sites with equal probabilities. $\langle w_2 \rangle$ is estimated from the saturation effect observed for $Pr^{3+}$ site I, as discussed below, and a value of $\langle w_2 \rangle \simeq 1.6 \times 10^{-4}$ is obtained. For $Y_2SiO_5$ , an average $r_0$ was calculated in Chapter 2, yielding $r_0 \simeq 2.4$ Å for the corresponding cubic lattice unit. $\rho_0$ is fixed by setting $\rho_0 r_0^3 = 1$. For the range $t_{12} \leq 400\mu$s and $T_1 \simeq 2$ ms the condition $\gamma_1 \, t_{12} \ll 1$ is obeyed so that Eqs. (7.19) and (7.28) are applicable. For $Eu^{3+}$ site I, one finds $\Gamma_{\text{EFS-D}} \simeq 650$ Hz which compares with the experimental value of 850 Hz.

**Broadening in $Pr^{3+}$.** Based on the calculations presented for $Eu^{3+}$, the echo decays observed in $Pr^{3+}$:$Y_2SiO_5$ site I are now analyzed. As shown in Chapter 2, the spin dynamics in $Y_2SiO_5$ can be fully attributed to the $^{89}$Y-spins; frozen-core effects are ignored here. From Table 7.1 one finds that in the case of $Pr^{3+}$ site I the difference in the homogeneous broadening with and without field is approximately $\Gamma_h(H = 0) - \Gamma_h(H > 500\text{G}) \simeq 450$ Hz. This difference was observed to be about five times smaller for $Pr^{3+}$ site II and $Eu^{3+}$ site I. For the latter two, the spin-ion contribution were therefore approximated by an exponential [21, 42]. For $Pr^{3+}$ site I, however, the broadening by SI is strong enough so that the non-exponentialities according to Eq. (7.2) should be visible. In Fig. (7.6), a typical photon-echo decay for $Pr^{3+}$ site I at intermediate pulse energies is shown along with the broadening by SI with $k_1 = k_2 = T_m^{-1}$, using Eq. (7.2), the broadening by EFS, and the intrinsic broadening $\Gamma_0$ exclusive the SI contribution.

From Fig. (7.6) it is clear that the non-exponential behavior by SI is weak and is partially masked by the competing effect through EFS. In the fit $\Gamma_0$ was set equal to $\Gamma_h \simeq 1200$ Hz, corresponding to the measured zero energy extrapolated broadening in an external magnetic field. The flip rate $T_m$, and the prefactor for the broadening by EFS were adjusted to the experiment. The prefactor $c_{SI}$ was fixed, so that the SI contribution corresponded to the difference between the homogeneous widths with and without magnetic field. This resulted in a flip rate of $T_m \simeq 200$ $\mu$s. Because of the weak broadening by spin-ion interactions, and particularly because of the super-

position of two effects the value of $T_m$ is only very approximate. As demonstrated in Fig. (7.6) the echo decays deviate only weakly from the non-exponential behavior, especially for larger $t_{12}$. Therefore, in all further evaluations the data of $Pr^{3+}$ site I were fitted to an exponential law, restricting the times to $t_{12} > 20\mu s$.

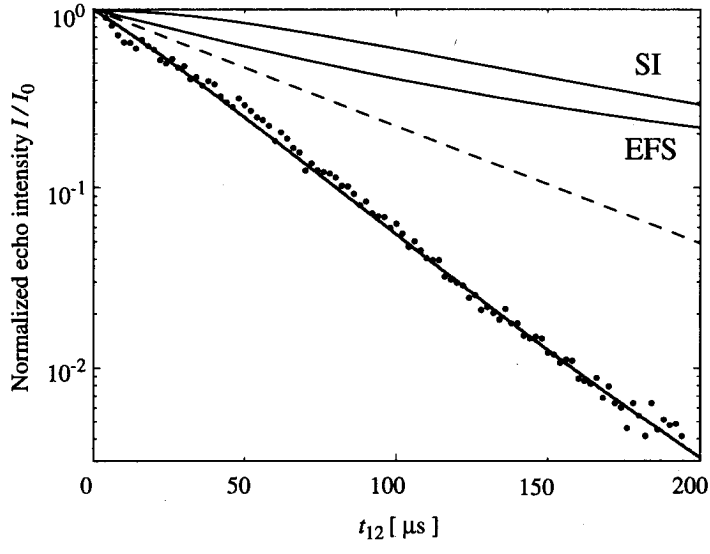


**Figure 7.6:** Competing broadening mechanisms for $Pr^{3+}$ site I in $Y_2SiO_5$. Plotted is a typical echo decay for a moderate laser intensity. The thick full line through the data is the fit. The thin dashed line gives the intrinsic broadening $\Gamma_h \simeq 1200$ Hz obtained from zero-energy extrapolation with the magnetic field set-on. The thin full lines are the SI and EFS contributions. See text for details.

The linewidths in Fig. (7.7) are given for a fixed ratio $2\mathcal{T}_1 : \mathcal{T}_2 = 1$, according to the ratio $\tau_1/\tau_2 = 1/2$ and an equal laser intensity $\mathcal{I}$ for the two pulses. As a function of $\mathcal{I}$ the experimental linewidths follow a linear behavior at low intensities and show saturation at large intensities. At saturation the observed broadening is 1100 Hz. The full line gives the fit of $\Gamma = \Gamma_h + A[1 - \exp(-c_1\mathcal{I})]$, with $A$ and $c_1$ as adjustable parameters. The figure indicates that the data monotonically approach the saturation value. The resolution of the data is probably too small for the detection of a maximum in the broadening, predicted in Fig. (A.1). Equally

well, laser-field inhomogeneities may be present so that the hump in the broadening is smoothed out, as discussed in Appendix A.

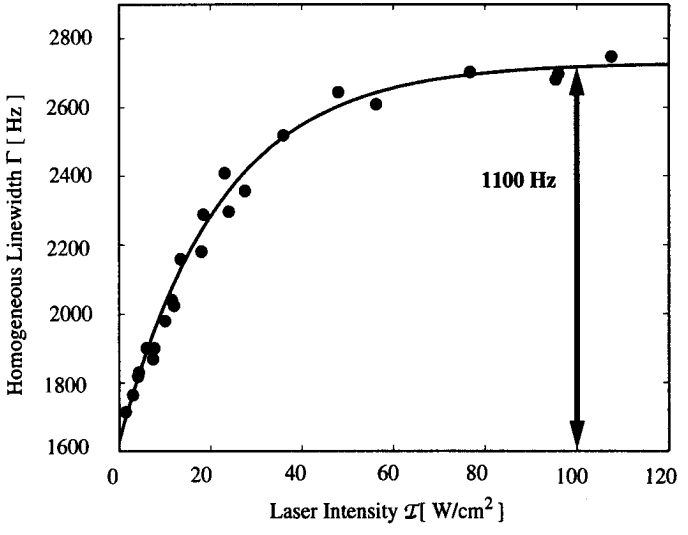


**Figure 7.7:** Linewidths of $Pr^{3+}$ site I in $Y_2SiO_5$ as a function of the laser intensity $\mathcal{I}$. The linewidths were measured without magnetic field and are given for a fixed ratio $2\mathcal{T}_1 : \mathcal{T}_2 = 1$ of the pulse energies. The full line is the fit $\Gamma = \Gamma_h + A\,[1 - \exp(-c_1\mathcal{I})]$, see text. The value extrapolated to zero power yields $\Gamma_h = 1650$ Hz.

In Fig. (7.8) echo intensities of $Pr^{3+}$ site I are presented for different ratios $2\mathcal{T}_1 : \mathcal{T}_2$.Because of the small relative broadening the $t_{12}$ times had to be extended up to 200 $\mu$s in order to detect the pulse energy dependent broadening. This time scale is comparable to $T_1 = 165$ $\mu$s so that the $\gamma_1 t_{12} \ll 1$ condition is not satisfied. Correspondingly, Eq. (7.18) has to be applied instead of Eq. (7.19), and a dependence of the echo also on the energy of the first pulse is expected. In fact, such a dependence is observed.

For a comparison, the echo intensity was also investigated for $Pr^{3+}$ site II. The echo signal was weak if compared with the site I intensity because of the much smaller oscillator strength. No broadening effect could be observed up to a laser intensity of 100 W cm$^{-2}$. It was concluded that the laser intensity dependent broadening

is smaller than 100 Hz which approximately marks the visibility limit. Independent measurements in a 0.1% $Pr^{3+}$:$Y_2SiO_5$ doped crystal showed that at higher concentrations an intensity dependent broadening is present in accordance with the observations by Equall et al. [42].

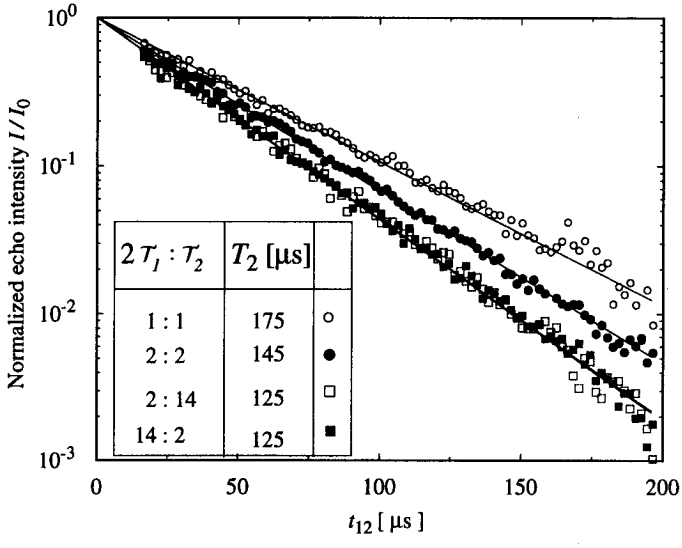


**Figure 7.8:** Echo attenuation for $Pr^{3+}$ site I in $Y_2SiO_5$. Plotted are the echo intensities as a function of $t_{12}$ for several energies of the two pulses. The duration of the first pulse was chosen to be half of the second pulse duration. The ratios of the pulse energies are indicated in the inset as $2\mathcal{T}_1 : \mathcal{T}_2$ for an arbitrary scale. The full lines are fits to the exponential law with the corresponding $T_2$ also given in the inset.

For $Pr^{3+}$, the broadening was calculated according to the procedure presented above for $Eu^{3+}$ by taking into account the corresponding excitation densities, dipole moments, and ion concentrations. The calculation of the excitation probability $\langle w_2 \rangle$ is based on the saturation behavior in the echo attenuation of $Pr^{3+}$ site I. From the comparison of the experimental saturation behavior shown in Fig. (7.7) to the calculated one presented in Fig. (A.1), the maximum of $\langle w \rangle \sigma_\nu \tau$ in Fig. (A.1) is estimated at $\chi_2^2 = 11.5$, corresponding to a laser intensity of $\mathcal{I} \simeq 25$ Wcm$^{-2}$. The excitation probability in Fig. (A.1) saturates at a value of $\langle w \rangle \sigma_\nu \tau = 0.4$ so that one

finds $\langle w_2 \rangle \simeq 0.4/(\sigma_\nu \tau_2) \simeq 9.6 \times 10^{-5}$ at saturation. According to Eq. (7.28) and the data of Table I, $\Gamma_{\mathrm{EFS-D}} \simeq 450$ Hz for $Pr^{3+}$ site I, roughly a factor of two smaller than the experimentally observed 1100 Hz. For the Rabi frequencies of $Eu^{3+}$ and $Pr^{3+}$ site II the dependence of the Rabi frequency on the oscillator strength and the laser energy, $\chi^2 \sim f\mathcal{T}$ is considered. From $\chi_2^2 = 11.5$ for $Pr^{3+}$ site I at $\mathcal{I} \simeq 25$ $Wcm^{-2}$ the corresponding values $\chi_2^2 = 3.2$ for $Eu^{3+}$ and $\chi_2^2 = 2.7$ for $Pr^{3+}$ site II at the laser intensity of $\mathcal{I} = 100$ $Wcm^{-2}$ are derived. Using these parameters, and making use of Eq. (A.5), one finds $\langle w_2 \rangle \simeq 1.35 \times 10^{-4}$ and $9.6 \times 10^{-5}$ for $Eu^{3+}$ and $Pr^{3+}$ site II, respectively. The value of $\langle w_2 \rangle \simeq 1.35 \times 10^{-4}$ was applied above in the calculation of the broadening for $Eu^{3+}$. For $Pr^{3+}$ site II $\Gamma_{\mathrm{EFS-D}} \simeq 300$ Hz is obtained, a value about a factor of two to three larger than the visibility limit.

It can thus be concluded that for all investigated systems, the predicted broadenings agree within a factor of two to three with the experimental results. Part of the discrepancies arise due to the uncertainties of the different parameters. The dielectric constant $\epsilon(0) \simeq 7$ is only a conjecture and its anisotropic properties are not considered at all. Furthermore, the effective concentration of the ion in the crystal might be different from the one given by the nominal weight percents. Finally, NQP may additionally contribute to the broadening as shall be discussed in the next Subsection.

### 7.3.4 Non-equilibrium phonons

For the analysis of the echo attenuation by NQP the following independent processes have to be considered: the generation and relaxation of NQP, the propagation of the NQP in the solid and the interaction between the NQP and the excitations involved in the echo process. NQP are generated directly by spontaneous decays from the pumped electronic state to ground state phonon modes by electron-phonon coupling. In the case where there are low-lying electronic states, these states may be populated by the spontaneous transitions and the population of these levels may then subsequently relax into NQP. The lifetime of NQP depends strongly on their frequency $\nu_p$. As mentioned in Chapter 2, for $\nu_p > 1$ THz the phonon lifetime $\tau_p$ limited by anharmonic relaxation was found to follow a $\tau_p \sim \nu_p^{-5}$ law [33–35]. Superimposed

to that, if there are several low-lying electronic levels the NQP relaxation by repeated inelastic scattering may efficiently occur so that eventually a large density of phonons resonant with the lowest electronic level is accumulated. This path is particularly feasible if the low-lying electronic levels are within the Debye frequency range. If there are several different ion species, the number of relaxation paths is increased and the lowest level out of all ion levels may act as a bottleneck so that NQP are accumulated at a frequency resonant with this level. Elastic scattering of NQP resonant with the lowest electronic state can occur many times before the NQP decay by anharmonic relaxation.

In the quasi-particle picture of phonon dynamics, the phonons are assumed to perform random walks through the crystal by elastic scattering and to relax by inelastic scattering. They are also scattered at electronically excited impurity ions and these scattering processes give rise to a dephasing [35, 131, 132], as schematically shown in Fig. (7.9). The dephasing is particularly efficient when electronic

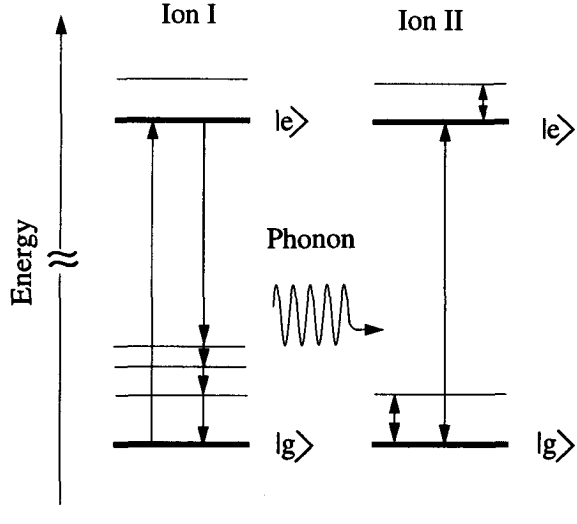


**Figure 7.9:** Schematic representation of the echo attenuation by NQP. The excitation of ion I decays spontaneously and populates low lying electronic states. These populations decay by generating non-equilibrium phonons. Resonant and non-resonant scattering of the phonons at transitions in the ground and excited state of ion II lead to a dephasing in the electronic excitation.

transitions of the ion involved in the echo process are resonant with the NQP. While these resonances are more likely for ground state transitions, they might also occur for transitions in the excited state, if the frequency gaps between the pumped state

and higher electronic states are comparable to the phonon frequencies. In this case, depending on the electronic excitation density and the scattering cross sections, an accumulation of NQP resonant with these transitions may take place. Resonances of NQP with transitions in the ground and the excited states lead to a lifetime shortening of the ground or excited state, respectively. These shortenings give rise to a dephasing in the excitation of an ion in the superposition state and thus to an echo attenuation. The efficiency of the attenuation by NQP is limited, apart from the phonon lifetime, by the time of detuning from the resonances and by the time at which the NQP diffuse out of the area probed by the laser [131, 170]. Bai and Kachru interpreted their experimental results in terms of 51 $cm^{-1}$ NQP, resonant with the lowest electronic state of $Pr^{3+}$ in $YAlO_3$. Macfarlane and Meltzer [132], as mentioned in the introduction, pumped an electronic state 29 $cm^{-1}$ higher than the state involved in the echo process with a second laser source. In this way NQP of 29 $cm^{-1}$ were generated by phonon-assisted relaxation to the lower state. The increased broadening was attributed to the resonance with the 29 $cm^{-1}$ NQP.

From the preceding considerations it is obvious that the broadening by NQP depends crucially on the electronic level scheme of the ions. From Fig. (2.6) it can be seen that for $Pr^{3+}$ site I, the lowest Stark levels of the $^3H_4$ and of of the $^1D_2$ states are separated by 88 $cm^{-1}$ and 59 $cm^{-1}$, respectively [42]. For $Pr^{3+}$ site II, the corresponding energy gaps are significantly larger, namely 176 $cm^{-1}$ and 200 $cm^{-1}$. For $Eu^{3+}$ site I in the ground state, the lowest of the $^7F_1$ Stark levels is shifted by 203 $cm^{-1}$ from the $^7F_0$ level [92]. In the excited state the closest lying level is as far as 1707 $cm^{-1}$ [43]. This situation is similar for $Eu^{3+}$ site II. For $Nd^{3+}$, also contained in the present system, the lowest level is shifted by 91 $cm^{-1}$ and 68 $cm^{-1}$ from the ground state for site I and site II [36]. From these values it appears that broadening by NQP is likely to occur for $Pr^{3+}$ site I, where the 88 $cm^{-1}$ level may be resonant with NQP. However, this level is higher than the 68 $cm^{-1}$ state of $Nd^{3+}$site II, so that the latter level may act as a bottleneck. Even smaller is the 59 $cm^{-1}$ transition of $Pr^{3+}$ site I in the excited state so that this transition may also work as a bottleneck. In order to estimate the approximate magnitude of NQP induced broadening contributions, a collision model is considered. Here, use is made of the expression $\Gamma_{NQP} \simeq \sigma_0 v_p N_p/\pi$ [171], where $\sigma_0$ is the cross section for

elastic scattering, $v_p$ denotes the phonon velocity, and $N_p$ is the density of phonons. For the estimate, the data of Baumgartner et al. [35] obtained for $CaF_2$ and of Renk [170] measured for $V^{4+}$:$Cr^{3+}$:$Al_2O_3$ are considered. The resonant cross section is of the order $\sigma_0 \simeq 10$ nm$^2$. For inelastic scattering, the cross section is orders of magnitude smaller, depending on the energy mismatch. The phonon velocity is taken as $v_p \simeq 5 \times 10^3$ ms$^{-1}$ and the phonon density is calculated from a steady state approach [131], which yields

$$N_p/N^* = q(\tau_p/T_1) \,, \tag{7.29}$$

where $N^*$ is the density of the excited ions and $T_1$ is the corresponding lifetime. $q$ is the number ratio of resonant NQP over decaying excitations. This factor is diminished when the electronic excitation population is spread over several levels. However, $q$ may also be increased by several processes the most prominent one being the bottleneck effect, when NQP resonant with the electronic transition are accumulated. In such a case a single electronic decay may lead to several resonant NQP. Using the data for $Pr^{3+}$ site I, $N^*$ is estimated from the considerations in the previous Section by setting $N^* = \langle w \rangle p/r_0^3$, so that with $p = 1.25 \times 10^{-5}$ and $\langle w \rangle = 1.6 \times 10^{-4}$ , $N^* \simeq 1.4 \times 10^{14}$ cm$^{-3}$ is obtained. Setting $q = 0.1$ and using the phonon lifetime of $\tau_p \simeq 0.5$ $\mu$s results in $N_p = 4 \times 10^{10}$cm$^{-3}$ and correspondingly $\Gamma_{NQP} \simeq 700$ Hz. Because there are several competing phonon-relaxation processes, bottlenecking, detuning, and anharmonic relaxation, and because the quantities used in this calculation are rough estimates, the calculated broadening is somewhat arbitrary. Nevertheless, a substantial contribution to the broadening by NQP for $Pr^{3+}$ site I is feasible. Such a contribution would lift the discrepancy between the prediction based on EFS and the observed broadening for $Pr^{3+}$ site I.

From the level scheme shown in Fig. (2.6) and from the $\nu_p^{-5}$-law of the phonon lifetimes it is clear that the broadening by NQP is much less likely to occur for $Pr^{3+}$ site II and for $Eu^{3+}$ site I. Taking the corresponding parameters used for the estimate carried out for $Pr^{3+}$ site I, in both cases sub-Hz broadening by NQP is expected. That NQP are negligible for these two systems is further supported by the fact that no power depending broadening was observed in $Pr^{3+}$ site II and that the $Eu^{3+}$ data could be fitted assuming EFS only.

So far, it was only discussed whether broadening by NQP is principally feasible. Concerning the dependence on the pulse strength, an expression is derived in Appendix D which up to a correction term reads

$$-\ln\left(\frac{I}{I_0}\right)_{\mathrm{NQP}} \sim \langle \mathrm{w}_1\rangle \left(1-e^{-2\gamma_1 t_{12}}\right) + \langle \mathrm{w}_2\rangle \left(1-e^{-\gamma_1 t_{12}}\right) \ . \tag{7.30}$$

This expression is clearly different from the corresponding one for EFS given in Eq. (7.17). For $\gamma_1 t_{12} \ll 1$ the broadening is

$$\Gamma_{\mathrm{NQP}} \sim 2\mathcal{T}_1 + \mathcal{T}_2 \ , \tag{7.31}$$

which, similar to Eq. (7.19) for EFS, is regarded as a signature of the broadening by NQP [131]. NQP and EFS are generally expected to simultaneously lead to a broadening. Assuming $\gamma_1 t_{12} \ll 1$, the combination of Eqs. (7.19) and (7.31) gives

$$\Gamma \sim \beta\mathcal{T}_1 + \mathcal{T}_2, \quad \text{with} \quad \beta \in [0,2] \ , \tag{7.32}$$

where $\beta$ indicates the mixing of the two effects, so that $\beta = 0$ corresponds to pure EFS and $\beta = 2$ to pure NQP broadening, respectively. Concerning $Pr^{3+}$ site I, as mentioned above, $t_{12}$ had to be chosen long compared to $T_1$ in order to detect the pulse energy dependent attenuation. At these times, $\Gamma \sim \beta\mathcal{T}_1 + \mathcal{T}_2$ is not applicable so that the discrimination between the broadening by EFS and NQP is more difficult. It is worth noticing that Equall et al. considered only EFS for the interpretation of the power dependent broadening for $Pr^{3+}$ in $Y_2SiO_5$ [42].

Making use of the above scattering model the diffusion constant can also be estimated. The mean free path between scattering events is $\lambda = 1/(N\sigma_0)$, where $N$ is the concentration of ions resonant with the NQP. Taking for the elastic scattering centers only the $Pr^{3+}$ site I ions yields $N \simeq 1 \times 10^{18}\mathrm{cm}^{-3}$ from which $\lambda \simeq 100$ nm is obtained for the mean free path and $D = \lambda^2/(6\tau_{\mathrm{scattering}}) = \lambda v_{\mathrm{p}}/6 \simeq 1\mathrm{cm}^2\ \mathrm{s}^{-1}$ for the diffusion constant. Furthermore, the diffusion distance within the phonon lifetime is calculated to be $\langle r^2\rangle^{1/2} \simeq (2D\tau_{\mathrm{p}})^{1/2} \simeq 10\mu$m. This value is somewhat too small if compared to the study of Bai and Kachru [131], in which a dependence on the laser focus for areas larger than 0.025 mm$^2$ is reported, corresponding to a

radius $r \simeq 100$ $\mu$m. Comparing the diffusion length with the 45 $\mu$m beam waist of the present experiments it is suspected that only a fraction of the NQP diffuse out of the excitation area. However, with detuning of the NQP from resonance the scattering cross section decreases rapidly, so that the detuned phonons are more likely to escape from the excitation area.

## 7.4 Conclusions

In this Chapter, the echo attenuation of $Eu^{3+}$ and $Pr^{3+}$ ions diluted in a $Y_2SiO_5$ crystal has been studied as a function of several parameters. The discussion of the broadening by EFS and NQP has been based on statistical grounds. Since dephasing is a quantum coherence problem, quantum mechanical and statistical aspects have been combined in this analysis. EFS has been analyzed in terms of diagonal- and off-diagonal interactions. An experiment has been proposed to distinguish between the two types of effects. The experimental results and the numerical predictions strongly indicate that EFS by off-diagonal interactions are negligible in the system considered in this work. It should be emphasized that this claim does not hold generally because the broadening depends on the properties of the photo-active species. Based on Stark experiments presented in Chapter 6, quantitative predications of EFS broadening by diagonal interactions were performed. The comparison with the measured broadening by EFS for $Eu^{3+}$ and $Pr^{3+}$ have revealed that the calculations are accurate to roughly a factor two. Inaccuracies arise from several experimental quantities which enter the calculations: oscillator strength, inhomogeneous width, static dipole-moment differences, and the excitation probabilities by the laser pulses. These inaccuracies are believed the be the reason for the deviations between theory and experiment, rather than that modifications of the model are required.

It appears quite remarkable that a very low excitation density can give rise to EFS which can be detected by photon echoes. For $p\langle w\rangle \simeq 1 \times 10^{-8}$ obtained for $Eu^{3+}$ site I in Section 7.3.3, the closest distance between excited ions is typically as large as 100 nm and yet, the interactions lead to measurable effects. Accounting of the small dipole-moment differences of $10^{-2}$ D, this observation demonstrates

the power of the photon-echo spectroscopy for the investigation of extremely small changes in the environment. Correspondingly it can be argued that TLS even at very low concentrations may lead to a detectable dephasing. This gives support to the hypothesis that differences in the optical behavior between crystals grown under nominally identical conditions may be attributed to TLS.

Magnetically induced EFS broadening has not been analyzed in this work. A rough estimate shows that this factor is negligible for all systems studied here. $Pr^{3+}$ and $Eu^{3+}$ both belong to the non-Kramers ion group with magnetic moments of approximately 1 $\mu_N$. This value is comparable to the magnetic moment of the host ion (compare Section 2.2.3). Further, for all transitions the spin-ion induced broadening was measured to be below 500 Hz. Since the average distance of a guest ion to a host ion is several orders smaller than the distance to another guest ion, one can safely state the EFS induced broadening deriving from magnetic interactions must be below 100 Hz and can therefore neglected. In general however, this is not true [107], and Section 7.3.3 needs to be adapted correspondingly.

Concerning the effect of non-equilibrium phonons, the made predictions are only qualitative and estimates based on a phonon-scattering model remain vague. The attenuation by NQP depends crucially on the energy level scheme of the ions because the broadening is dominated by the resonance between the NQP and transitions of the ions. The investigation of 2PPE in other systems and especially of the NQP properties is required to shed more light on this type of broadening. The characteristics of the broadening by EFS and NQP as a function of the pulse intensities facilitate the distinction between the two broadening processes. For sufficiently small pulse energies, the representation of the broadening as a function of $\beta\mathcal{T}_1 + \mathcal{T}_2$, as proposed here, provides a means to graphically get information about the two broadening mechanisms. The quality of the present experimental results and the choice of the systems have turned out to be not ideal to unambiguously attribute part of the broadening to NQP. From the estimates, however, a considerable NQP broadening for $Pr^{3+}$ site I is plausible. Correspondingly, one can argue that due to the 23 $cm^{-1}$ level spacing in the excited state of $Pr^{3+}$ in $LaF_3$ [132] NQP may also be of importance, in contrast to earlier reports where the pulse-energy dependence of the linewidth was solely attributed to EFS [156]. Additionally, the dependence

of the echo attenuation as a function of the frequency position in the inhomogeneously broadened band has been studied for $Eu^{3+}$ in $Y_2SiO_5$. The results confirm the prediction that the echo-attenuation by EFS depends linearly on the excitation density in the system. However, such a dependence also holds for the attenuation by NQP, so that these experiments do not allow for the distinction between the two broadening processes.

The experiments presented in this Chapter, were all carried out in an optically thin crystal and also the theoretical considerations have been based on the thin crystal approximation. As already pointed out earlier, the situation may dramatically change for thick crystals, because the effect of light propagation cannot be disregarded anymore. Longitudinal inhomogeneities in the laser field may significantly change the characteristics of echo dependence on $t_{12}$ and on the pulse intensities.

Summarizing, the broadening induced by various dynamical processes has been studied here. Experimental results obtained from a single system were compared to theoretical predications based on a stochastic model and reasonable agreement has been achieved. The consideration of the characteristic behavior and of the quantitative estimates may render possible the selection of systems specially suited for the investigation of a particular broadening mechanism in future investigations.

# 8. Conclusions and outlook

.... She went on, "Would you tell me please which way I ought to go from here?"
"That depends a good deal on where you want to get to," said the Cat.
"I don't much care where-" said Alice.
"Then it doesn't matter which way you go," said the Cat.
"-as long as I get somewhere," Alice added as an explanation.
"Oh, you sure do that," said the Cat, "if you only walk long enough."

*Alice in Wonderland,* Lewis Carroll

The work presented here focused on two applications of RE ion doped crystal spectroscopy: the possible use of these materials as frequency markers and their suitability as very sensitive probes for measuring the interaction with the environment. By means of an ultra-high resolution cw-laser and non-linear spectroscopic techniques, investigations of the spectral dynamics of the guest/environment system were carried out.

Using a side band modulation laser locking scheme, persistent spectral holes with linewidths in the range of 10-30 kHz could be burned. This allowed for the verification of the laser system characteristics, as well as the measurements of the long term behavior of the hole burning material with kHz resolution. Within the detection limit given by the laser linewidth, it was found that the hole width of the persistent holes of $Eu^{3+}:Y_2SiO_5$ is constant over several ten's of minutes and that at 1.7 K the persistence of the hole lifetime exceeds 10 hours. From these perspectives, $Eu^{3+}:Y_2SiO_5$ appears to be very well suited for the investigation of small frequency changes over long time periods.

By means of two-pulse photon echoes, various dynamical processes were investigated on the $\mu$s-ms time scale. Particular focus was placed on the echo attenuation by excitation induced frequency shifts (EFS), spin-ion interactions (SI), non-equilibrium phonons (NQP), and lattice two level systems (TLS). The experiments revealed that in order to observe narrow spectral lines, all of these factors need to be controlled and minimized, either by the choice of the material or by the choice of the experimental parameters. Characteristic behaviors have been sketched which should allow for a better discrimination between the different contributions in future studies.

The experiments and the theoretical predictions showed that for the particular system $Eu^{3+}:Y_2SiO_5$ the major contributions to the line broadening arise from diagonal EFS interactions and that the off-diagonal EFS interactions are negligible. The diagonal EFS term is guest-guest ion driven and arises due to a difference between the static dipole moments in the ground and the excited state. Thus, upon a configurational change of one ion, the local field at another ion changes which affects its resonance frequency and leads to an attenuation of the echo amplitude. Although

typical distances between interacting states were found to be in the 100 nm range, measurable attenuations were observed, demonstrating the extreme sensitivity of RE ion doped crystals to perturbations.

Since the transition dipole moment and the static dipole moment difference are independent quantities, it appears that in an ideal system the latter one should be reduced at a constant value of the transition dipole moment. To verify whether this task is achieved requires the precise measurement of static dipole moment differences. In this work it was shown that generally if an electric field pulse of variable length is applied during either the dephasing or the rephasing period of a two-pulse photon echo, complicated modulations of the echo intensity are observed. These modulations allow for the sensitive determination of the magnitude as well as of the orientations of the static dipole moment differences.

It thus appears that a combination of electric field measurements, ultra high resolution cw-spectroscopy and the extremely sensitive method of photon echo spectroscopy may be the right tools to characterize and investigate RE ion doped crystals on different time scales.

If one considers atom optics and the spectroscopy of single molecules in solids, two currently very active fields, it seams that the spectroscopy of a single RE ion in a solid could combine the advantages of the two, namely the study of the interaction of a relatively easy to treat probe with its environment at a very high precision. In principle this task is not impossible to reach but it is clear that with a signals of a few hundred photons/s available it becomes a big technical challenge for the experimentalists. The future will tell us whether this will be one of the "ways" taken in the investigations of RE ion doped crystals.

Leer - Vide - Empty

# Appendices

## A Rabi solution of the excitation density

In this Appendix the excitation density for an inhomogeneously broadened band is determined, using the density matrix approach. A similar approach was followed by Zhang and Mossberg [156]. For this calculation, damping for times shorter than the pulse times $\tau_{1,2}$ are disregarded. Further, only the population difference $r_3$ of the Bloch vector $\mathbf{r} = (r_1, r_2, r_3)$ is considered which after the first pulse reads [61]

$$r_3(\tau_1; \Delta, \chi_1) = \frac{\Delta^2 + \chi_1^2 \cos\left(\tau_1 \sqrt{\Delta^2 + \chi_1^2}\right)}{\Delta^2 + \chi_1^2} r_3(0) \ , \tag{A.1}$$

where $\Delta$ is the offset, the transition frequency relative to the laser frequency, and $\chi_k$ denotes the Rabi frequency of pulse $k$. The initial state is again given by $\boldsymbol{r}(0) = (0, 0, -1)$. If $\mathrm{w}_1$ denotes the density matrix element $\rho_{22}(\tau_1)$, then

$$\mathrm{w}_1 = \rho_{22}(\tau_1) = \frac{1}{2}\left[1 + r_3(\tau_1; \Delta, \chi_1)\right] = \frac{\chi_1^2 \left[1 - \cos\left(\tau_1 \sqrt{\Delta^2 + \chi_1^2}\right)\right]}{2\left(\Delta^2 + \chi_1^2\right)} \ , \tag{A.2}$$

making use of $\rho_{11} + \rho_{22} = 1, \forall \tau$. The average excitation density is obtained from the integration over the inhomogeneously broadened band. Assuming that the band is of Gaussian shape, that the laser frequency is tuned to the center of the band, and that the width of the band is much larger than the Rabi frequency, the spectral density can be approximated by a constant equal to the density at the band center

$1/\left(\sqrt{2\pi}\sigma_\nu\right)$ where $\sigma_\nu$ is the standard deviation of the band in units of Hz. Thus,

$$\langle \mathrm{w}_1 \rangle = \frac{\vartheta_1}{(2\pi)^{3/2}\sigma_\nu \tau_1} \int_0^\infty \frac{1-\cos\left(\vartheta_1\sqrt{1+x^2}\right)}{1+x^2}\mathrm{d}x \ , \tag{A.3}$$

where $\vartheta_k = \chi_k \tau_k$ denotes the area of pulse $k$. The average excitation density depends on $\vartheta_1$ and parametrically on the dimensionless quantity $\sigma_\nu \tau_1$. Making use of the derivation of Kunitomo and Kaburagi [72], Eq. (A.3) can be cast into

$$\langle \mathrm{w}_1 \rangle = \frac{\vartheta_1}{4\sqrt{2\pi}\sigma_\nu \tau_1} \int_0^{\vartheta_1} J_0(x)\mathrm{d}x \ , \tag{A.4}$$

which is easily integrated numerically by standard routines. For small $\vartheta_1$ values, to lowest order one has

$$\langle \mathrm{w}_1 \rangle \simeq c\mathcal{T}_1 \quad , \quad c = \frac{1}{4\sqrt{2\pi}\sigma_\nu} \ , \tag{A.5}$$

where $\mathcal{T}_k$ denotes the pulse energy, $\mathcal{T}_k = \chi_k^2 \tau_k$.

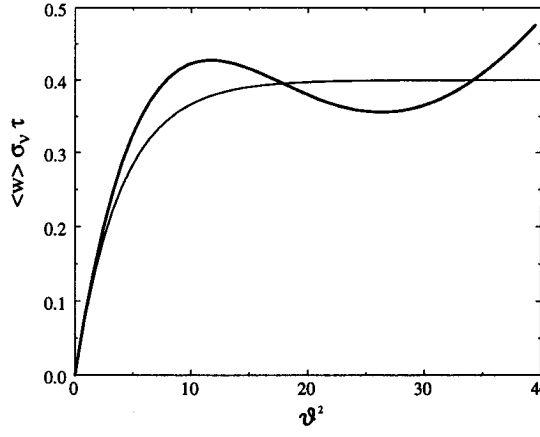


**Figure A.1:** Excitation density after a single pulse. Plotted is the averaged excitation probability $\langle \mathrm{w} \rangle = \langle \rho_{22}(\tau;\chi) \rangle$ times $\sigma_\nu \tau$, as a function of $\vartheta^2$ for the case of $\sigma_\nu \gg \chi$. The thick line gives the calculation of Eq. (A.3). A maximum is observed at $\vartheta^2 \simeq 11.5$. The thin line is $0.4\left(1-\exp(-2.5c\vartheta^2)\right)$, representing the approximate saturation behavior on the scale of $\vartheta^2 \leq 4\pi^2$.

The behavior of $\langle w \rangle \sigma_\nu \tau$ as a function of $\vartheta$ is demonstrated in Fig. (A.1) where for clarity the index $k$ of the pulse is omitted. For $\vartheta \ll \pi/2$, $\langle w \rangle$ depends quadratically on $\vartheta$. The first maximum is found at $\vartheta^2 \simeq 11.5$. For larger $\vartheta$ values the overall behavior is linear in $\vartheta$ with an oscillatory behavior superimposed.

This oscillatory behavior is expected to be smoothed out in the experimental observations because of laser field inhomogeneities. On the scale of the figure, the shape of the function suggests a saturation behavior. Therefore given is also the exponential behavior $0.4\,[1 - \exp(-2.5c\vartheta^2)]$. A similar exponential behavior is used in Fig. (7.8) as a guide to the eye.

For the excitation density at time $t_3$ after the second pulse the Rabi solution is [61]

$$r_3(t_3) \simeq -\frac{\left[\Delta^2 + \chi_1^2 \cos\left(\tau_1 \sqrt{\Delta^2 + \chi_1^2}\right)\right]\left[\Delta^2 + \chi_2^2 \cos\left(\tau_2 \sqrt{\Delta^2 + \chi_2^2}\right)\right]}{(\Delta^2 + \chi_1^2)\,(\Delta^2 + \chi_2^2)}\,, \qquad \text{(A.6)}$$

where terms depending on $\sin(\Delta t_{12})$ and $\cos(\Delta t_{12})$ are disregarded because they contribute negligibly when integrating over the offset $\Delta$ provided that $t_{12} \gg \tau_{1,2}$. Denoting by $w_2$ the excitation probability for an independent second pulse, one may write

$$\rho_{22}(t_3) = \frac{1}{2}\,(1 + w(t_3)) = w_1 + w_2 - 2w_1 w_2\,. \qquad \text{(A.7)}$$

This result indicates that $w_2$ is the probability of changing state upon the second pulse because from probabilistic considerations one has $\rho_{22}(t_3) = w_1\,(1 - w_2) + (1 - w_1)\,w_2$ which corresponds to the rhs of Eq. (A.7). It is worth emphasizing that $\langle w_1 w_2 \rangle \neq \langle w_1 \rangle \langle w_2 \rangle$.

# B Average dephasing time $\langle|\theta|\rangle$

In this Appendix the expression

$$\langle|\theta|\rangle = \left\langle \left| \int_0^{t_{12}} u(t)\mathrm{d}t - \int_{t_{12}}^{2t_{12}} u(t)\mathrm{d}t \right| \right\rangle \tag{B.1}$$

is evaluated where the average is taken over the temporal realizations of $u(t)$ and over the excitation probability dependent on the offset $\Delta$. The notation follows the one used in the main text. As outlined there, $u(t)$ changes states stochastically because of the two excitation pulses with probabilities $\mathrm{w}_1$ and $\mathrm{w}_2$ and because of the spontaneous decay according to the rate $\gamma_1$. The average over the offset and the temporal realization can be taken independently. One finds

$$\langle|\theta|\rangle = \langle \mathrm{w}_1(1-w_2)\rangle F_1 + \langle (1-w_1)w_2\rangle F_2 + \langle w_1 w_2\rangle F_3 \ , \tag{B.2}$$

where the first term on the rhs arises when the ion under consideration is excited by the first pulse and does not change state as a result of the second pulse. The second term denotes the contribution of an ion which was not excited by the first pulse, however, is excited by the second pulse. The third term accounts for possible changes of state by both pulses. The prefactors are conditional probabilities of occurrence with the averages taken over the offset frequency.

$F_1$, $F_2$, and $F_3$ are calculated from averages over particular temporal realizations of $u(t)$. For $F_1$ this results in

$$F_1 = \gamma_1 \left[ \int_0^{t_{12}} x e^{-x\gamma_1}\mathrm{d}x + \int_{t_{12}}^{2t_{12}} (2t_{12}-x) e^{-x\gamma_1}\mathrm{d}x \right] \ , \tag{B.3}$$

where the first and second term on the rhs are the contributions when the excitation decays spontaneously in the time interval $[0, t_{12}]$ and $[t_{12}, 2t_{12}]$, respectively.

The integration is straight forward and yields

$$F_1 = \gamma_1^{-1}\left(1 - e^{-t_{12}\gamma_1}\right)^2 \ . \tag{B.4}$$

For $F_2$ this gives

$$F_2 = \gamma_1 \left[ \int_{t_{12}}^{2t_{12}} (x - t_{12}) e^{-(x-t_{12})\gamma_1} \mathrm{d}x + t_{12} \int_{2t_{12}}^{\infty} e^{-(x-t_{12})\gamma_1} \mathrm{d}x \right] \ , \tag{B.5}$$

where the first term arises when spontaneous decays occur in the interval $[t_{12}, 2t_{12}]$ and the second term when there is no such decay. Integration gives

$$F_2 = \gamma_1^{-1}\left(1 - e^{-t_{12}\gamma_1}\right) \ . \tag{B.6}$$

The most involved term is $F_3$ being

$$\begin{aligned} F_3 \ = \ & \gamma_1^2 \int_0^{t_{12}} \mathrm{d}x \int_{t_{12}}^{2t_{12}} \mathrm{d}y |x - (y - t_{12})| e^{-[x+(y-t_{12})]\gamma_1} + \\ & + \gamma_1^2 \int_0^{t_{12}} \mathrm{d}x \int_{2t_{12}}^{\infty} \mathrm{d}y |x - t_{12}| e^{-[x+(y-t_{12})]\gamma_1} + \gamma_1 t_{12} \int_{t_{12}}^{\infty} e^{-x\gamma_1} \mathrm{d}x \ , \end{aligned} \tag{B.7}$$

where the first term arises when a spontaneous decay occurs in the intervals $[0, t_{12}]$ and $[t_{12}, 2t_{12}]$, the second when a spontaneous decay takes place only in the interval $[0, t_{12}]$ and the third when there is no such an event. Integration yields

$$F_3 = F_2 = \gamma_1^{-1}\left(1 - e^{-t_{12}\gamma_1}\right) \ . \tag{B.8}$$

Inserting Eqs. (B.3) and (B.8) into Eq. (B.2) one obtains

$$\langle|\theta|\rangle \ = \ \langle \mathrm{w}_1(1 - \mathrm{w}_2)\rangle \gamma_1^{-1}\left(1 - e^{-t_{12}\gamma_1}\right)^2 + \langle \mathrm{w}_2\rangle \gamma_1^{-1}\left(1 - e^{-t_{12}\gamma_1}\right) \ . \tag{B.9}$$

For the two limiting cases $\langle \mathrm{w}_2\rangle \to 0$ and $\langle \mathrm{w}_1\rangle \to 0$ Eq. (B.9) corresponds to Eq. (22) of Ref. [36] with $t_s = 0$ and $t_s = t_{12}$, respectively. For weak pulses $\langle \mathrm{w}_1 \mathrm{w}_2\rangle$ is negligible if compared with $\langle \mathrm{w}_1\rangle$ so that the weight factor of the first term in Eq. (B.9) can be approximated by $\langle \mathrm{w}_1\rangle$.

Making use of Eq. (7.8) one finds that for weak pulses

$$\langle|\theta|\rangle \simeq c\gamma_1^{-1}\mathcal{T}_1\left(1-e^{-t_{12}\gamma_1}\right)^2 + c\gamma_1^{-1}\mathcal{T}_2\left(1-e^{-t_{12}\gamma_1}\right) , \tag{B.10}$$

which is considered in Eq. (7.18) of the main text. For $\gamma_1 t_{12} \ll 1$, Eq. (B.9) is approximated by

$$\langle|\theta|\rangle \simeq \langle w_2\rangle\, t_{12} \simeq c\mathcal{T}_2 t_{12} , \tag{B.11}$$

where the latter equality applies for a weak second pulse. This expression is used in Eq. (7.19) of the main text.

# C EFS by off-diagonal interactions

In this Appendix, the rhs of Eq. (7.21) of the main text is analyzed which here is denoted as $\Phi$ and reads

$$\Phi = p\sum_k{}' \left\{ 1 - \left\langle \cos\left[ -i\theta_k \sigma_{jk} \left( \sqrt{J_{jk}^2 + (\Delta_{jk}/2)^2} - |\Delta_{jk}/2| \right) \right] \right\rangle_{\theta_k, \Delta_{jk}, \Omega_k} \right\}, \quad \text{(C.1)}$$

where the average is taken over the realizations of $\theta_k$ and over the distribution of $\Delta_{jk}$. First the case is considered, where the scrambler excitations are shifted by a fixed frequency $\Delta\omega_s$ so that $\Delta_{jk} = |\Delta\omega_s|$. In the continuum approximation Eq. (C.1) writes

$$\Phi \simeq 4\pi\rho_0 p \left\langle \int_0^\infty \mathrm{d}r\, r^2 \left\{ 1 - \right. \right. \quad \text{(C.2)}$$
$$\left. \left. - \cos\left[ \theta \left( \sqrt{J_0^2 \kappa^2(\Omega)(r_0/r)^6 + (\Delta\omega_s/2)^2} - |\Delta\omega_s/2| \right) \right] \right\} \right\rangle \theta, \Omega \,,$$

where $\rho_0$ and $p$ have the meaning of Section 7.3.3 and the average is taken over $\theta$ and the angular configuration indicated by $\Omega$. Changing variables ($r^{-3} \to x$) the integration by parts gives

$$\Phi = \frac{4\pi}{3} r_0^3 \rho_0 p J_0^2 \left\langle |\theta| \kappa^2(\Omega) \cdot \right. \quad \text{(C.3)}$$
$$\left. \cdot \int_0^\infty \frac{\sin\left( |\theta| \left( \sqrt{J_0^2 \kappa^2(\Omega) x^2 + (\Delta\omega_s/2)^2} - |\Delta\omega_s/2| \right) \right)}{\sqrt{J_0^2 \kappa^2(\Omega) x^2 + (\Delta\omega_s)^2}} \,\mathrm{d}x \right\rangle_{\theta,\Omega} .$$

Substituting $y = \sqrt{J_0^2 \kappa^2(\Omega) x^2 + (\Delta\omega_s/2)^2} - |\Delta\omega_s/2|$ Eq. (C.3) reads

$$\Phi = \frac{4\pi}{3} r_0^3 \rho_0 p J_0 \langle |\kappa| \rangle \left\langle |\theta| \int_0^\infty \mathrm{d}y \frac{1}{\sqrt{y(y + |\Delta\omega_s|)}} \sin(|\theta| y) \right\rangle_\theta . \quad \text{(C.4)}$$

Integration gives [172]

$$\Phi = \frac{4\pi}{3} r_0^3 \rho_0 p J_0 \langle|\kappa|\rangle \left\langle |\theta| \, \Im \left\{ e^{-i|\theta||\Delta\omega_s/2|} \mathrm{K}_0(-i|\theta||\Delta\omega_s/2|) \right\} \right\rangle_\theta , \qquad \text{(C.5)}$$

where $\mathrm{K}_0(x)$ is the zeroth order Bessel function of third kind and $\Im$ denotes the imaginary part.

Considering the asymptotic behavior [173]

$$\Im \left\{ e^{-ix} \mathrm{K}_0(-ix) \right\} \simeq \begin{cases} \pi/2 & , \; x \ll 1 \\ \sqrt{\dfrac{\pi}{4x}} & , \; x \gg 1 \end{cases} , \qquad \text{(C.6)}$$

one obtains

$$\Phi \simeq \begin{cases} (2\pi^2/3) r_0^3 \rho_0 p J_0 \langle|\kappa|\rangle \langle|\theta|\rangle & , \; \langle|\theta|\rangle |\Delta\omega_s| \ll 1 \\ (2\pi)^{3/2} (1/3) r_0^3 \rho_0 p J_0 \left\langle \sqrt{|\theta|} \right\rangle / \sqrt{|\Delta\omega_s|} & , \; \langle|\theta|\rangle |\Delta\omega_s| \gg 1. \end{cases} , \qquad \text{(C.7)}$$

Next , the case is studied where the $\Delta_{jk}$ are uniformly distributed random variables restricted to the range $[-\Delta_{\max}, \Delta_{\max}]$. In this case, Eq. (C.2) takes the form

$$\Phi \simeq \frac{4\pi\rho_0 p}{\Delta_{\max}} \left\langle \int_0^{\Delta_{\max}} d\Delta \int_0^{\infty} \mathrm{d}r \; r^2 N(\theta, \Omega, \Delta) \right\rangle_{\theta,\Omega} , \qquad \text{(C.8)}$$

where

$$N(\theta, \Omega, \Delta) = \left\{ 1 - \cos \left[ \theta \left( \sqrt{J_0^2 \kappa^2(\Omega)(r_0/r)^6 + (\Delta/2)^2} - (\Delta/2) \right) \right] \right\} .$$

Making use of Eqs. (C.3)-(C.5) $\Phi$ becomes

$$\Phi = \frac{4\pi}{3\Delta_{\max}} r_0^3 \rho_0 p J_0 \langle|\kappa|\rangle \left\langle |\theta| \int_0^{\Delta_{\max}} \mathrm{d}\Delta \; \Im \left\{ e^{-i|\theta|\Delta/2} \mathrm{K}_0(-i|\theta|\Delta/2) \right\} \right\rangle_\theta . \qquad \text{(C.9)}$$

By numerical inspection it is noticed that the approximation

$$\Im\left\{e^{-ix}\mathrm{K}_0(-ix)\right\} \simeq \frac{\pi}{2\sqrt{1+\pi x}}\,, \tag{C.10}$$

reproduces the exact result reasonably for $x \in [0,\infty]$ with a maximum relative deviation of less than 4 %. By substituting Eq. (C.10) into Eq. (C.9) one obtains

$$\begin{aligned}\Phi &\simeq \frac{2\pi^2}{3\Delta_{\max}} r_0^3 \rho_0 p J_0 \left\langle|\kappa|\right\rangle \left\langle |\theta| \int_0^{\Delta_{\max}} \frac{\mathrm{d}\Delta}{\sqrt{1+\pi\Delta|\theta|/2}} \right\rangle_\theta \\ &= \frac{8\pi}{3\Delta_{\max}} r_0^3 \rho_0 p J_0 \left\langle|\kappa|\right\rangle \left( \left\langle \sqrt{1+\pi\Delta_{\max}|\theta|/2} \right\rangle_\theta - 1 \right)\,. \end{aligned} \tag{C.11}$$

Taking into account that $\theta$ is not broadly distributed, expression (C.11) can be approximated by the limiting cases

$$\Phi \simeq \begin{cases} (2\pi^2/3) r_0^3 \rho_0 p J_0 \left\langle|\kappa|\right\rangle \left\langle|\theta|\right\rangle & , \ \left\langle|\theta|\right\rangle \Delta_{\max} \ll 1 \\ (2\pi)^{3/2} (1/3) r_0^3 \rho_0 p J_0 \left\langle\sqrt{|\theta|}\right\rangle / \sqrt{\Delta_{\max}} & , \ \left\langle|\theta|\right\rangle \Delta_{\max} \gg 1 \end{cases}\,, \tag{C.12}$$

which are considered in Eq. (7.23) of the main text.

# D Number of spontaneous decay events

In this Appendix the number $\langle N \rangle$ of spontaneous decays of electronic excitations in the time $2t_{12}$ is considered. These decays may generate non-equilibrium phonons. Here, the scheme of Appendix B is followed, thus $\langle N \rangle$ is described in terms of the excitation probability $w_1$ by the first pulse and by the probability $w_2$ of changing state upon the second pulse and of the decay rate $\gamma_1$.

The probability for one spontaneous decay can be given as the sum of three terms

$$\begin{aligned} P_1 &= \langle w_1 (1 - w_2) \rangle \left(1 - e^{-2\gamma_1 t_{12}}\right) + \langle (1 - w_1) w_2 \rangle \left(1 - e^{-\gamma_1 t_{12}}\right) + \\ &\quad + \langle w_1 w_2 \rangle \left(1 - e^{-\gamma_1 t_{12}}\right) e^{-\gamma_1 t_{12}} \end{aligned} \tag{D.1}$$

where the first term denotes the probability that an excitation is induced by the first pulse, that the state is not altered by the second pulse and a spontaneous decay occurs in the period between the first pulse and the echo. The second term is the probability that an excitation is induced only by the second pulse followed by a decay in the period between the second pulse and the echo. The third term denotes the probability that an excitation is induced by the first pulse, that a spontaneous decay occurs in the inter-pulse period followed again by an excitation without further decay. Analogously, for the probability of two decay events one finds

$$\langle P_2 \rangle = \langle w_1 w_2 \rangle \left(1 - e^{-\gamma_1 t_{12}}\right)^2 , \tag{D.2}$$

which is the probability that excitations are induced by the first and second pulse and decays occur in the inter-pulse period and in the period between the second pulse and the echo. The expectation value of the number of decay events thus is

$$\begin{aligned} \langle N \rangle = \langle P_1 \rangle + 2\langle P_2 \rangle &= \langle w_1 \rangle \left(1 - e^{-2\gamma_1 t_{12}}\right) + \langle w_2 (1 - w_1) \rangle \left(1 - e^{-\gamma_1 t_{12}}\right) - \\ &\quad - 2 \langle w_1 w_2 \rangle \left(1 - e^{-\gamma_1 t_{12}}\right) e^{-\gamma_1 t_{12}} . \end{aligned} \tag{D.3}$$

For either $\langle w_1 \rangle = 0$ or $\langle w_2 \rangle = 0$ the two trivial cases are recovered, where either only the first or the second pulse induces an excitation. For small $\langle w_1 \rangle$ and $\langle w_2 \rangle$

values Eq. (D.3) reduces to

$$\langle N \rangle \simeq \langle \mathrm{w}_1 \rangle \left(1 - e^{-2\gamma_1 t_{12}}\right) + \langle \mathrm{w}_2 \rangle \left(1 - e^{-\gamma_1 t_{12}}\right) , \tag{D.4}$$

which was considered in Eq. (7.30) of the main text. For $\gamma_1 t_{12} \ll 1$ Eq. (D.3) can be approximated by

$$\langle N \rangle \simeq \left[\left(1 - e^{-2c\mathcal{T}_1}\right) + \frac{1}{2}\left(1 - e^{-2c\mathcal{T}_2}\right)\right] \gamma_1 t_{12} . \tag{D.5}$$

Finally for weak pulses and for $\gamma_1 t_{12} \ll 1$ one finds

$$\langle N \rangle \simeq (2\mathcal{T}_1 + \mathcal{T}_2)\, c\gamma_1 t_{12} , \tag{D.6}$$

which is considered in Eq. (7.31) of the main text.

Leer - Vide - Empty

# Bibliography


[1] T. W. Mossberg, "Time-domain frequency-selective data storage", *Opt. Lett.* **7**(2), pp. 77 (1982).

[2] D. Psaltis and F. Mok, "Holographic memories", *Sci. Am.* **273**(5), pp. 52 (1995).

[3] B. H. Plagemann, F. R. Graf, S. B. Altner, A. Renn, and U. P. Wild, "Exploring the limits of data storage using persistent spectral hole burning: Recording of 12'000 holographic images", *Appl. Phys. B* **66**(1), pp. 67 (1998).

[4] For homepages of start up companies in the field of holographic data storage see for example: *http://www.holoplex.com* or *http://www.templex.com.*

[5] P. I. Bunyk, A. Oliva, V. K. Semenov, M. Bhushan, K. K. Likharev, J. E. Lukens, M. B. Ketchen, and W. H. Mallison, "High-speed single-flux-quantum cicuit using planarized niobium-trilayer josephson junction technology", *J. Appl. Phys.* **66**(646) (1995).

[6] Walter Ferri, *Diffraction Properties of Time-and-Space-Domain Volume Holograms in Frequency-Selective Materials studied with ultrashort Pulses*, PhD thesis ETH No. 11892, Zürich (1996).

[7] W. E. Moerner, editor, *Persistent Spectral hole-burning: Science and Applications*, Springer-Verlag Berlin (1988).

[8] R. M. Macfarlane and R. M. Shelby, *Spectroscopy of Solids Containing Rare-Earth Ions* chapter 3, Elsevier Science North-Holland,Amsterdam (1987), and references therein.

[9] M. Mitsunaga, "Time-domain optical data storage by photon echo", *Opt. and Quantum Elect.* **24**, pp. 1137 (1992).

[10] T. W. Mossberg, "Swept-carrier time domain optical memory", *Opt. Lett.* **17**, pp. 535 (1992).

[11] A. Renn and U. P. Wild, "Spectral hole burning and hologram storage", *Appl. Opt.* **26**, pp. 4040 (1987).

[12] U. P. Wild and A. Renn, "Molecular computing: A review", *J. Mol. Elect.* **7**, pp. 1 (1990).

[13] E. S. Maniloff, F. R. Graf, and S. Bernet, "Frequency de-multiplexing", Yearly report SHB subgroup ETH Zürich (1994), Originally proposed for a patent.

[14] F. R. Graf, B. H. Plagemann, E. S. Maniloff, S. B. Altner, A. Renn, and U. P. Wild, "Data compression in frequency-selective materials using frequency-swept excitation pulses", *Opt. Lett.* **21**(4), pp. 284 (1996).

[15] F. R. Graf, B. H. Plagemann, E. S. Maniloff, S. B. Altner, A. Renn, and U. P. Wild, "Data compression in $Pr^{3+} : Y_2SiO_5$ by frequency-swept pulses", *J. Lumin.* **66**(67), pp. 70 (1996).

[16] Bernd Plagemann, *Untersuchung von Grenzen und Möglichkeiten optischer Datenspeicher in frequenzselektiven Materialien*, PhD thesis ETH , Zürich (1998).

[17] J. Becquerel, "Untersuchungen über die magneto-optischen Erscheinungen in Kristallen", *Phys. Zeitschrift* **8**(19), pp. 632 (1908).

[18] N. A. Kurnit, I. D. Abella, and S. R. Hartmann, "Photon echoes", *Phys. Rev. Lett.* **13**, pp. 567 (1964).

[19] I. D. Abella, N. A. Kurnit, and S. R. Hartmann, "Photon echos", *Phys. Rev.* **1411**, pp. 391 (1966).

[20] L. E. Erickson, "The nuclear quadrupole interaction in $Pr^{3+} : LaF_3$. An optical-rf double resonance measurement of the ground electronic state", *Opt. Comm.* **21**(1), pp. 147 (1977).

[21] R. W. Equall, Y. Sun, R. L. Cone, and R. M. Macfarlane, "Ultraslow optical dephasing in $Eu^{3+} : Y_2SiO_5$", *Phys. Rev. Lett.* **72**(14), pp. 2179 (1994).

[22] S. Hüfner, *Optical Spectra of Transparent Rare Earth Compounds*, Academic Press N.Y. (1978).

[23] S. Mukamel, *Principles of Nonlinear Optical Spectroscopy*, Oxford University Press N.Y. (1995).

[24] R. G. DeVoe, A. Wokaun, S. C. Rand, and R. G. Brewer, "Monte Carlo theory of optical dephasing in $Pr^{3+} : LaF_3$", *Phys. Rev. B* **23**(7), pp. 3125 (1981).

[25] J. Huang, J. M. Zhang, A. Lezama, and T. W. Mossberg, "Excess dephasing in photon-echo experiments arising from excitation-induced electronic level shifts", *Phys. Rev. Lett.* **63**, pp. 78 (1989).

[26] R. Orbach, "Spin lattice relaxation in rare earth salts", *Proc. Roy. Soc. A* **264**, pp. 485 (1961).

[27] C. B. Harris, "The origin of optical dephasing times and line shape functions for electronic transitions to localized and delocalized states in solids", *J. Chem. Phys.* **67**(12), pp. 5607 (1978).

[28] A. Abragam and B. Bleaney, *Electron Paramagnetic Resonance of Transition Ions*, Dover Press N.Y. (1986).

[29] M. A. Teplov, "Magnetic resonance on $^{141}Pr$ nuclei in $Pr_2(SO_4)_3 \cdot 8H_2O$ single crystal", *Sov. Phys. JETP* **26**(5), pp. 872 (1968).

[30] P. W. Anderson, B. L. Halperin, and C. M. Varma, "Anomaleous low-temperature properties of glasses and spin glasses", *The Phil. Mag.* **25**, pp. 1 (1971).

[31] D. L. Huber, "Analysis of a stochastic model for the optical linewidths and photon-echo decays of impurities in glasses", *J. Lumin.* **36**, pp. 307 (1987).

[32] A. Suarez and R. Silbey, "Low temperature dynamics in glasses and the stochastic sudden-jump model", *Chem. Phy. Lett.* **218**, pp. 445 (1994).

[33] R.Orbach and L.A. Vredevoe, "The attenuation of high frequency phonons at low temperatures", *Physics* **1**(2), pp. 91 (1964).

[34] P. G. Klemens, "Decay of high-frequency longitudinal phonons", *J. Appl. Phys.* **38**, pp. 4573 (1967).

[35] R. Baumgartner, M. Engelhardt, and K. F. Renk, "Spontaneous decay of high-frequency phonons in $CaF_2$", *Phys. Rev. Lett.* **47**(19), pp. 1403 (1981).

[36] S. Altner, G. Zumofen, U. P. Wild, and M. Mitsunaga, "Photon echo attenuation in rare-earth-ion-doped crystals", *Phys. Rev. B* **54**(24), pp. 17493 (1996).

[37] A. S. Davydov, *Theory of Molecular Excitons*, Plenum Press N.Y. (1971).

[38] J. L. Skinner, H. C. Andersen, and M. D. Fayer, "Theory of photon echoes from a pair of coupled two level systems: Impurity dimers and energy transfer in molecular crystals", *J. Chem. Phys.* **75**(1), pp. 3195 (1981).

[39] T. Basché, W. E. Moerner, M. Orrit, and U. P. Wild, editors, *Single-molecule optical detection, imaging and spectroscopy*, VCH Berlin (1996), and references therein.

[40] G. H. Dieke and H. M. Crosswhite, "The spectra of the doubly and triply ionized rare-earth", *Appl. Opt.* **2**, pp. 681 (1963).

[41] B. A. Maksimov, Yu. A. Kharitonov, V. V. Illyukin, and N. B. Belov, "Crystal structure of the y-oxysilicate $Y_2(SiO_4)O$", *Sov. Phys. Dokl.* **13**(12), pp. 1188 (1969).

[42] R. W. Equall, R. L. Cone, and R. M. Macfarlane, "Homogeneous broadening and hyperfine structure of optical transitions in $Pr^{3+} : Y_2SiO_5$", *Phys. Rev. B* **52**(6), pp. 3963 (1995).

[43] X. A. Shen and R. Kachru, "$^7F_0 - {}^5D_1$ transition in $Y_2SiO_5$", *J. Opt. Soc. Am. B* **11**(4), pp. 591 (1994).

[44] R. M. Macfarlane, D. P. Burum, and R. M. Shelby, "New determination of the nuclear magnetic moment of $^{141}Pr$", *Phys. Rev. Lett.* **49**(9) (1982).

[45] J. M. Baker and F. I. B. Williams, "Electron nulcear double resonance of the divalent europium ion", *Proc. R. Soc. London Series A* **267**, pp. 283 (1962).

[46] R. J. Elliott, "Theory of nuclear magnetic resonance in $Eu^{3+}$", *Proc. Phys. Soc. B* **70**, pp. 119 (1957).

[47] L. Mandel and E.Wolf, *Optical Coherence and Quantum Optics*, Cambridge Press N.Y. (1995).

[48] R. G. Brewer and E. L. Hahn, "Coherent Raman beats", *Phys. Rev. A* **8**(1), pp. 464 (1973).

[49] T. P. Das and E. L. Hahn, *Nuclear quadrupole resonance spectroscopy*, Accademic Press N.Y. (1958).

[50] M. Mitsunaga, E. S. Kintzer, and R. G. Brewer, "Raman heterodyne interference of inequivalent nuclear sites", *Phys. Rev. Lett.* **52**(17), pp. 1484 (1984).

[51] K. Holliday, M. Croci, E. Vauthey, and U. P. Wild, "Spectral hole burning and holography in an $Y_2SiO_5 : Pr^{3+}$ crystal", *Phys. Rev. B* **47**(22), pp. 14741 (1993).

[52] T. Blasberg, *Coherent Raman Scattering for Optical Detection of NMR in* $Pr^{3+} : YAlO_3$, PhD thesis ETH No. 11027, Zürich (1995).

[53] Stefan Altner, *Hochauflösende Laserspektroskopie an Lanthanidionen in Orthosilikatkristallen*, PhD thesis ETH No. 11418, Zürich (1996).

[54] T. Plakhotnik, E. A. Donley, and Urs P. Wild, "Single-molecule spectroscopy", *Ann. Rev. Phys. Chem.* **48**, pp. 181–212 (1997).

[55] N. Bloembergen, E.M. Purcell, and R.V. Pound, "Relaxation effects in nuclear magnetic resonance absorption", *Phys. Rev.* **73**(679) (1948).

[56] A. Szabo, "Observation of hole burning and cross relaxation effects in ruby", *Phys. Rev. B.* **11**(11), pp. 4512 (1975).

[57] B.M. Kharlamov, R.I. Personov, and L.A. Bykovskay, "Stable gap in absorption spectra of solid solutions of organic molecules by laser irradiation", *Opt. Comm.* **12**, pp. 1191 (1974).

[58] A.A. Ghorokhovskii, R.K. Kaarli, and L.A. Rebane, "Hole burning in the contour of a pure electronic line in a Shpol'skii system", *JETP Lett.* **20**, pp. 216 (1974).

[59] W. H. Hesselink and D. W. Wiersma, *Theory and experimental aspects of photon echoes in molecular solids* chapter 6, , p. 249, North-Holland Amsterdam (1983).

[60] K. Blum, *Density Matrix Theory and Applications*, Plenum Press N.Y. (1981).

[61] L. Allen and J. H. Eberly, *Optical Resonance and Two-Level Atoms*, John Wiley N.Y. (1975).

[62] A. G. Redfield, "On the theory of relaxation", *IBM J. Res. Dev.* **1**, pp. 19 (1957).

[63] A. Abragam, *The Principles of Nuclear Magnetism*, Int. series of monographs on physics. Oxford Press Oxford (1961).

[64] A. G. Redfield, "The theory of relaxation processes", *Adv. Magn. Res.* **1**, pp. 1 (1965).

[65] M. Gross and S. Haroche, "Superradiance: An essay of the theory of collective sponteneous emission", *Phys. Rep.* **93**(1), pp. 301 (1982).

[66] R. P. Feynman, F. L. Vernon, and R. W. Hellwarth, "Geometrical representation of the Schrödinger equation for solving Maser problems", *J. Appl. Phys.* **28**(1), pp. 49 (1957).

[67] F. Bloch, "Nuclear induction", *Phys. Rev* **70**(7), pp. 460 (1946).

[68] I.I. Rabi, N. F. Ramsey, and J. Schwinger, "Use of rotating coordinates in magnetic resonance problems", *Rev. Modern Physics* **26**(2), pp. 167 (1954).

[69] H. Primas, *Vorlesungsnotizen PC VIII*, ETH Zürich (1992).

[70] A. Schenzle, N. C. Wong, and R. G. Brewer, "Theorem on coherent transients", *Phys. Rev. A* **22**(2), pp. 653 (1980).

[71] M. Mitsunaga and R. G. Brewer, "Generalized perturbation theory of coherent optical emission", *Phys. Rev. A* **32**(3), pp. 1605 (1985).

[72] M. Kunitomo and M. Kaburaghi, "General study of two-pulse echoes", *Phys. Rev. A* **29**(1), pp. 207 (1984).

[73] Y. Y. Asadullin, "Formation mechanisms and properties of photon echoes in crystals", *Laser Phys.* **2**(6), pp. 965 (1992).

[74] J. R. Klauder and P. W. Anderson, "Spectral diffusion decay in spin resonance experiments", *Phys. Rev.* **125**(3), pp. 912 (1962).

[75] V. S. Lethokov, *High-Resolution Laser Spectroscopy*, Topics in Applied Physics. Springer Berlin (1976).

[76] E. Maniloff, F. Graf, H. Gygax, A. Renn, and U. P. Wild, "Power broadening of spectral holewidth in an optically thick sample", *Chem. Phys* **193**, pp. 173 (1995).

[77] S. L. McCall and E. L. Hahn, "Self-induced transparency by pulsed coherent light", *Phys. Rev. Lett.* **18**(21), pp. 908 (1967).

[78] S. L. McCall and E. L. Hahn, "Self-induced transparency", *Phys. Rev.* **183**(2), pp. 457 (1969).

[79] R. E. Slusher and H. M. Gibbs, "Self-induced transparency in atomic rubidium", *Phys. Rev. A* **5**(4), pp. 1634 (1972).

[80] G. Zumofen, F. R. Graf, A. Renn, and U. P. Wild, "Self-induced transparency in an optically thick $Pr^{3+} : Y_2SiO_5$ crystal", to be published (1998).

[81] R. R. Ernst, G. Bodenhausen, and A. Wokaun, *Principles of Nuclear Magnetic Resonance in One and Two Dimensions*, Int. series of monographs on chemistry 14. Oxford Press N.Y. 6 edition (1997).

[82] K. Schneider, P. Kramper, S. Schiller, and J. Mlynek, "Towards an optical synthesizer: A single frequency parametric oscillator using periodically poled $LiNbO_3$", *Opt. Lett.* **22**(17), pp. 1293 (1997).

[83] R. W. Drever, J. L. Hall, F. V. Kowalski, J. Hough, G. M. Ford, A. J. Munley, and H. Ward, "Laser phase and frequency stabilization using and optical resonator", *Appl. Phys. B* **31**, pp. 97 (1983).

[84] R. V. Pound, "Electronic frequency stabilization of microwave oscillators", *Rev. Sc. Instr.* **17**(11), pp. 490 (1946).

[85] M. Houssin, M. Jardino, B. Gely, and M. Desaintfuscien, "Design and performance of a few-kilohertz-linewidth dye laser stabilized by reflection in an optical resonator", *Opt. Lett.* **13**(10), pp. 823 (1988).

[86] G. C. Bjorklund, M. D. Levenson, W. Length, and C. Ortiz, "Frequency modulation spectroscopy", *Appl. Phys. B* **32**, pp. 145 (1983).

[87] S. Seel, R. Storz, G. Ruoso, J. Mlynek, and S. Schiller, "Cryogenic optical resonators: a new tool for laser frequency stabilization at the 1Hz level", *Phys. Rev. Lett.* **78**(25), pp. 4741 (1997).

[88] N. Manson and M. Sellars, "Laser stabilizer system", Technical report Inst. Adv. Studies Australian National University Camberra (1993).

[89] A. Brillet and J. L. Hall, "Improved laser test of the isotropy of space", *Phys. Rev. Lett.* **42**, pp. 549 (1979).

[90] J. E. Faller, P. L. Bender, J. L. Hall, D. Hils, and M. A. Vincent, *In Kilometric Optical Arrays in Space*, European Space Agency Paris (1985).

[91] M. Roberts P. Taylor, G. P. Barwood, H. A. Klein, and W. R. C. Rowley, "Observation of an electric octupole transition in a single ion", *Phys. Rev. Lett.* **78**, pp. 1876 (1997).

[92] R. Yano, M. Mitsunaga, and N. Uesugi, "Ultralong optical dephasing in $Eu^{3+} : Y_2SiO_5$", *Opt. Lett.* **16**(23), pp. 1884 (1991).

[93] C. Salomon, D. Hils, and J.L. Hall, "Laser stabilization at the millihertz level", *J. Opt. Soc. Am. B* **5**(8), pp. 1576 (1988).

[94] Hansruedi Gygax, *Von zeitaufgelöster Fluoresenzspektroskopie zum Photon-Echo-Experiment*, PhD thesis ETH No. 10374, Zürich (1993).

[95] Werner Graff, *Spektrale Daten im Multi-Giga-Byte-Bereich*, PhD thesis ETH No. 12059, Zürich (1997).

[96] D. J. Berkeland, J. D. Miller, J. C. Berquist, W. M. Itano, and D. J. Wineland, "Laser-cooled mercury ion frequency standard", *Phys. Rev. Lett.* **80**(10), pp. 2089 (1998).

[97] X. A. Shen, A. Nguyen, J. Perry, D. Huestis, and R. Kachru, "Time-domain holographic digital memory", *Science* **278**, pp. 96 (1997).

[98] H. Kogelnik, "Coupled wave theory for thick hologram gratings", *Bell Sys. Tech. J.* **48**, pp. 2909 (1969).

[99] A. J. Meixner, A. Renn, and U. P. Wild, "Spectral hole-burning and holography. I. Transmission and holographic detection of spectral holes", *J. Chem. Phys.* **91**(11), pp. 6728 (1989).

[100] S. Bernet, S. Altner, F. Graf, E. Maniloff, A. Renn, and U. P. Wild, "FPS holograms in spectral hole-burning materials", *Appl. Opt.* **34**(22), pp. 4674 – 4684 (1995).

[101] H. de Vries and D. A. Wiersma, "Photophysical and photochemical molecular hole burning theory", *J. Chem. Phys* **72**, pp. 1851 (1980).

[102] A. J. Meixner, A. Renn, and U. P. Wild, "Spectral hole-burning and holography", *J. Lumin.* **45**, pp. 320 (1990).

[103] M. Mitsunaga, N. Uesugi, and K. Sugiyama, "Kilohertz-resolution pump-porbe spectroscopy in $Pr^{3+} : YAlO_3$.", *Opt. Lett.* **18**, pp. 1256 (193).

[104] M. J. Sellars, R. S. Meltzer, P. T. H. Fisk, and N. B. Manson, "Time-resolved ultranarrow optical hole burning of a crystalline solid: $Y_2O_3 : Eu^{3+}$", *J. Opt. Soc. Am. B* **11**(8), pp. 1468 (1994).

[105] J. A. Barnes, A. R. Chi, L. S. Cutler, D. J. Healey, D. B. Leeson, T. E. McGunigal, J. A. Mullen, W. L. Smith, R. L. Syndor, R. F. C. Vessot, and G. M. R. Winkler, *IEEE Trans. Instrum. Meas.* **20**, pp. 105 (1971).

[106] S. Altner, G. Zumofen, U. P. Wild, and M. Mitsunaga, "Dephasing-rephasing balancing by excitation induced frequency shifts", *Phys. Rev. Lett.* **76**, pp. 1747 (1996).

[107] G. K. Liu and R. L. Cone, "Laser-induced instantaneous spectral diffusion in $Tb^{3+}$ compounds as observed in photon echo experiments", *Phys. Rev. B* **41**(10), pp. 6193 (1990).

[108] M. Mitsunaga, E. S. Kintzer, and R. G. Brewer, "Raman heterodyne interference: Observations and analytic theory", *Phys. Rev. B* **31**(11), pp. 6947 (1984).

[109] E. S. Kintzer, M. Mitsunaga, and R. G. Brewer, "Raman heterodyne interference: Symmetry analysis", *Phys. Rev. B* **31**(11), pp. 6985 (1985).

[110] A. J. Silversmith, A. P. Radlinski, and N. B. Manson, "Optical study of hyperfine coupling in the $^7F_0$ and $^5D_0$ states of two $Eu^{3+}$ centers in $CaF_2$ and $CdF_2$", *Phys. Rev. B* **34**(11), pp. 7554 (1986).

[111] R. M. Macfarlane and R. M. Shelby, "Measurement of the nuclear and electronic Zeeman effects using optical hole-burning spectroscopy", *Opt.Lett.* **6**, pp. 96 (1981).

[112] A. Meixner, A. Renn, S. E. Bucher, and U. P. Wild, "Spectral hole burning in glasses and polymer films: The Stark effect", *J. Phys. Chem* **90**, pp. 6777 (1986).

[113] L. Kador, D. Haarer, and R. Personov, "Stark effect of polar and unpolar dye molecules in amorphous hosts, studied via persistent spectral hole burning", *J. Chem. Phys.* **86**, pp. 5300 (1987).

[114] A. J. Meixner, *Spektrales Lochbrennen. Entwicklung der Holographischen Detektionsmethode. Stark-Effekt Experimente an Spektralen Löchern*, PhD thesis ETH No. 8726 Zürich (1988).

[115] U.P. Wild, F. Güttler, M. Pirotta, and A. Renn, "Single molecule spectroscopy: Stark effect of pentacene in p-terphenyl", *Chem. Phy. Lett.* **193**(6), pp. 451 (1992).

[116] M. Pirotta, A. Renn, and U. P. Wild, "Stark effect measurements on single perylene molecules", *Helv.Phys.Acta* **69**, pp. 7 (1996).

[117] R. M. Shelby and R. M. Macfarlane, "Measurement of the pseudo-Stark effect in $Pr^{3+}:LaF_3$ using population hole burning and optical free-induction decay", *Opt Comm.* **27**(3), pp. 399 (1978).

[118] J. P. Chaminade, R. M. Macfarlane, F. Ramaz, and J. C. Vial, "High resolution laser spectroscopy of rare earth doped $CsCdBr_3$", *J. of Lumin.* **48**, pp. 531 (1991).

[119] Y. P. Wang and R. S. Meltzer, "Modulation of photon-echo intensities by electric fields: Pseudo-Stark splittings in alexandrite and $YAlO_3 : Er^{3+}$", *Phys. Rev. B* **45**(17), pp. 10119 (1992).

[120] A. J. Meixner, C. M. Jefferson, and R. M. Macfarlane, "Measurement of the Stark effect with subhomogeneous linewidth", *Phys. Rev. B* **46**(10), pp. 5912 (1992).

[121] R. M. Macfarlane and A. J. Meixner, "Electric field-modulated photon echoes in $Pr^{3+} : YAlO_3$", *Opt. Lett.* **19**(3), pp. 987 (1994).

[122] V. N. Lisin, V. A. Zuikov, A. M. Shegeda, V. V. Samartsev, and B. M. Khabibullin, "Modulation of the photon echo polarization by an electric field: Pseudo-Stark splitting in $LaF_3 : Pr^{3+}$", *Laser Physics* **6**(1) (1996).

[123] F. R. Graf, B. H. Plagemann, A. Renn, U. P. Wild, and M. Mitsunaga, "Total dephasing-rephasing balancing in Stark-pulse modulated photon echoes", *Opt. Lett.* **22**(3), pp. 181 (1997).

[124] L. E. Erickson, "Hyperfine interaction in the lowest level of the level of the $^3H_4$ and $^1D_2$ states of the trivalent praesodymiunm in yttrium aluminum perovskite ($YAlO_3$)", *Phys. Rev. B* **19**(9), pp. 4412 (1979).

[125] L. E. Erickson, "Addendum to hyperfine interaction in the lowest level of the level of the $^3H_4$ and $^1D_2$ states of the trivalent praesodymiunm in yttrium aluminum perovskite ($YAlO_3$)", *Phys. Rev. B* **24**(9), pp. 5388 (1981).

[126] See for example in M. Hamermesh, *Group theory and its application to physical problems*, Dover Publ. N.Y. (1962).

[127] R. M. Macfarlane and R. M. Shelby, "Sub-kilohertz optical linewidth of the $^7F_0 - {}^5D_0$ transition in $Y_2O_3 : Eu^{3+}$", *Opt. Comm.* **39**(3), pp. 169 (1981).

[128] S. Altner, U. P. Wild, and M. Mtitsunaga, "Photon-echo demolition spectroscopy in $Eu^{3+}$:$Pr^{3+}$:$Nd^{3+}$:$Y_2SiO_5$", *Chem. Phys. Lett.* **237**, pp. 406 (1995).

[129] H. Gygax, A. Rebane, and U. P. Wild, "Stark effect in dye-doped polymers studied by photochemically accumulated photon echo", *J. Opt. Soc. Am. B* **10**(7), pp. 1149 (1993).

[130] H. Maier, R. Wunderlich, D. Haarer, B. M. Kharlamov, and S. G. Kulinov, "Optical detection of electric two level system dipoles in a polymeric glass", *Phys. Rev. Lett.* **74**(26), pp. 5252 (1995).

[131] Y. S. Bai and R. Kachru, "Non-equilibirum resonant-phonon-induced excess photon-echo decay", *Phys. Rev. B* **46**(21), pp. 13735 (1992).

[132] R. M. Macfarlane and R. S. Meltzer, "Optical dephasing of $Pr^{3+}$ ions by non-equilibrium phonons in $LaF_3$ and $YAlO_3$", *J. de Physique* **46** (1985).

[133] R. L. Cone and G. K. Liu, "Conference abstract", *Bull. Am. Phys. Soc.* **33**, pp. 676 (1988).

[134] Y. S. Bai and M. D. Fayer, "Optical dephasing in glasses: Theoretical comparison of the incoherent photon echo, accumulated grating echo, and two-pulse photon echo experiments", *Chem. Phys.* **128**, pp. 135 (1988).

[135] M. Mitsunaga, T. Takagahara, R. Yano, and N. Uesugi, "Excitation-induced frequency shift probed by stimulated photon echoes", *Phys. Rev. Lett.* **68**, pp. 3216 (1992).

[136] E. Geva and J. L. Skinner, "Theory of photon echoes and hole burning in low temperature glasses: How good are the standard approximations?", *J. Chem. Phys.* **107**, pp. 7630 (1997).

[137] D. E. MacCumber and M. D. Struge, "Linewidth and temperature shift of the R lines in Ruby", *J. Appl. Phys.* **34**, pp. 1682 (1963).

[138] W. M. Yen, W. C. Scott, and A.L. Schawlow, "Phonon-induced relaxation in excited optical states of trivalent Praseodynium in $LaF_3$", *Phys. Rev. A* **1**, pp. 271 (1964).

[139] W. R. Babbitt, A. Lezama, and T. W. Mossberg, "Optical dephasing, hyperfine struture and hyperfine relaxation associated with the 580.8 nm $^7F_0 - {}^5D_0$ transition of $Eu^{3+} : Y_2O_3$", *Phys. Rev. B* **39**, pp. 1987 (1989).

[140] G. P. Flinn, K. W. Jang, M. L. Jones, R.. S. Meltzer, and R. M. Macfarlane, "Sample-dependent optical dephasing in bulk crystalline samples of $Y_2O_3 : Eu^{3+}$", *Phys. Rev. B* **49**(9), pp. 5821 (1994).

[141] P. W. Anderson and P. R. Weiss, "Exchange narrowing in paramagnetic resonance", *Rev. Mod. Phys.* **25**, pp. 269 (1953).

[142] P. W. Anderson, "A mathematical model for narrowing of spectral lines by exchange or motion", *J. Phys. Soc. Japan* **9**(3), pp. 316 (1954).

[143] R. Kubo, "Note on the stochastic theory of resonance absorption", *J. Phys. Soc. Japan* **9**(6), pp. 935 (1954).

[144] R. Kubo, "A stochastic theory of line shape", *Adv. Chem. Phys.* **15**, pp. 101 (1969).

[145] R. Kubo, *Fluctuation, Relaxation and Resonance in Magnetic Systems*, Oliver and Boyd Ltd. Edinburgh (1962).

[146] W. B. Mims, "Phase memory in electron spin echoes, lattice relaxation effects in $CaWO_4 : Er, Ce, Mn$ ", *Phys. Rev.* **168**, pp. 370 (1968).

[147] W. B. Mims, *Electron Paramagnetic Resonance* , p. 263, Plenum Press New York (1972).

[148] D. R. Taylor and J. P. Hessler, "Photon echo decay in Ruby: Electric dipole interactions and instantaneous diffusion", *Phys. Lett.* **50A**, pp. 205 (1974).

[149] P. Hu and S. R. Hartmann, "Theory of spectral diffusion decay using an uncorrelated-sudden-jump model", *Phys. Rev. B* **9**, pp. 1 (1974).

[150] P. Hu and L. R. Walker, "Spectral-diffusion decay in echo experiments", *Phys. Rev. B* **18**, pp. 1300 (1978).

[151] J. Ganem, Y. P. Wang, R. S. Meltzer, W. M. Yen, and R. M. Macfarlane, "Non-exponential photon-echo decays of paramagentic ions in the superhyperfine limit", *Phys. Rev. Lett.* **66**(6), pp. 695 (1991).

[152] R. M. Macfarlane, R. Wannemacher, D. Boye, Y. P. Wang, and R. S. Meltzer, "Nonexponential photon echo decay of $Er^{3+}$ in fluorides", *J. Lumin.* **48**, pp. 313 (1991).

[153] A. Szabo, T. Muaramoto, and R. Kaarli, "$^{27}$Al nuclear-spin dephasing in the Ruby frozen core and $Cr^{3+}$ spin-flip-measurements", *Phys. Rev. B* **42**, pp. 7769 (1990).

[154] P. F. Liao and S. R. Hartmann, "Magnetic field- and concentration-dependent photon echo relaxation in Ruby with simple exponential decay", *Opt. Comm.* **8**, pp. 310 (1973).

[155] J. Huang, J.M. Zhang, and T.W. Mossberg, "Excitation-induced frequency shifts and frequency dependent dephasing in $Eu^{3+} : Y_2O_3$", *Opt. Comm.* **75**(1), pp. 29 (1990).

[156] J. Zhang and T. W. Mossberg, "Optically induced shifts in the frequency of the $^3H_4 - {}^1D_2$ transition of $Pr^{3+}$ in $LaF_3$", *Phys. Rev. B* **48**, pp. 7668 (1993).

[157] L. Root and J. L. Skinner, "Optical dephasing and photon echoes from energetically and substitutionally disordered crystals", *J. Phys. Chem.* **81**, pp. 5310 (1984).

[158] L. Root and J. L. Skinner, "Frequency-dependent optical dephasing and the nature of inhomogeneous broadening in crystals", *Phys. Rev. B.* **32**, pp. 4111 (1985).

[159] W. S. Warren and A. H. Zewail, "Optical dephasing in multilevel systems. Bath-independent dephasing and breakdown of the two-level approximation", *J. Phys. Chem.* **85**, pp. 2309 (1981).

[160] W. S. Warren and A. H. Zewail, "Multiple phase-coherent laser pulses in optical spectroscopy ii. Applications to mulilevel systems", *J. Chem. Phys.* **78**, pp. 2298 (1983).

[161] W. Bron, editor, *Non-equilibrium Phonon Dynamics*, NATO ASI Series. Plenum Press N.Y. (1984).

[162] S. Kröll, E. Y. Xu, M. K. Kim, R. Kachru, and M. Mitsunaga, "Intensity-dependent photon-echo relaxation in rare-earth-doped crystals", *Phys. Rev. B* **41**(16), pp. 11568 (1990).

[163] S. Kröll, E. Y. Xu, and R. Kachru, "Influence of excited-state $Pr^{3+}$ on the relaxation of the $Pr^{3+} : YAlO_3$ $^1D_2 - {}^3H_4$ transition", *Phys. Rev. B* **44**, pp. 30 (1991).

[164] Luo-Baozhu and S. Kröll, "Observation of magnetic-field-induced resonance in the homogeneous dephasing time for the $^1D_2 - {}^3H_4$ transition in $Pr^{3+} : YAlO_3$", *Phys. Rev. B* **54**(14), pp. 9834 (1996).

[165] A. P. Kulesski, A. M. Korovkin, A. V. Kruzkalov, L. V. Viktorov, and B. V. Shugin, "Radioluminescence and scintillation properties of monocrystals of sillicates of yttrium and rare earth elements", *J. Appl. Spect.* **48**, pp. 446 (1988).

[166] G. D. Mahan, "Local-field corrrections to Coulomb interactions", *Phys. Rev.* **153**(3), pp. 983 (1967).

[167] S. R. Polo and M. K. Wilson, "Infrared intensities in liquid and gas phase", *J. Chem. Phys.* **23**(12), pp. 2376 (1955).

[168] C. F. Boettcher, *Theory of electric polarization* volume 1, Elsevier Amsterdam 2nd edition (1973).

[169] G. K. Liu, R. L. Cone, M. F. Joubert, B. Jacquier, and J. L. Skinner, "Energy transfer and instantaneous spectral diffusion processes in $Tb^{3+}$ compounds as probed in photon echo experiments", *J. Lumin.* **45**, pp. 387 (1990).

[170] K. F. Renk, *Detection of High-Frequency Phonons by Phonon-induced Fluorescence* volume 16 chapter 6, , p. 277, Elsevier Amsterdam (1986).

[171] W. Demtröder, *Laser Spectroscopy, Basic Concepts and Instrumentation*, Springer Berlin (1996).

[172] I. S. Gradshteyn and I. M. Ryzhik, *Tables of Integrals, Series, and Products*, Academic Press N.Y. (1980).

[173] M. Abramowitz and A. Stegun, *Handbook of Mathematical Functions*, Dover Press N.Y. (1972).

# Curriculum Vitae

| | |
|---|---|
| Name: | Felix R. Graf |
| Date of birth: | June 5, 1967 |
| Place of birth: | Midland (Mi), U.S.A |
| Nationality: | Swiss, American. |
| Citizenship: | Winterthur (ZH). |
| Parents: | Walter and Margrit Graf-Schüepp. |
| Marital status: | married to Fatma Hayatally. |

## Education

| | |
|---|---|
| April '74 - April '80 | Primary school in Oberrieden and Thalwil (ZH). |
| April '80 - Sept. '83 | "Gymnasium Bühl", Zürich. |
| Sept. '80 - April '83 | "Liceo della scuola svizzera di Milano" (Italy). |
| April '83 - Sept. '87 | "Mathematisches Naturwissenschaftliches Gymnasium Rämibühl", Zürich. Matura Typus C. |
| July '91 - Nov. '91 | Trainee with Dow Chemical, Michigan (USA). Analytical chemistry department. |

## Studies

| | |
|---|---|
| 1988 - 1993 | Studies at the ETH Zürich in interdisciplinary science. Emphasis: Physics. Degree in natural science. Diploma thesis in optical data storage in the group of Prof. Urs P. Wild. Silver medal award of the ETH for the diploma thesis. |
| 1994 - 1998 | Postgraduate studies in the group of Prof. Urs P. Wild at the physical chemistry departement ETH. |

## Teaching experience

| | |
|---|---|
| Nov '93 - July '98 | Teaching assistant in the departement of physical chemistry for various lectures and practical courses. |